STUDY OF SODIUM ALUMINOBOROSILICATE GLASSES FOR PHOTOMULTIPLIER TUBE GLASS APPLICATION IN NEUTRINO DETECTION USING EXPERIMENTAL AND MOLECULAR DYNAMICS TECHNIQUES

BY

RUHIL MAN SINGH DONGOL

A THESIS

SUBMITTED TO THE FACULTY OF

ALFRED UNIVERSITY

IN PARTIAL FULFILLMENT OF THE REQUIREMENTS
FOR THE DEGREE OF

DOCTOR OF PHILOSOPHY

IN

MATERIALS SCIENCE AND ENGINEERING

ALFRED, NEW YORK

FEBRUARY, 2018

STUDY OF SODIUM ALUMINOBOROSILICATE GLASSES FOR PHOTOMULTIPLIER TUBE GLASS APPLICATION IN NEUTRINO DETECTION USING EXPERIMENTAL AND MOLECULAR DYNAMICS TECHNIQUES

BY

RUHIL MAN SINGH DONGOL

B.A. COE COLLEGE (2010)

SIGNATURE OF AUTHOR_____

APPROVED BY _____
DR. S. K. SUNDARAM, ADVISOR

_____
DR. A. N. CORMACK, ADVISORY COMMITTEE

_____
DR. A. G. CLARE, ADVISORY COMMITTEE

_____
DR. W. C. LACOURSE, ADVISORY COMMITTEE

_____
DR. W. CARLSON, CHAIR, ORAL THESIS DEFENSE

ACCEPTED BY _____
ALASTAIR N. CORMACK, INTERIM DEAN
KAZUO INAMORI SCHOOL OF ENGINEERING

ACCEPTED BY _____
JAY CERIO, INTERIM ASSOCIATE PROVOST
FOR GRADUATE AND PROFESSIONAL PROGRAMS
ALFRED UNIVERSITY

ACKNOWLEDGMENTS

I am truly indebted and grateful to my advisor, Dr. S. K. Sundaram, for his unwavering support, guidance, and most definitely patience, throughout my graduate years at Alfred University, and without whom this work would not have been possible. I would like to extend my sincere thanks to Dr. Alastair. N. Cormack, for his guidance as I embarked on the computational work. I would also like to thank my committee members, Dr. William C. LaCourse, and Dr. Alexis G. Clare, for their assistance, availability and support.

I must thank Dr. Adama Tandia, for his guidance and support in a significant part of my work and Dr. Liaoyuan Wang for working tireless with me. I thank my lab mates and friends, Priyatham Tumurugoti, Braeden Clark, Dimple Pradhan and Yuxuan Gong for their friendship, support, encouragement and wonderful working experience. I also would like to thank A. J. Lanphere, Tyler Gubb and Bu Wang for their advice and support during the start of my computational work.

I also extend my thanks to my friends for their kind support and encouragement throughout the process. I thank Alfred University and the community for the amazing experience over the past six years.

I thank my significant other, Shringkhala Bajimaya, for her love and support, and who has been an absolute rock to me. Her confidence, belief and persistence is inspiring and has kept me going through challenging and difficult times.

Finally, I would like to dedicate this work to my family for whom I endeavor. Their support for me throughout my life, while going through hardship themselves, has kept me persevering. I am grateful for my father, Bikash Dongol, for forever keeping me in track, my mother, Reeta Dongol, for her unconditional love and always worrying if I ate or slept right, my brother, Anish Dongol, whom I love so dearly.

TABLE OF CONTENTS

LIST OF TABLES

LIST OF FIGURES

ABSTRACT

In this thesis, we present a comprehensive study of structural, mechanical properties, and chemical durability of commercial and experimental aluminoborosilicate glasses with potential for photomultiplier tube application using both experimental and molecular dynamics (MD) techniques.

The mechanical properties, measured using Vickers indentation and ring-on-ring (R-O-R) biaxial flexural strength test, showed similar performance for two commercial PMT glasses. The chemical durability test under simulated neutrino detector conditions revealed dealkalized and deboronated layer at the glass surface. In addition, the normalized mass loss indicated pH and temperature dependent ion-release behavior. The effect of high-purity water on the R-O-R flexural strength of the glass was minor as the test measures the bulk strength of the glass. Furthermore, we verified the release of gadolinium (Gd) ions in high-purity water from a Gd-doped aluminoborosilicate glass, which could be used as a controlled Gd-source in future WCDs to enhance neutrino detection.

Two MD projects were completed. In the first project, the composition-structure-property relationship of sixty-nine different multicomvponent aluminoborosilicate glasses within the compositional space of commercial PMT glasses were studied. The glasses were simulated using classical MD. The structural and mechanical properties such as bond distance, coordination number (CN), Q_n speciation, bridging oxygen (BO) and non-bridging oxygen (NBO) concentration, and Young's Modulus (E) were calculated. The glasses were further differentiated in terms of low-E and high-E glasses and subjected to temperature and pressure simulations. The densities and E values calculated showed no statistical variations for the glasses simulated at different temperature and pressure conditions. In the simulated glasses, silicon was almost entirely 4-coordinated, boron was observed in 3- and 4-coordination and aluminum was found in 4- and 5-coordination. The BO concentration of 93.4±0.84% suggests highly polymerized simulated glasses. The high-E glasses contained higher BO and lower NBO concentrations as compared to low-E glasses. Furthermore, low-E glasses consisted of higher amount of depolymerized glass former structural units. The polymerization of the simulated glasses was affected by the presence of sodium, which takes on multiple roles of charge compensating ion for tetra-coordinated Al and B, and modifies the glass network by creating NBO sites at Si and B structural units.

In the second MD project, the bulk and surface structures, and the glass surface-water reactions of sodium aluminosilicate glass were simulated using a combination of classical Buckingham and reactive force field (ReaxFF) potentials. On comparison of the simulated glass structures generated using ReaxFF and Buckingham potentials, our results showed that the atomic density profiles calculated for the surface glass structures indicate a bond-angle distribution dependency, and higher concentrations of NBOs and sodium ions at the glass surface. Additionally, our results showed the formation of silanol species and diffusion of water molecules at the glass surface using ReaxFF.

CHAPTER 1. INTRODUCTION

Aluminoborosilicate glasses have a wide range of applications ranging from fiberglass reinforcement, optical components, sealing materials, and as a host matrix for immobilization of nuclear waste to photomultiplier tube (PMT) application in water Cherenkov detectors (WCDs) for neutrino detection. The PMTs are light sensitive glass-enclosed vacuum tubes that convert extremely weak optical signals, which could be down to a single-photon level, to detectable electrical signal. In a WCD, the PMTs detect Cherenkov radiation generated from interaction of neutrinos and water molecules. The WCD is a massive underground water tank with capacity to hold thousands of tons of high-purity water with resistivity from 11 to 18.24 MΩ-cm, nearing the theoretical limit. A single WCD employs a large number of PMTs. Due to their size, the PMTs can experience a maximum hydrostatic pressure of ~1 MPa. In addition, a typical lifetime of a WCD is ~10-20 years. A combination of aqueous and pressurized environment creates a detrimental operation condition for the PMT glasses, which could significantly compromise the long-term reliability of PMT glasses. PMT failures can result from a variety of different factors, including bulb shape, glass thickness, surface or bulk flaws, stress corrosion, residual stresses from processing, and extended exposure to the environmental conditions of neutrino detection. Any failure of PMTs can disrupt the long-term experiments before their designed conclusions.

1. Thesis Objectives and Contents

This thesis emphasizes the fundamental understanding of structural and mechanical properties and chemical durability of the sodium aluminosilicate glasses to better understand the PMT glasses for WCD application. To achieve this, we have combined experimental and computational research approaches to investigate the structure and properties of aluminoborosilicate glasses. The objectives of the thesis are:

- Characterize the mechanical properties and chemical durability of the commercial PMT and simplified Alfred glasses to provide groundwork for further studies and industrial usage

- Design a gadolinium (Gd)-doped glass composition and study the Gd ion release behavior in high-purity water as a novel approach to deliver Gd ions into the WCD for enhanced detection
- Perform composition-structure-property relationship study of statistically designed multicomponent aluminoborosilicate glass composition using molecular dynamics (MD) simulations
- Implement reactive force field (ReaxFF) potential to study the glass structures and the glass surface-water reactions of sodium aluminosilicate glass in a reactive MD framework

The remainder of this thesis is structured as follows: Chapter 2 presents a brief literature survey. In Chapter 3, the materials and methods used to study the aluminoborosilicate glasses are described. In the experimental procedure section, the glass compositions and sample preparation methods used for experimental studies are presented. In molecular dynamics section, the potential models used for classical and reactive MD simulations are presented. The next four chapters (Chapters 4-7) presents 4 distinct topics matching with the objectives.

Chapters 4 and 5 summarize the experimental studies. In Chapter 4, the experimental works on mechanical property and chemical durability of commercial PMT and Alfred glasses are presented. In Chapter 5, the results and discussions of the Gd-doped glass and its ion release behavior are discussed. This work is performed to search for alternative methods to include Gd ions in the water systems of the WCD, which can increase the sensitivity of the WCD.

Chapters 6 and 7 describe the MD simulation studies. The research work on the application of a reactive force field (ReaxFF) potential on a ternary sodium aluminosilicate glass is presented in Chapter 6. This work extends the application of ReaxFF to a ternary glass system by investigating the glass structures and the glass surface-water reactions. In Chapter 7, the study of the composition-structure-property relationship of multicomponent aluminoborosilicate glasses using classical MD technique is detailed. The work focuses on the detail study of the composition and structure of the simulated glasses and their effect on the mechanical property, Young's modulus. All our findings are summarized along

with some thoughts on the future studies of aluminoborosilicate glasses are presented in Chapter 8. Chapter 9 lists the cited reference, and is followed by an appendix.

CHAPTER 2. LITERATURE REVIEW

1. Photomultiplier Tube in Water Cherenkov Detector for Neutrino Detection

1.1 What are Neutrinos?

The Neutrinos are fundamental particles that have a quantum spin number ½ and a negligible mass compared to other elementary particles (negligible gravitational interactions) with no electromagnetic charge (no Coulomb interactions) and baryonic charge (no strong interactions). It interacts with particles via the weak interaction. There are three types of neutrinos: an electron neutrino (ν_e), a muon neutrino (ν_μ), and a tau neutrino (ν_τ), each with its own antiparticle. Although, W. Pauli first postulated the neutrino particle in 1930 and was termed 'little neutral one' by Fermi in 1933,[1] it was not until 1956, the first neutrino was detected by C. Cowan and F. Reines.[2] The existence of cosmic neutrinos was experimentally proven by Masatoshi Koshiba and Raymond Davis Jr., who were awarded with Nobel prize in physics 2002.[3] Subsequent improvement in the detection technology led to discovery of the neutrino oscillation, which proved the neutrinos carry miniscule mass and the Nobel prize in physics was awarded to Takaaki Kajita and Arthur B. McDonald in 2015.[4]

Neutrinos are abundant in nature, but difficult to detect. On average, about ten trillion neutrinos per second pass through a cubic centimeter on the Earth.[5] The sources of neutrinos are numerous. Stars, like the sun, produces a large number ($\sim 5 \times 10^6$ $cm^{-1}s^{-1}$) of neutrinos in the fusion processes, and geological neutrinos from natural radiation have a flux of 6×10^6 $cm^{-1}s^{-1}$. The relic neutrinos left over from supernova bursts is $\sim 6 \times 10^{58}$ over ten seconds. Other sources include nuclear accelerators that produce neutrinos for physics experiments and nuclear reactors that produce over 10^{20} neutrinos per second as a byproduct of the fission process. The abundance of neutrinos makes the study of neutrinos possible.

1.2 Significance of Discovery of Neutrino Oscillation

Originally, atmospheric neutrinos were of interest to the high-energy physics community as they are the most significant background to proton decay experiments. In

1980's, several large underground detectors experiments were constructed to study the proton decay; however, instead of proton decay, these experiments observed many atmospheric neutrino events. These detectors were then used to study the number of ν_e and ν_μ interactions. It was found that the ν_μ interactions had a significant deficit compared with the Monte Carlo prediction, while the numbers of ν_e detected were in good agreement with the prediction.[6] This discrepancy between the predicted atmospheric neutrino fluxes and that observed in detectors initiated a serious interest in atmospheric neutrinos. Subsequent studies confirmed the deficit of ν_μ interactions were explained by either $\nu_\mu \rightarrow \nu_\tau$ or $\nu_\mu \rightarrow \nu_e$ oscillations.[7,8] Even though the neutrino oscillations were conceived, the data were inconclusive due to relatively poor interaction statistics. To observe statistically conclusive evidence of neutrino oscillations, Super-Kamiokande[9] (Super-K) experiment was started in 1996. In 1998, the Super-K experiment findings showed that the atmospheric neutrinos data gave evidence for neutrino oscillation[10,11] and determined that the oscillation was mostly between ν_μ and ν_τ.[12] The evidence of neutrino oscillation proved the existence of neutrino mass, which was previously assumed to be massless under the Standard Model[13] of elementary particles. Thus, it provided the first unambiguous evidence of the physics beyond the Standard Model.

In neutrino physics community, the Super-K experiment has been a landmark achievement that has produced groundbreaking results summarized in these articles.[14–16] In addition to providing direct evidence of atmospheric neutrino oscillations, the detector was instrumental in confirming neutrino oscillations using a man-made neutrino source in the first long-baseline experiment, the high energy accelerator research organization (KEK) to Kamioka (K2K) experiment,[17] which were consistent with results from main injector neutrino oscillation search[18] (MINOS) and Tokai to Kamioka[19,20] (T2K) experiments. In addition, the Super-K experiment has searched for deviations and subleading effects from sterile neutrinos,[12] mass-varying neutrinos,[21,22] non-standard interactions,[23] and Lorentz violation.[24] The profound success of Super-K is based on the scalability of the WCD. In addition to WCD, other notable neutrino detection techniques include liquid scintillator,[25] radiochemical method,[26] radio detector,[27] tracking calorimeter,[28] and coherent recoil detector.[29] In comparison, the WCD is a relatively inexpensive detector but in general, neutrino detection experiments have long-term scientific and financial implications.

1.3 Neutrino Detection using Water Cherenkov Detector

In a WCD, a particle is detected by the Cherenkov light it emits in the water. The emission of Cherenkov radiation was discovered by Pavel Alekseyevich Cherenkov in 1934. A charged particle, such as muon or electron, moving at greater than the speed of light in the medium ($v = c/n_{water} = \frac{3\times10^8}{1.33} \approx 2.26 \times 10^8$ m/s in water and c is the speed of light in a vacuum and n_{water} is the refractive index of water), builds up radiation at an angle $cos\theta = \frac{c/n_{water}}{\beta c}, (\beta = v_{particle}/c)$. This radiation eventually becomes a radiation shockwave or an optical boom, analogous to a sonic boom but in the form of a light cone. Figure 2-1 shows a two-dimensional representation of geometry of Cherenkov radiation. The radiation is emitted at an angle (θ) = arccos(1/n) to the direction of travel and the blue arrow are photon direction, which are detected by PMTs lined in the inner walls of the detector. WCD uses purified water as its refractive index (n) is ~1.33 and a 'transparency window' with attenuation lengths > 50 m in the spectral region of 320-480 nm, which matches with Cherenkov radiation.

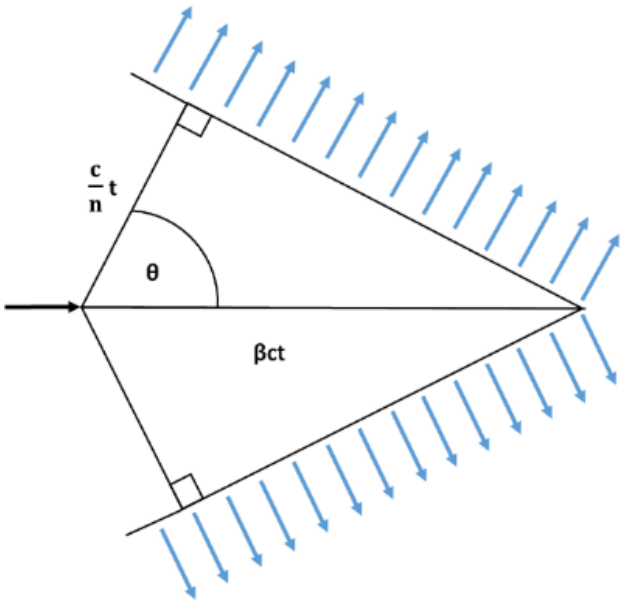

Figure 2-1. Schematic of geometry of Cherenkov radiation propagation

In WCDs, a neutrino can interact with nuclei in the water and generate a charge lepton with enough energy to emit Cherenkov radiation. A lepton is an elementary, half-integer spin particle that consists of two main classes: charged leptons (also known as electron-like leptons), and neutral leptons (better known as neutrinos). The emitted radiation travels through the detector media and is detected by the PMTs lined in the inner walls of the WCD. In a neutrino-event (instance where a neutrino generates Cherenkov radiation), a PMT light map can be built from the fixed angle of the cone of light in the direction of travel, the timing and charge distribution. The energy and direction of travel of the charged particle can be determined via the light map which are compared with various 3-dimensional neutrino flux models[30–34] to determine the nature of the interacting neutrinos.

1.4 The Water Cherenkov Detector

The WCD has been successfully implemented in neutrino detection programs such as Irvine-Michigan-Brookhaven[35] (IMB), Kamiokande,[36] Super-Kamiokande,[9] and Sudbury Neutrino Observatory[37] (SNO) among others. These detectors have gathered vast amount of data to excel the field of neutrino physics. In general, WCDs are massive water tanks constructed deep underground to shield it from background cosmic rays and have an operational lifetime of ~10-20 years. The largest one built to date is the Super-K detector. The detector itself is a cylindrical tank of 41.4 m high and 39.3 m in diameter. The Super-K detector can hold 50 kilotons of water with a 22.5 kiloton fiducial volume. It is built ~1000 m below ground level and has 13,000 PMTs in the inner and outer walls. Figure 2-2 shows the pre-operational image of the interior of WCD for the Super-Kamiokande Observatory. In the image, each bright spot represents a 50-cm diameter single semi-hemispherical PMTs.

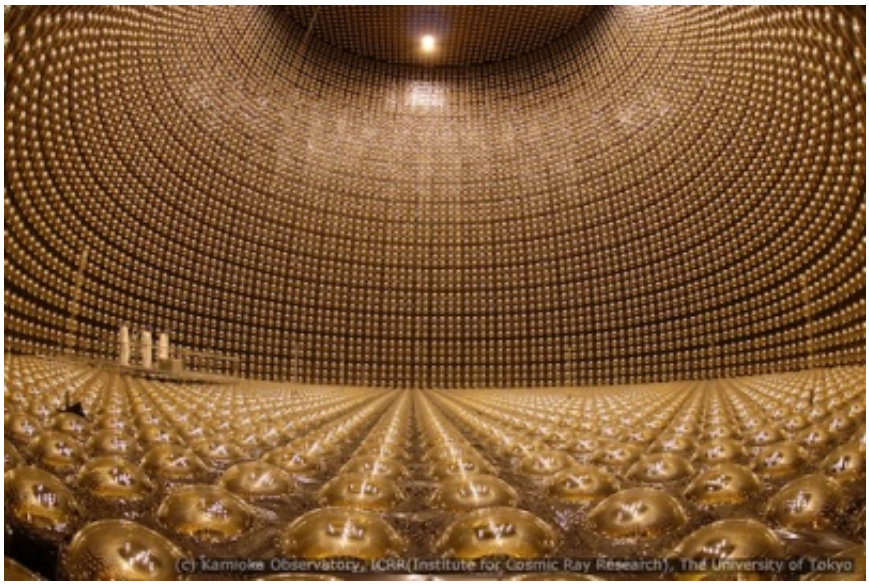

Figure 2-2. Interior of WCD in Super-Kamiokande Observatory, ICRR (Institute of Cosmic Ray Research), The University of Tokyo

Table 2-I lists the detector size and the number of PMTs used in various detector programs. As discussed in Section 2.2, bigger detector leads to better interaction statistics. Additionally, there are proposals for an even bigger, next generation detector called the Hyper-Kamiokande[38] (Hyper-K). The Hyper-K consists of two cylindrical tanks lying side-by-side with outer dimension of each tank being 48 (W) × 54 (H) × 250 (L) m^3. The proposed detector has a total (fiducial) mass is 0.99 (0.56) million metric tons, which is about 20 (25) times larger than the Super-K. The Hyper-K employs 99,000 50-cm diameter PMTs corresponding to the PMT density of 20% light coverage. In addition to Hyper-K, the future neutrino detection programs include India-based Neutrino Observatory[39] (INO), Precision IceCube Next Generation Underground (PINGU) detector,[40] and Oscillation Research of Cosmics in the Abyss (ORCA), which is a low energy extension of the Cubic Kilometer Neutrino Telescope (KM3NeT) detector in the Mediterranean.[41] Furthermore, the WCDs are also used as veto detector system in Jiangmen Underground Neutrino Experiment[42] (JUNO) in China.

Table 2-I. List of Water Cherenkov Detectors

Neutrino Detector	Location (timeline)	Fudicial mass	No. of PMT (bulb diameter in cm)
Irvine-Michigan-Brookhaven detector (IMB)	Lake Erie, USA (1979-1989)	5000 ton of ultra-pure water	2048 (20)
Sudbury Neutrino Observatory (SNO)	Sudbury, Canada (1999-2006)	1000 ton of heavy water	9600
Kamioka Nucleon Decay Experiment (Kamiokande)	Kamioka, Japan (1983-1996)	3000 tons of pure water	1000 (50)
Super-Kamiokande (Super-K)	Kamioka, Japan (1996-present)	22.5 ktons of pure water	13,000 (50)
Underground Nucleon decay and neutrino Observatory (UNO)	Colorado, USA (planned)	440,000 tons	60,000
Hyper-Kamiokande Detector (Hyper-K)	Kamioka, Japan (planned)	1,250,000 tons of pure water	99,000 (50)

1.5 Photomultiplier Tube (PMT)

PMTs are sophisticated light sensitive glass-enclosed vacuum tubes that convert extremely weak optical signal, down to single-photon level, to a detectable electrical signal. The underlining physical phenomenon is the photoelectric effect. An incoming single photon strikes the photocathode to generate a photoelectron. This electron is accelerated to a charged dynode within the tube and upon striking the dynode it creates more electrons. There are several dynodes within a PMT. This process occurs several times resulting in a cascade of electrons, thus amplifying the original photon to a detectable electrical signal which is recorded for analysis. Figure 2-3 shows a schematic of PMT used in the Super-K experiment, a detailed description can be found in Suzuki et al.[43]

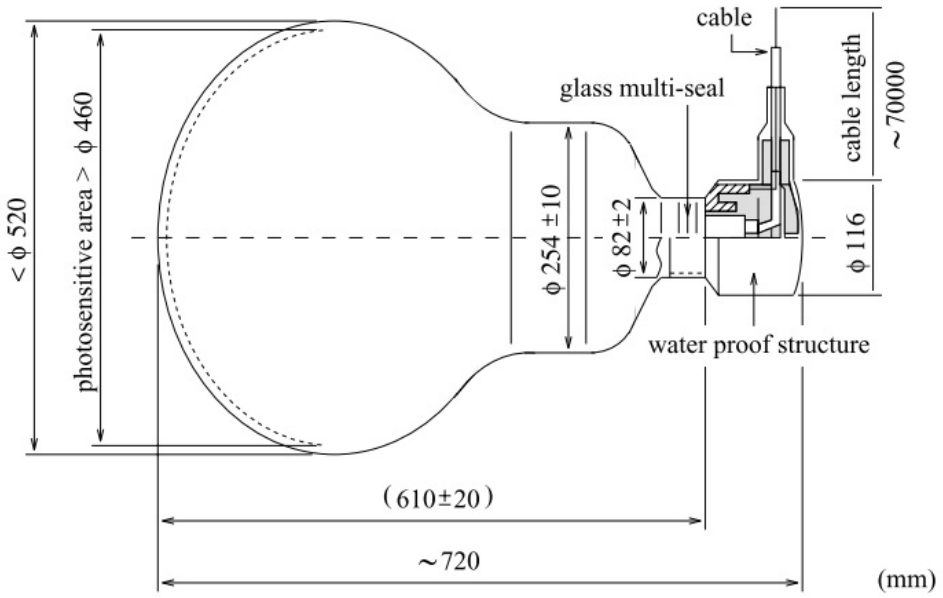

Figure 2-3. Schematic of a 50 cm PMT as illustrated in Fukuda et al.[9]

The PMT employed in a WCD is a large format custom built PMT. In Super-K detector, 7650 PMTs are distributed on the side wall and 1784 each on the top and bottom areas, amounting to a 40.41% coverage of the inner surface area. The photon collection coverage was increased from 20% to 40 % with 50 cm PMTs[43] with improved time resolution of 2.2 ns and improved single photoelectron response. The adjacent PMTs are spaced at 70 cm with a layer of black polyethylene terephthalate. Details of data acquisition setup, electronic huts and Analog Timing Modules (ATMs) among others, can be found in Koshio's work.[44]

PMTs play a vital role in the success of WCDs. As discussed in Section 1.2, a large number of PMTs increases the detector sensitivity. However, with the use of larger numbers the risk of glass failure increases, especially inside the detectors as the PMTs can experience a maximum hydrostatic pressure of ~1 MPa at the bottom of the detectors due to the height of the detectors. In addition, the PMTs are exposed to high-purity water for the entire detector lifetime of ~10-20 years. The corrosive nature of the high-purity water coupled with hydrostatic pressure in the detector, creates a unique and detrimental operational condition for the long-term application of PMT glasses that can lead to a premature failure of the PMTs. As a case in point, in 2001, an implosion of a single PMT

in the Super-K detector created a catastrophic 'shock-wave' that destroyed 60% of the PMTs in a few seconds.[45] The total rebuilding cost to make the WCD operational was approximately $20 million. This incident shows that the long-term reliability of the PMT glasses are essential for the success of the detection program and carries financial and scientific implications. Despite that necessity to understand the properties of these glasses under detector conditions, there is a lack of scientific effort in this area. In the following section, a brief background on the aluminoborosilicate glass properties for PMT application is presented.

2. Aluminoborosilicate Glasses

The PMT glasses are primarily multicomponent aluminoborosilicate glasses. These glasses selected based on their low thermal expansion coefficient, good mechanical properties, high water-resistance characteristics, and allows transmission of electromagnetic radiation from 300-700 nm. The properties of glasses are dependent on glass composition and structures. In this thesis, we will only be focused on the aluminoborosilicate glass compositions that are close to the commercially available PMT glass compositions. In the following section, structures of aluminoborosilicate glasses are discussed.

2.1 Glass Structure

The amorphous nature of oxide glasses is characterized by the lack of long-range atomic ordering; however, they do exhibit some degree of short-range ordering. The structure of an archetypical silica glass consists of 4-coordinated corner sharing Si-tetrahedra that share oxygen atoms called "bridging oxygen" (BO)[46] and forms a silicate framework. The BO links together two network-formers (e.g. Si-O-Si). The addition of ions such as (Na^+, K^+, Ca^{2+}, Ba^{2+}, etc.) form comparatively weaker bonds with oxygen than Si^{4+}. These alkali metals and alkaline earths are linked to terminal oxygens on tetrahedra, thus acts as a network-modifier and creates non-bridging oxygens (NBOs). The relative abundance of NBOs in glasses is critical in determining the thermodynamic and other dynamic properties of silicate glasses and melts.

Aluminum (Al) and boron (B) act as network formers in silicate glass network. The Al and B atoms replace the Si to form 4-coordinate Al (AlO_4 tetrahedra) and 3-coordinated B (trigonal BO_3) and 4-coordinated B (BO_4 tetrahedra). The 4-coordinated structures of Al and B structures require a charge compensating alkali and alkaline-earth modifier cations. The reaction can be represented as $R_2O_3 + Na_2O = 2Na^+[RO_4]^-$, where R = Al or B.

In borosilicate glasses, the 3-cooridnated B ($^{[3]}B$) converts to 4-coordination ($^{[4]}B$) with the addition of alkali up to about 40%, depending upon modifier and silica content. The fraction of 4-coordinated B among total B is defined as N_4. The formation of $^{[4]}B$ is accompanied by a charge compensating modifier atoms. If enough modifiers are added, the 4-coordinated B begin to convert to asymmetric BO_3 groups and a NBO at BO_3. However, the starting point and the rate of this process depend strongly on the composition.[47] The structural reaction between the formation of $^{[3]}B$, $^{[4]}B$, and NBO in a system is hypothesized by:

$$^{[3]}B + NBO \Leftrightarrow {}^{[4]}B \tag{2.1}$$

A low modifier oxides content in B-rich glasses would result formation of 4-coordinated B and push the reaction to the right-hand side.[47–49] At high modifier contents, the reaction shifts to the left, primarily to avoid formation of $^{[4]}B$-O-$^{[4]}B$ species.[50] These are relatively energetically unfavorable due to higher net negative charge at the bridging oxygen atoms.[50,51] The presence of higher modifier cation field strength ions favor the formation of NBO and hence results in conversion of $^{[4]}B$ to $^{[3]}B$ and NBO.[52–54]

The addition of Al adds more complexity into the glass structure. In general, the structure of an aluminoborosilicate glass is an interconnected network of Si, Al and B glass former units with modifier ions taking various roles within the glass structure. Al is predominantly 4-coordinated ($^{[4]}Al$) accompanied by a charge compensating modifier ions. Additionally, significant amount of $^{[5]}Al$ have been revealed in glasses with divalent modifier cations.[54] Furthermore, B_2O_3 and Al_2O_3 compete with each other to combine with alkali or alkaline-earth oxides to transform $^{[3]}Al$ to $^{[4]}Al$ or $^{[3]}B$ to $^{[4]}B$.[55] It has been shown that, alkali oxides prefer to react with Al_2O_3, because of the energetics of the charge-

balance mechanism is more favorable for the Na-Al^{3+} species than for Na-B^{3+} species.[56] The structure and properties of aluminoborosilicate glasses have been studied using experimental[57] and MD[58,59] techniques.

Additional relevant literature is cited in appropriate chapters throughout this thesis to make the chapters complete and enhance the readability.

CHAPTER 3. MATERIALS AND METHODS

In this chapter, the glass compositions and sample preparation methods for experimental studies and potential models used in computational studies are presented.

1. Experimental Methods - Sample Preparation

1.1 Aluminoborosilicate Glass Composition

The glasses studied in this work are of aluminoborosilicate glass composition. Table 3-I shows the compositional range of two commercial PMT glasses (from here onwards the two glasses will be referred to as Vendor1 and Vendor2) and the composition of simplified Alfred glass. The composition of Alfred glass was selected to closely represent the vendor glass compositional range, but with higher Na content to facilitate easy melting and processing.

Table 3-I. Composition (wt%) of Vendor and Alfred Glasses

Oxide	Commercial PMT	Simplified Alfred
SiO_2	65-70	64
Al_2O_3	4-7	9
B_2O_3	15-18	14
Na_2O	6-9	13
CaO	0-1	-
BaO	0-3	-
ZnO	0-3	-

1.2 Glass Synthesis

The commercial glasses were received in cullet forms and melted in a platinum crucible in an electrically-heated high-temperature furnace at 1450 °C for 4-6 h and 1550 °C for 0.5 h to facilitate pouring. The Alfred glass was synthesized using reagent-grade SiO_2, Al_2O_3, H_3BO_3, and Na_2CO_3. The chemicals were weighted and mixed thoroughly. For small batch size (<20 g), the chemicals were manually mixed in the platinum crucible using spatula, while for larger batch size (>50g), the chemicals were mixed using ball milling in a solution of ethanol and water. The mixture was milled overnight and dried at

110-120 ℃. The resulting powders were placed in a platinum crucible and melted in a high temperature furnace at 1450 ℃ for 1 h and 1550 ℃ for 0.5 h to facilitate pouring. The melt was poured in a cylindrical stainless-steel mold of ~30 mm inner diameter to produce bulk cylindrical glass samples.

The annealing temperature for the glasses were determined by measuring the glass transition temperature (T_g) using a differential scanning calorimeter (DSC – TA Instruments model 2910). Pieces of glass samples, held in platinum pans alongside an empty pan, used for reference, were heated at a rate of 10 °C/min from room temperature to 610 °C under a nitrogen atmosphere. Glass transition temperatures estimated using the tangent intercept method on the temperature versus heat flow graph were 554.4 °C, 510.5 °C, and 540.2 °C for Vendor1, Vendor2 and Alfred glasses, respectively. A temperature of 600 °C was deemed suitable to anneal the glass samples for an hour and cooled at 5 °C per minute to room temperature.

1.3 Disk Glass Samples for Mechanical Testing

The disk samples were prepared by cutting the glass cylinders using a high-speed saw (Struers Discotom-5, Copenhagen, Denmark) at spindle speed of 2850 rpm 50 Hz. The use of high-speed saw reduced the sample preparation time. The planarization of disk samples was performed using 8" wet/dry silicon carbide (SiC) abrasive grinding pressure sensitive adhesive (P.S.A) premium discs (MetLab Corp., Niagara Falls, USA) with kerosene or mineral oil as a lubrication media. The average grinding grain size (in μm) used was 30.4, 20.9, 14.0, 9.2 to 6.2 on both sides of the disk samples. The samples were thoroughly washed with ethanol between switching sides and changing grinding discs. The samples were polished with 3 μm, 1 μm and 0.25 μm polycrystalline (black) diamond particles suspension (MetLab Corp., Niagara Falls, USA) solutions. The disk glass sample preparation steps are shown in Figure 3-1. The samples were ultrasonically cleaned in ethanol, and stored in desiccant chamber for usage.

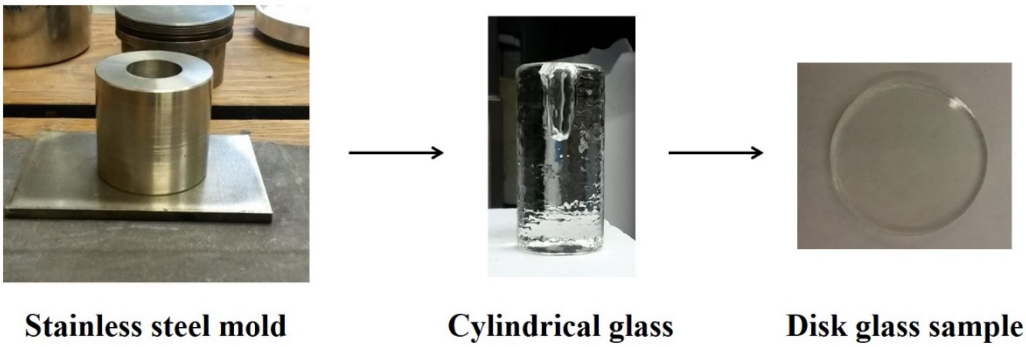

Figure 3-1. Disk glass sample preparation

1.4 Powdered Glass Samples for Leaching Experiments

Powdered glass samples were prepared by crushing larger glass pieces using mortar and pestle. The powdered glass samples of 63-75 μm size fractions were sieved and collected. The powdered glass was ultrasonically cleaned in acetone and then in ethanol for 10 min each, dried overnight at 90±1 °C and stored in a desiccator before use.

2. MD Simulations

MD simulation technique is a spatio-temporal process that utilizes the description of atomic interaction to simulate atomic level perturbation in a system and calculate the observable macroscopic properties. Essentially, MD techniques study the equilibrium properties of classical many-body atomic and molecular system. Additionally, MD can also provide dynamical properties of a system such as time-dependent responses to perturbations, transport coefficients, rheological properties and spectra. The observable quantities are expressed as a function of the positions and momenta of the particles in the system. In this section, the basics of MD and potential models used in two MD simulation works are briefly outlined.

2.1 MD Fundamentals

MD technique iteratively solves the classical Newtonian equations of motion for the trajectories of N particles with mass m utilizing a potential model. The equations of motion for N particles can be written as

$$m_i \ddot{\boldsymbol{r}}_i(t) = \boldsymbol{F}_i(t), \qquad i = \{1 \dots N\} \tag{3.1}$$

where the force on particles *i* at time, F(t), depends on the positions of all other particles of the system at the time, and is given by

$$\boldsymbol{F}_i(t) = -\nabla_i \sum_{i=1}^{N} \sum_{j>i}^{N} V\left(r_{ij}(t)\right) \tag{3.2}$$

where $r_{ij}(t) = \left| r_i(t) - r_j(t) \right|$. The force on every particle is calculated using Equation 3.2, which is the most computationally expensive part of a MD simulation. Subsequently, the positions of the particles are updated using an integration algorithm. In this work, 'velocity Verlet' algorithm is used which has been modified to correctly include the velocities of the particles. The original Verlet algorithm[60] can be derived from Taylor expansion on time *t* of the coordinate of a particle, Equations 3.3 and 3.4:

$$\boldsymbol{r_i}(t + \Delta t) = \boldsymbol{r_i}(t) + \boldsymbol{v_i}(t)\Delta t + \frac{\boldsymbol{F_i}(t)}{2m_i}\Delta t^2 + \frac{\dddot{\boldsymbol{r}}_{\boldsymbol{i}}}{3!}\Delta t^3 + O(\Delta t^4) \tag{3.3}$$

$$\boldsymbol{r_i}(t - \Delta t) = \boldsymbol{r_i}(t) - \boldsymbol{v_i}(t)\Delta t + \frac{\boldsymbol{F_i}(t)}{2m_i}\Delta t^2 - \frac{\dddot{\boldsymbol{r}}_{\boldsymbol{i}}}{3!}\Delta t^3 + O(\Delta t^4) \tag{3.4}$$

Adding these equations give:

$$\boldsymbol{r_i}(t + \Delta t) \approx 2\boldsymbol{r_i}(t) - \boldsymbol{r_i}(t - \Delta t) + \frac{\boldsymbol{F_i}(t)}{2m_i}\Delta t^2 \tag{3.5}$$

which contains an error of order Δt^4.

The positions of the particles are updated each time step using Equation 3.5. Additionally, the velocity Verlet algorithm[61] updates the velocities using Equation 3.6:

$$\boldsymbol{v_i}(t + \Delta t) = \boldsymbol{v_i}(t) + \frac{\boldsymbol{F_i}(t + \Delta t) + \boldsymbol{F_i}(t)}{2m_i}\Delta t \tag{3.6}$$

The velocity Verlet algorithm generates identical trajectories as the original Verlet algorithm. In addition, it has the advantage of expressing positions and velocities of the

particles at the same instant of time. In this algorithm, the velocity for the next step can only be computed if the positions and forces at $t + \Delta t$ are known.

The simulations performed in this work are in orthogonal simulation cells. Periodic boundary conditions (PBC) are used in MD to avoid problems with boundary effects caused by finite size of the simulated system. PBC works by replicating the simulation box in all six faces. The application of PBC ensures that any atom that leaves a simulation box enters the simulation box from the opposite face of the simulation box. Figure 3-2 shows a schematic two-dimensional representation of PBC.

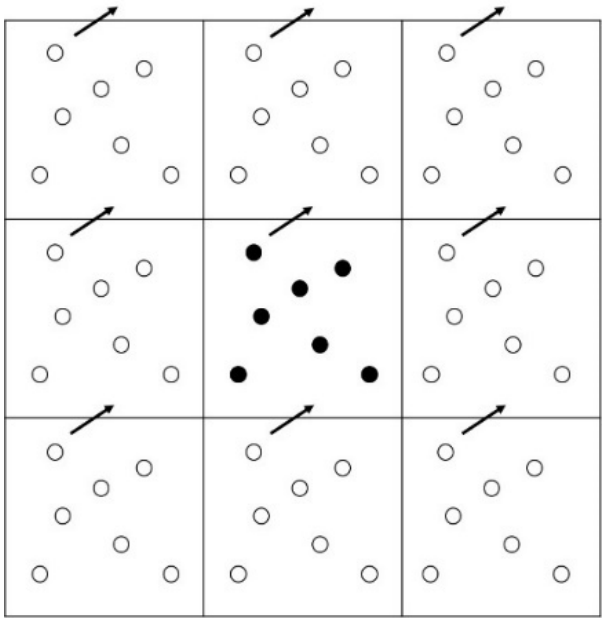

Figure 3-2. Periodic boundary conditions used in MD simulation

2.2 Potential Models

Two computational MD studies performed using classical and reactive MD potentials were:

I. Investigation of the composition-structure-property relationships of aluminoborosilicate glass compositions using classical MD potential.

II. Investigation of glass structures and reaction of water molecules on ternary sodium aluminosilicate glass surface using combination of Buckingham and reactive force field (ReaxFF) potentials in a reactive MD framework.

2.2.1. Pedone Potential

The simulation work of the composition-structure-property relationships of aluminoborosilicate glass was performed using a pair-wise inter-atomic empirical potential developed by Pedone et al.[62] From here on the potential is referred to as Pedone potential in this thesis. The potential is based on a rigid ionic model with partial charges to handle the covalent character of silicate systems. The potential is a generalized self-consistent force field which can model the structures and mechanical properties of silica-based glasses with different compositions. The potential function is shown in Equation 3.7:

$$U(r_{ij}) = D_{ij}\left[\left\{1 - e^{-a_{ij}(r_{ij}-r_0)}\right\}^2 - 1\right] + \frac{C_{ij}}{r_{ij}^{12}} + \frac{z_i z_j e^2}{r_{ij}} \qquad (3.7)$$

The first term represents short-range Morse function, the second term is repulsive contribution and the third terms is the long-range Coulomb potential. The physical meaning of the different parameters is defined as: D_{ij} is the bond dissociation energy, a_{ij} is a function of the slope of the potential energy well, and r_0 is the equilibrium bond distance. The parameters used in this work were derived by empirical fitting and are shown in Table 3-II. A proprietary boron-oxygen (B-O) pair potential was used, which was developed by Corning Inc®. The superscript numbers in the table are the partial charges assigned to the elements.

Table 3-II. Potential Parameters for Pedone Potential

Oxide	D_{ij} (eV)	a_{ij} (Å^{-2})	r_0 (Å)	C_{ij} (eVÅ^{12})
$Na^{0.6}$-$O^{-1.2}$	0.023363	1.763867	3.006315	5.0
$Ca^{1.2}$-$O^{-1.2}$	0.030211	2.241334	2.923245	5.0
$Ba^{1.2}$-$O^{-1.2}$	0.065011	1.547596	3.393410	5.0
$Zn^{1.2}$-$O^{-1.2}$	0.001221	3.150679	2.851850	1.0
$Al^{1.8}$-$O^{-1.2}$	0.361581	1.900442	2.164818	0.9
$Si^{2.4}$-$O^{-1.2}$	0.340554	2.006700	2.100000	1.0
$O^{-1.2}$-$O^{-1.2}$	0.042395	1.379316	3.618701	22.0[b]

[b] The term D/r^{12} is needed only in MD simulations and in free energy calculation at high temperature and pressure. In fact, the D_{OO} term can range between 22 and 100 eVÅ^{12} without altering the results of free energy minimization at room temperature.

2.2.2. Buckingham Potential

The Buckingham potential was used to simulate the initial bulk glass structure of sodium aluminosilicate glass for the glass surface-water reaction simulations. The potential was chosen for it simpler definition of atomic-pair interaction. The Buckingham-Coulombic potential form is shown in Equation 3.8:

$$V(r_{ij}) = Aexp\left(-\frac{r_{ij}}{\rho}\right) - \frac{C}{r_{ij}^6} + \frac{q_i q_j}{4\pi\varepsilon_0 r_{ij}} \tag{3.8}$$

where r_{ij} is the interatomic distance between atom pairs and A, ρ and C are variable parameters. Parameters A and ρ are thought to relate to the number of electrons and electron density, respectively, and C represents the van der Waal interaction. The first and second terms represent the short range attractive and repulsive potentials, respectively, while the last term accounts for the long-range Coulomb interaction. Table 3-III lists the parameters used in this work which were developed by Teter.[63] The O-O pair parameters was modified by Cormack and Du.[64] The superscripted numerical values represent the element charge used in the simulation.

Table 3-III. Teter Parameters used for Buckingham Potential

	A (eV)	ρ (Å)	C (eVÅ^6)
$Si^{2.4} - O^{-1.2}$	13.702905	0.193817	54.681
$Al^{1.8} - O^{-1.2}$	12201.417	0.195628	31.997
$Na^{0.6} - O^{-1.2}$	4383.7555	0.243838	30.7
$O^{-1.2} - O^{-1.2}$	2029.2195	0.343645	192.58

2.2.3. Reactive Force Field (ReaxFF) Potential

Reactive force field (ReaxFF) is a variable-charge bond order potential, where the total energy of the system is described by the partial energy contributions, as shown in Equation 3.9:

$$E_{system} = E_{bond} + E_{atom} + E_{lp} + E_{angle} + E_{coangle} + E_{hb} + E_{vdWaals} + E_{charge} + E_{coulomb} \quad (3.9)$$

where E_{sytem}, the energy of the system is a sum of E_{bond}, bond energy, E_{atom} represent the atomic energy, E_{lp} is the lone electron pair energy, E_{angle} is the valence angle energy, $E_{coangle}$ co-angle energy, E_{hb} is hydrogen bonding energy, E_{tors} torsional energy, $E_{vdwaals}$ is the van der Waals energy, E_{charge} is the charge equilibration energy, and $E_{coulomb}$ is the coulombic potential energy. The functional forms of the partial energy contributions are detailed in the original work.[65] ReaxFF potential is based on bond order, BO'_{ij}, with the fundamental assumption that the bond order between a pair of atoms can be directly calculated for the atomic distance r_{ij}, given in Equation 3.10. The three exponential terms represent a sigma bond, first pi bond and second pi bond, respectively. This bond order term is calculated on each simulation step to allow for breakage and formation of bonds.

$$BO'_{ij} = \exp\left[p_{bo,1} \cdot \left(\frac{r_{ij}}{r_o}\right)^{p_{bo,2}}\right] + \exp\left[p_{bo,3} \cdot \left(\frac{r_{ij}^{\pi}}{r_o}\right)^{p_{bo,4}}\right] + \exp\left[p_{bo,5} \cdot \left(\frac{r_{ij}^{\pi\pi}}{r_o}\right)^{p_{bo,6}}\right] \quad (3.10)$$

Additional assumptions that differentiate the application of ReaxFF in a reactive MD from classical MD approaches are:

1) Indistinguishability of particles, for example, oxygen atoms that may transition between water and glass cannot be labeled as members of a specific chemical species.
2) Application of the charge equilibration technique (QEq) introduced by Rappé and Goddard[66] to minimize the electrostatic charges by assigning partial charges based on ionization potential, electron affinities, and atomic radii.
3) Inclusion of dynamics neighbor lists for reordering of chemical species, even for bond interactions.

CHAPTER 4. CHEMICAL DURABILITY AND MECHANICAL PROPERTIES OF ALUMINOBOROSILICATE GLASSES

The aluminoborosilicate glasses used for PMT applications are chemically durable but, glasses in general are susceptible to acid-base reactions rather than electrochemical reactions involving redox reactions. This makes them especially vulnerable to attacks from polar molecules such as H_2O molecules. The aqueous environment of a neutrino detector, creates a unique and detrimental environment for the glasses that can lead to a premature failure of the glasses. A study of the chemical durability and mechanical properties of these glasses have not been extensively studied. The present work was designed to provide needed data on both.

In this chapter, results of the present study of the chemical durability and mechanical properties of commercial PMT and Alfred glasses are presented. The chemical durability is investigated using a static mode leaching experiments. The effects of high-purity water on mechanical properties (Vickers hardness and ring-on-ring biaxial flexural strength test) are investigated using a water simulation test. In addition, the surface chemistry and depth profiling on the glasses were performed using X-ray photoelectron spectroscopy (XPS) and wavelength dispersive X-ray spectroscopy (WDS), respectively. The goal of the work is to provide a background of the chemical durability and mechanical properties of aluminoborosilicate glasses for PMT application in WCDs.

1. Experimental Procedure

The composition of glasses and the bulk and powder sample preparation techniques used have been discussed in Chapter 3, Section 1. The details of static mode leaching experiment, water simulation test and characterization tools are presented below.

1.1 Static Mode Leaching Experiment

The static mode leaching experiment was designed to investigate the chemical durability of glasses. The product consistency test - B (PCT-B)[67] was adopted to study the effects of high-purity water at 14 ℃ and 25 ℃, which represent the optimal operational

temperature of the neutrino detector and room temperature condition, respectively. The PCT was developed to study the chemical durability of radioactive, mixed or simulated waste glasses. The time durations for the test were varied from 1, 5, 14 and 40 days. Although, the operational lifetime of a WCD is ~10-20 years, this study aims to provide the initial stages of effects of high-purity water on the aluminoborosilicate glasses used for PMT application.

The static mode leaching experiment was performed on powdered glass samples. The powdered glass samples were fabricated using methods described in Chapter 3, Section 1.2 and 1.4. The specific surface areas measured by 11–point (Brunauer–Emmett–Teller) BET analysis with nitrogen adsorption were 0·063±0.002 and 0·078±0·002 m^2/g for Alfred and Vendor1 glass, respectively. The static mode leaching experiment was carried out on 1 gm of glass powder with 31.5 mL and 39 mL of high-purity water for Alfred and Vendor1 glasses, respectively, in 125 mL capacity high density polyethylene (HDPE) sterilized containers with a surface area to volume ratio (S/V) of 2000 m^{-1}. The analytical grade water (resistivity 18.24 MΩ-cm and total organic carbon (TOC) < 30 µg/L) collected from Millipore, Elix – water purification system (Millipore Corporation, Bellerica, MA) was used for the leaching experiment. The solution used for the experiments was unbuffered. The rationale behind the use of unbuffered solution is that the pH in a water Cherenkov neutrino detector is not monitored.

A set of triplet tests were carried out at both temperatures and time durations including control samples, which consisted of only high-purity water in a HDPE container. At the end of each test, the solutions were filtered with 0.2 µm Millipore filters and collected for pH measurements and chemical analysis using inductively coupled plasma – optical emission spectroscopy (ICP-OES) (Perkin Elmer, Optima 8300, Waltham, MA). All the tests were performed at ambient pressure conditions.

1.2 Water Simulation Test

The water simulation test was designed to investigate the effects of high-purity water on the mechanical properties of glasses such as Vickers indentation and ring-on-ring biaxial flexural strength test. The disk-shaped glass samples were prepared by methods discussed in Sections 1.2 and 1.3. Multiple disk samples were vertically placed in a secure

three column stainless steel tray, which was immersed in a water bath system (Fisher Scientific™, IsoTemp™ 4100 R20, Waltham, MA) filled with high-purity water. The setup ensured sample separation and water access on all sides of the disc samples. The water bath was held at a constant temperature of 14 ℃. The time durations for the test were varied from 1, 5, 14 and 40 days. After completion of each test, samples were collected, air dried and stored in a desiccator before usage.

2. Instrumentation

2.1 Differential Scanning Calorimetry (DSC)

The glass transition temperature (Tg) for the glasses were determined using the differential scanning calorimetry (DSC, TA Instruments DSC 2910) to estimate an appropriate annealing schedule. Small shards of the vendor glasses were placed in a platinum pan alongside an empty pan acting as a standard. The samples were heated at a rate of 10 ℃ per minute from room temperature to 610 ℃ under a nitrogen atmosphere. The glass transition temperatures were estimated using the tangent intercept method on the temperature versus heat flow plot.

2.2 Mechanical Properties

2.2.1. Vickers Indentation

The Vickers indentations were measured using a Shimadzu indenter (Model HMV-2000, Shimadzu Corporation, Kyoto, Japan) following standardized method ASTM E384 – 99. The indentations were performed on planarized disk glass samples. In addition, the samples holder could account for small deviations of sample surface parallelism. Ten individual indentation measurements were performed at 200, 300, 500, and 1000 gf loads. The Vickers indenter was slowly lowered on to the sample surface and held for 15 s before unloading. The indenter created a square imprint on the glass surface, Figure 4-1, whose diameters were measured using an in-built micrometer and the Vickers hardness was calculated using Equation 4.1:

$$HV = \frac{1.8544\,F}{d^2} \tag{4.1}$$

where F = force in kgf and d = average of the two diagonals in μm.

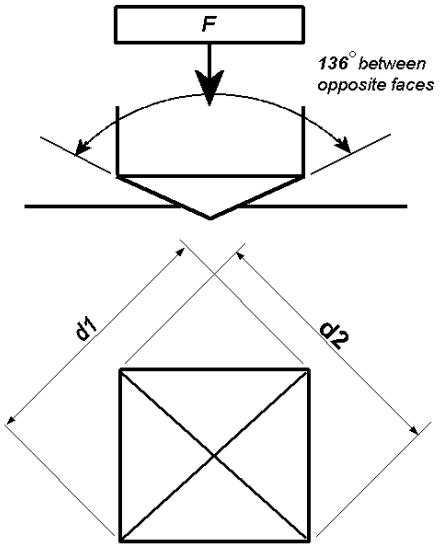

Figure 4-1. Schematic of Vickers indent

2.2.2. Ring-on-Ring (R-O-R) Biaxial Flexural Strength Test

A customized fixture attached to Instron 5566 (Model 5566P6016, Instron, Norwood, MA) was built to perform the R-O-R biaxial flexural strength test, shown in Figure 4-2. The specifications of the fixture were determined using ASTM C1499-08. The support (bottom) and load (top) rings were 25 mm and 10 mm in diameter. The disk glass samples were concentrically placed on support ring before applying load ring onto the samples. The load was applied on the sample at a displacement control rate of 0.5 mm/min. The load at failure was measured and equibiaxial failure stress was calculated as follows:

$$\sigma_f = \frac{3F}{2\pi t^2}\left[(1+\upsilon)\ln\left(\frac{D_S}{D_L}\right) + (1-\upsilon)\frac{(D_S^2 - D_L^2)}{2D^2}\right] \tag{4.2}$$

where F = the applied force in N, υ = the Poisson's ratio, D_S = diameter of the support ring in mm, D_L = diameter of the loading ring in mm, D = radius of the glass sample in mm, and t = the thickness of the sample in mm. The R-O-R biaxial flexural strength test is a destructive method, thus an average of thirty samples were tested for analysis. The data was analyzed using Weibull statistics.

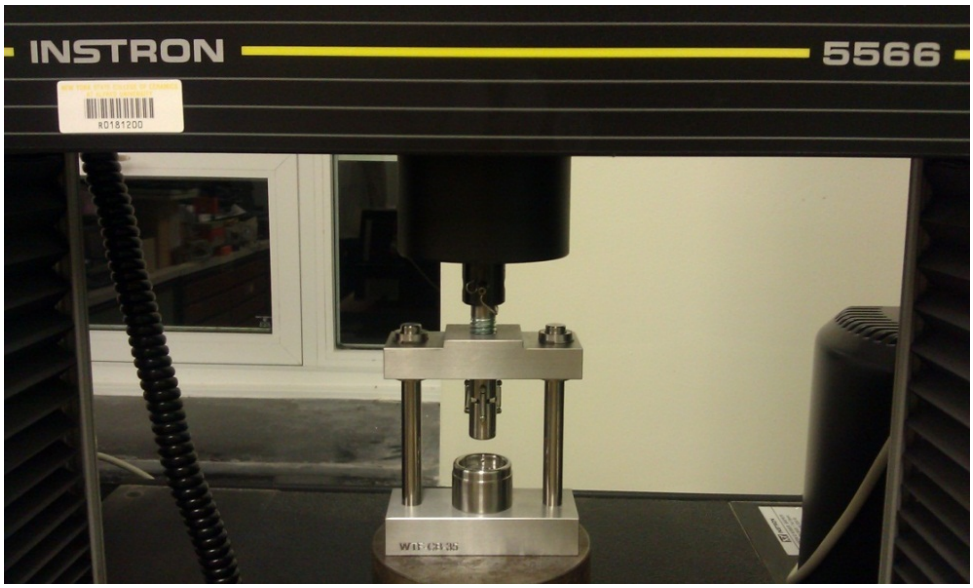

Figure 4-2. Customized fixture attached to Instron-5566 to measure the ring-on-ring biaxial flexural strength test

2.3 Inductively Coupled Plasma – Optical Emission Spectroscopy (ICP-OES)

Inductively coupled plasma – optical emission spectroscopy (ICP-OES) (Perkin Elmer, Optima 8300, Waltham, MA) technique was used to investigate the elemental ions release. The analysis was performed on the filtered and undiluted solutions collected from the static mode leaching experiments. The ICP-OES technique is inherently qualitative, thus a standard calibration curve was created for a known concentration of each element to generate quantitative data. To achieve this, the intensities measured for the elements in the sample solution are mapped to the calibration curve to estimate concentration of the elements. The normalized mass losses NL_i (gm^{-2}) were calculated using the relationship:

$$NL_i = \frac{C_i}{x_i\, S/V} \tag{4.3}$$

where C_i (mg·l^{-1}) is the concentration of element i in the solution and x_i is the mass fraction of element i in the glass, and S/V is the glass-surface-area-to-solution-volume ratio (m^{-1}) used in the static mode leaching experiments. The result is expressed in gm^{-2}. The normalized mass loss is used to evaluate the amount of altered glass calculated for B and Na ions. In addition, the pH of the solution was also measured.

2.4 X-ray Photoelectron Spectroscopy (XPS)

X-ray photoelectron spectroscopy (The Kratos Ultra XPS, Manchester, UK) was used to survey and high-resolution scans of Alfred and Vendor1 glasses. The survey scans were collected for as-prepared and 1, 5, 14, and 40 days water simulation tested glasses. A monochromatic Al K-α (1486.6 eV) was used for incident X-ray beam with a beam diameter of 100 μm. Three sequential narrow scans of the O 1s, Si 2p, B 1s, Al 2p, Na 1s, Ca 2p, and C 1s were collected using 40 eV pass energy with spectral resolution of 0.2 eV. A low-energy electron gun was used to compensate for surface charging. The binding energy scale was referenced to C 1s line of aliphatic adventitious carbon, set at 284.6 eV, observed due to adsorption of hydrocarbon impurities. The narrow scans were performed on 14 and 40 days glass samples.

2.5 Wavelength Dispersive X-ray Spectroscopy (WDS)

Wavelength dispersive X-ray spectroscopy (WDS) (JEOL, JXA-8200, 2004) was used to generate line profiles for elemental analysis. The elemental line profile scans were performed using an energy of the electron beam of 8 KeV compared to more common 15 KeV energy. The low energy of the beam was chosen because it could create a smaller interaction volume for the incident beam, especially for a low-density material such as glass. The probe diameter was based on a zero (pin-point) beam diameter. A 200 × 30 point scans with 2 dimensional shifts of 0.0977 μm. The dwell time for each scan was 500 ms. The WDS scans were performed on a cross section of a fractured piece of R-O-R

biaxial flexural test glass. The fractured piece was held on a hardened epoxy resin and polished down to 1 μm diamond paste with mineral oil as a grinding and polishing media.

3. Results

3.1 Property Comparison of Commerical PMT Glasses

Initially, the properties of two commercial PMT glasses were investigated. The X-ray diffraction plots of melted commercial glasses showed no crystallization or phase separation, Chapter 10, Figure 10-1. The density of the commercial PMT glasses were measured using the kerosene immersion technique which yielded 2.42 and 2.33 g/cm^3 for Vendor1 and Vendor2 glasses, respectively. The T_g for the Vendor1 and Vendor2 glasses were measured at 554.4 ℃ and 510.5 ℃, respectively. The T_g was used as the basis for choosing annealing schedules for the glasses throughout this work.

Figure 4-3 shows Vickers hardness of two commercial PMT glasses, Vendor1 and Vendor2. Ten indents were made for each load and the standard deviations are shown in the figure. The observed hardness for Vendor1 glass was higher than Vendor2 glass for all four tested loads. Both the vendor glasses showed decreasing hardness for higher indentation loads. This is an expected behavior of glasses in general, and may be attributed to the relaxation of local stress created due to the indenter. The relaxation occurs as a plastic response to higher load, which is accompanied by cracking behavior. The hardness comparison suggests that Vendor1 has better response to surface stress.

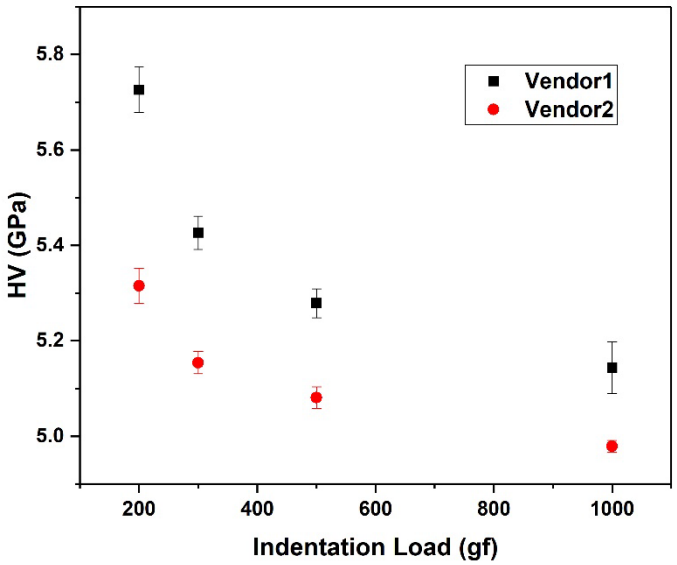

Figure 4-3. Vickers hardness comparison for two commercial PMT glasses

Figure 4-4 shows the Weibull plot for Vendor1 and Vendor2 glasses. Thirty samples were tested for Vendor1 glass while twenty-four samples were tested for Vendor2 glasses. The x-axis is in logarithmic scale while y-axis is in the double log reciprocal scale. The conversion of axes in these scales linearizes the cumulative distribution function which can then be analyzed using a linear fit. The linear regression of Weibull plot provides two essential parameters, Weibull modulus (m) and characteristic strength (σ_o) to analyze failure data. The Weibull modulus is the slope of the linear fit and indicates the reliability of the data. In an ideal case of perfectly uniform flaw population, the Weibull modulus would approach its theoretical upper limit of $m \rightarrow \infty$. A large value of m indicates a greater predictability and hence, a greater reliability. The characteristic strength is defined as the strength at which there is a 63.2% probability of failure of a given sample. Higher characteristic strength means a higher resistance to the biaxial flexural stress.

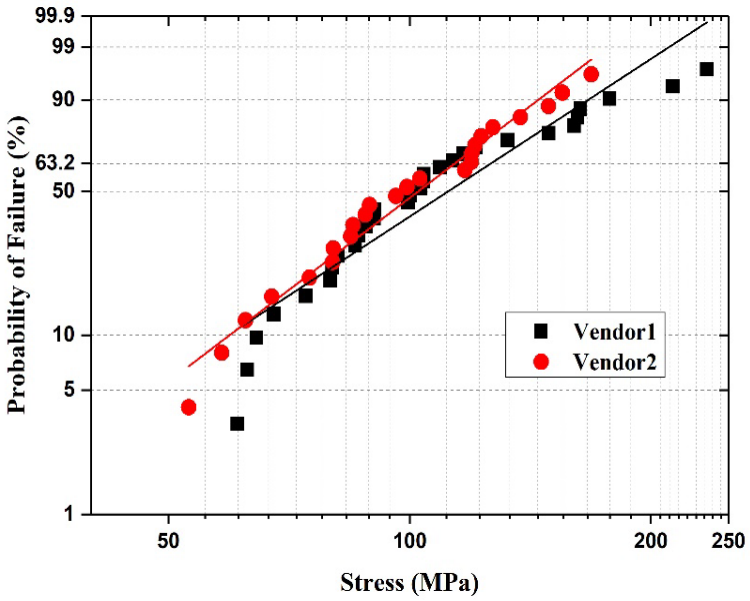

Figure 4-4. Weibull plot for Vendor 1 and Vendor 2 glasses

Table 4-I shows the Weibull parameters calculated for Vendor1 and Vendor2 glasses. 30 and 24 samples were tested for Vendor1 and Vendor2 glasses respectively. Vendor1 glass has higher characteristic strength, 126.28 MPa than Vendor2 glass, 113.86 MPa. Although Vendor1 has higher characteristic strength than Vendor2, the Weibull modulus of Vendor1, 2.98, is slightly lower than Vendor2, 3.47. The two commercial PMT glasses have comparable strength and Weibull modulus, which are highlighted in superimposed data points in Figure 4-4. In addition, the scatter of the flexural strength data for glasses depends on the surface finish, which strongly correlates to the presence of flaws and subsurface level damage during processing. Almost all of the R-O-R tested samples were found to have fracture origin at the surface of the glass. The initial comparison of the two commercial PMT glasses suggests that these glasses have similar thermal and mechanical properties.

The R-O-R test is a destructive test. Figures 4-5 (a), (b) and (c) show the sample before R-O-R test, after R-O-R test and optical image of fracture surface. The optical image of fractured surface suggests that the location of the fracture origin is at the surface of the glass samples. The fracture origin is center dark spot while the reflective region is

the fracture mirror. The edges of the fracture mirror are marked by heckle lines. The majority of glasses failed due to a flaw at the surface.

Table 4-I. Weibull Parameters for Commercial PMT Glasses

Glass Composition	Weibull modulus (*m*)	Characteristic Strength, σ_o (MPa)
Vendor1	2.98	126.28
Vendor2	3.47	113.86

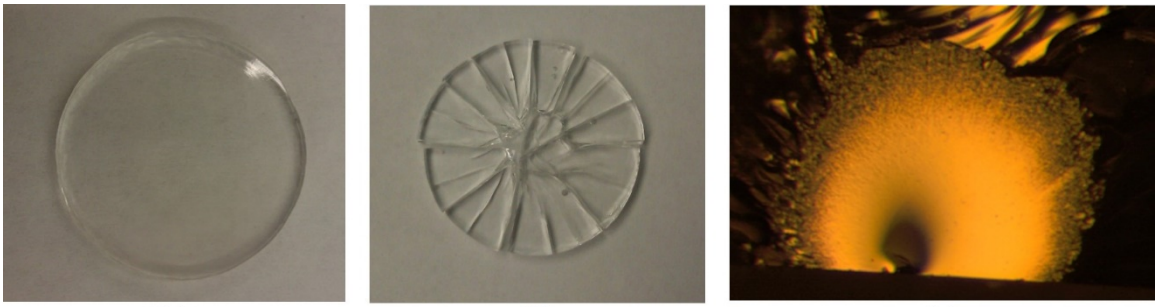

Figure 4-5. (a) Image of a R-O-R test glass sample, (b) glass sample after R-O-R test, and (c) Image of fracture mirror of a tested sample

Figure 4-6 shows the distribution of failure stress calculated from the R-O-R biaxial flexural strength test to the sample thickness. The data suggests that the sample thickness does not affect the strength of the glasses for this test method. The calculated mean failure stress of Vendor1 and Vendor2 glasses were 112.56±43.99 MPa, and 102.41±31.43 MPa, respectively. The lowest failure stress recorded for Vendor1 glass was 60.99 MPa with sample thickness of 3.235 mm and Vendor2 glass, it was 60.99 MPa. The highest flexural stress was 235.09 MPa for Vendor1 glass sample with thickness of 2.7925 mm. For further property testing, only Vendor1 glass was chosen primarily due to the ease of melting and processing of the glass.

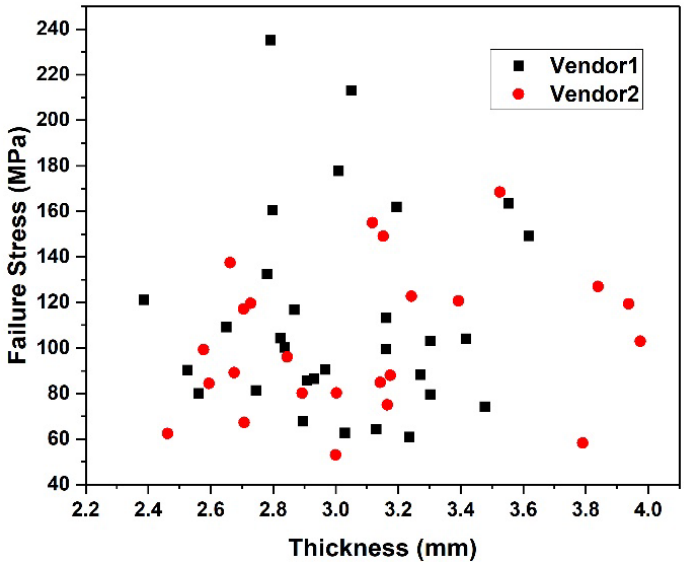

Figure 4-6. Scatter plot showing the thickness of a tested sample and the associated failure stress.

3.2 Static Mode Leaching Test - Chemical Analyses

3.2.1. pH

Figure 4-7 shows the pH measured for Vendor1 and Alfred glasses at 14 ℃ and 25 ℃ for various test durations. The x-axis is the time periods in days and the y-axis is the measured pH at different test periods. All the pH measurements were performed at room temperature. The pH of high-purity water as is, was 5.63±0.08, indicating an acidic condition. The pH measured for the two glasses immersed at different temperatures conditions were significantly higher than the pH of initial high-purity water. After 1 day test period, the pH ~6.4 for Vendor glass and ~6.6 for Alfred glass. The initial increase of pH can be attributed to the release of glass components into the water media. Following the increase of pH for 1 day test period, the pH at 14 days test periods did not show dramatic increase. The pH increases ~6.9 for 14 ℃ and ~7.2 for 25 ℃ after 14 days test periods. The pH measured at 25 ℃ is marginally higher than for 14 ℃. The difference of pH for two temperature conditions can be attributed to higher kinetic activity of chemical exchange between glass and water at higher temperature. For the durations of the testing in this work, the pH increased to neutral pH conditions.

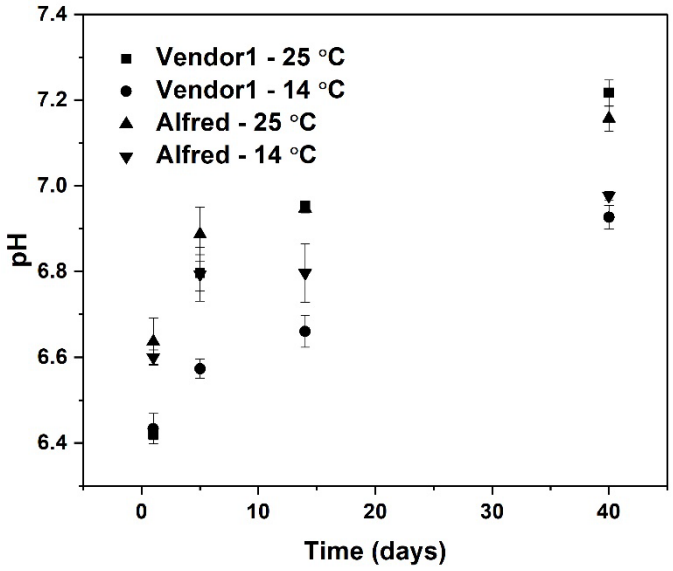

Figure 4-7. Time evolution of pH of vendor and Alfred glasses at 14 ℃ and 25 ℃.

3.2.2. Ion-Release

Figures 4-8 (a), (b) and (c) show the normalized mass loss (NL_i) behavior of Na, B, and Si ions for static mode leaching test. The units are expressed in $mg \cdot m^{-2}$ or $10^{-3} gm^{-2}$. The error bars shown in the graphs herein are ±1 standard deviation for the triplet test. For the elements shown in the Figures 4-8, higher amount of mass loss was recorded for longer time durations. In Figure 4-8 (a), the Na ion release is higher for static mode leaching experiment performed at 25 ℃ than 14 ℃. An increase in temperature can significantly affect the kinetics between the glass and water. The Na ion release at 14 ℃ is similar for Vendor1 and Alfred glasses; however, at 25 ℃, it is much higher for Vendor1 glass than Alfred glass. The ion release behavior of Alfred glass showed less temperature dependence than Vendor1 glass.

Similar normalized mass loss was measured for B and Si shown in Figures 4-8 (b) and (c), respectively. The ion release at 25 ℃ was higher compared to 14 ℃ and at 25 ℃, Vendor1 glass ion release was higher compared to Alfred glass. In addition, the normalized mass loss for Na > B > Si was observed for the leaching test. The higher normalized mass loss of Na and B for both glasses suggests the formation of dealkalized and deboronated layer at the glass surface. The higher ion release for Na can be attributed to the bonding

environment of Na in the glass. The Na ions are loosely bonded in a glass network, thus are readily released in contact with water. The Si and B form the glass network; however, the higher amount of release of B compared to Si have been reported for many borosilicate glasses. The ion release of Al, Ca and Zn were negligible and below instrumental detection limit.

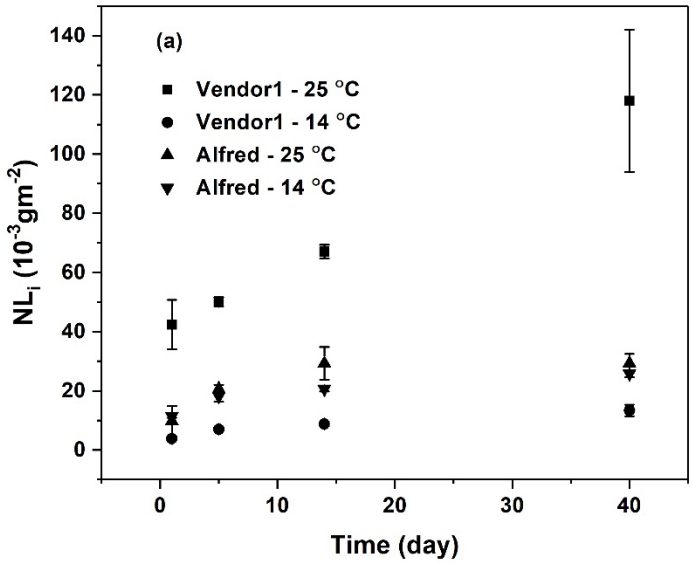

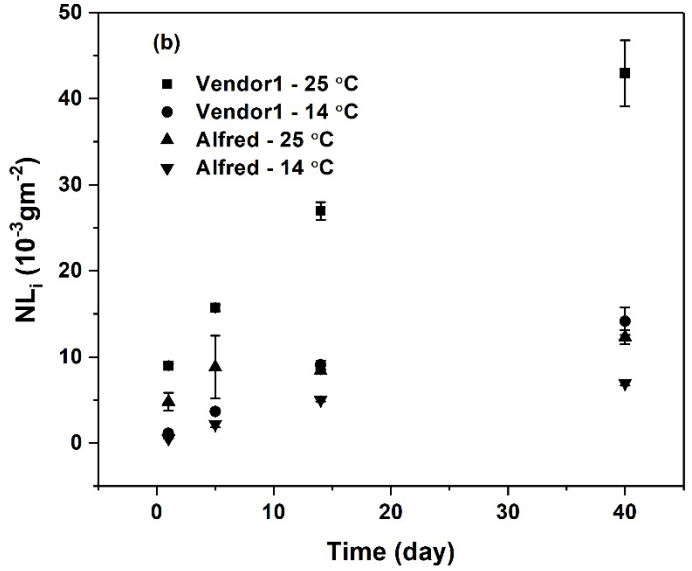

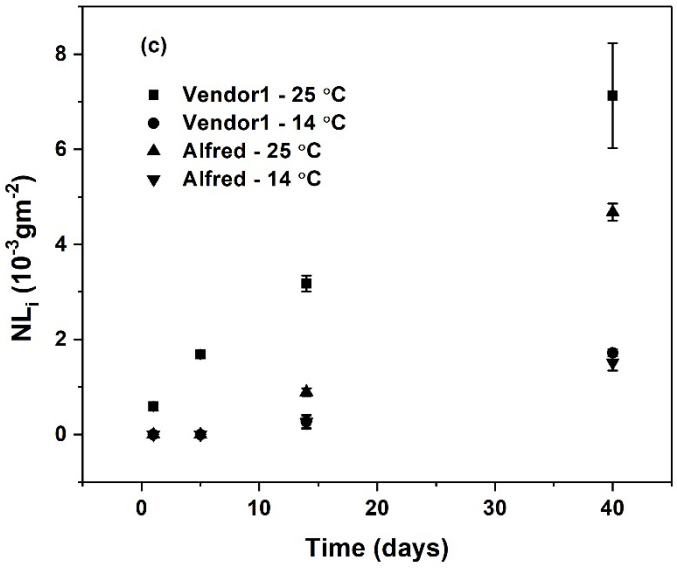

Figure 4-8. Normalized mass loss of: (a) Na, (b) B, and (c) Si

Figure 4-9 shows the normalized mass loss of Ba ion for Vendor1 glass at 14 ℃ and 25 ℃. The normalized mass loss for Ba ion at 25 ℃ was greater by a factor of 20 than at 14 ℃. This shows a pronounced temperature dependence for Ba ions, which was also observed for Na, B and Si ions.

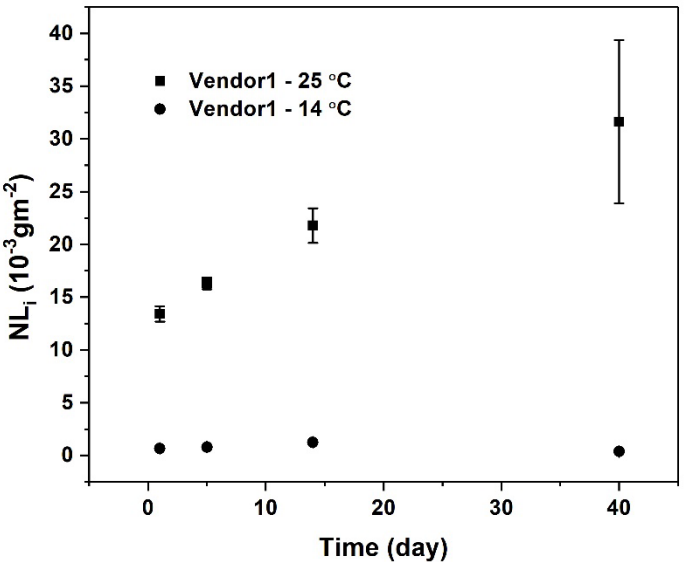

Figure 4-9. Normalized mass loss of Ba ion for Vendor1 glass

3.3 Water Simulation Test

3.3.1. Indentation Hardness

Figure 4-10 (a) and (b) show Vickers hardness (Hv) for Vendor1 and Alfred glasses, respectively. The hardness was tested on glasses before and after the water simulation tests. The x-axis represents the loads used for the indentation in gram-force (gf) and y-axis shows the Vickers hardness in GPa. An average of ten indents were performed on the disk glasses after 1, 5, 14 and 40 days test durations. In general, the hardness is lower for higher loads. The decrease in hardness for both glasses with respect to load is a typically expected behavior of glasses.

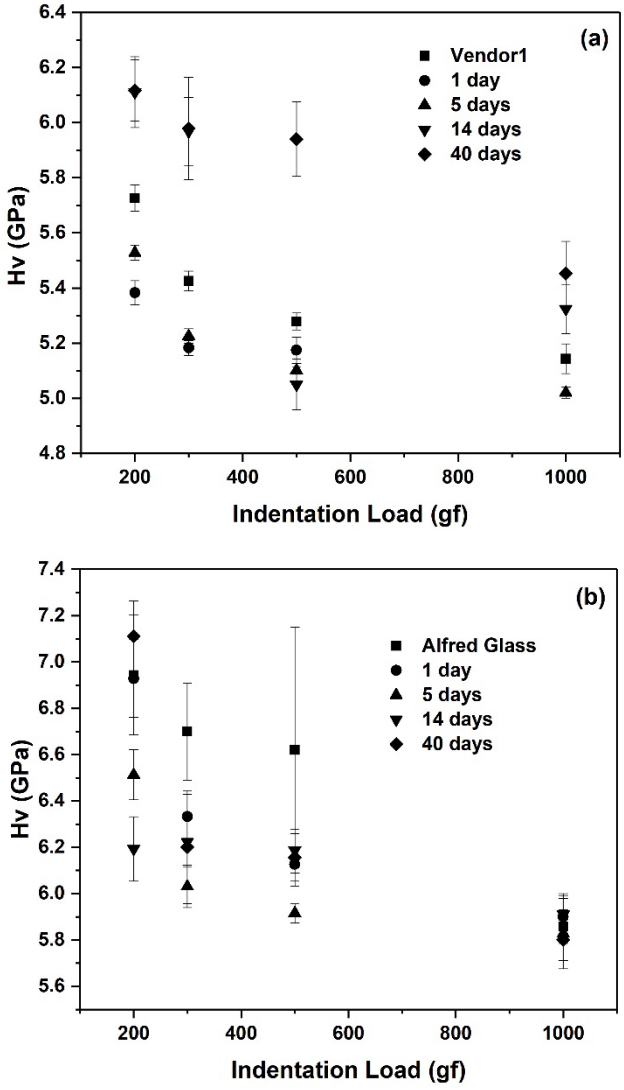

Figure 4-10. Vickers hardness for: (a) Vendor1 glass and (b) Alfred glass

3.3.2. Ring-on-Ring (R-O-R) Biaxial Flexural Strength Test

The R-O-R biaxial flexural test was investigated using Weibull analysis. Figure 4-11 (a) and (b) show Weibull plots for Alfred and Vendor1 glasses, respectively, for glasses before the water simulation test and after 40 days test duration. The explanation for the choices of Weibull plot axes were discussed in Section 4.1. The R-O-R test was not performed for 1, 5 and 14 days as the time duration would not be sufficient to significantly influence the flexural strength of the glasses. The Weibull parameter for the data sets are shown in Table 4-II. The Weibull plot shows that after 40 days of test the characteristic strength increased by 10.02%. The Weibull modulus for Alfred glass increased from 3.02 to 5.65 indicating that the failure stress has a much tighter fit, thus a greater reliability of the data set. On the contrary, the characteristic strength of Vendor1 glass decreased from 126.68 to 96.24 MPa for glass samples before and after 40 days water simulation test, respectively. The characteristic strength decreased by 24.04%, which is a significant amount. For Vendor glass, the Weibull modulus improved from 2.98 to 3.42, indicating greater reliability of the data set. The tightening of the spread of the data for 40 days tested glasses can be attributed to the smoothening of the sharp surface flaws, therefore creating a more uniform distribution of the surface flaws. As discussed earlier, in an ideal case with a perfectly uniform flaw population, the Weibull modulus would approach its theoretical upper limit of $m \rightarrow \infty$. Note that the modulus is on the lower end of reported values.

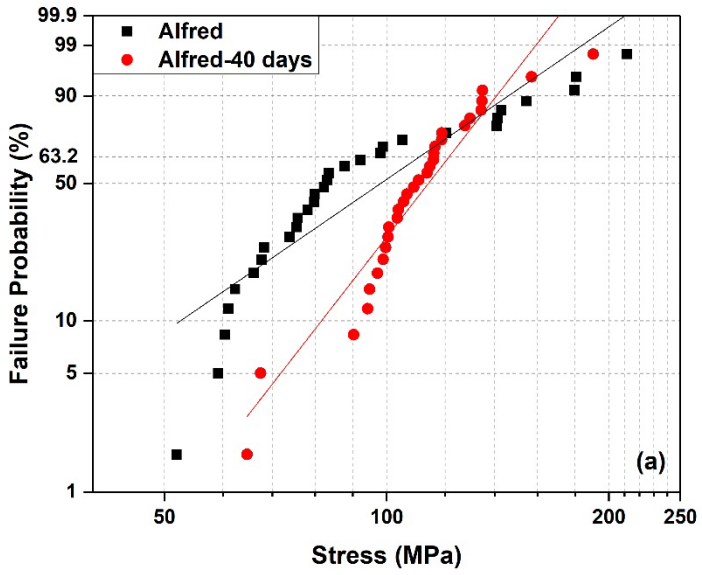

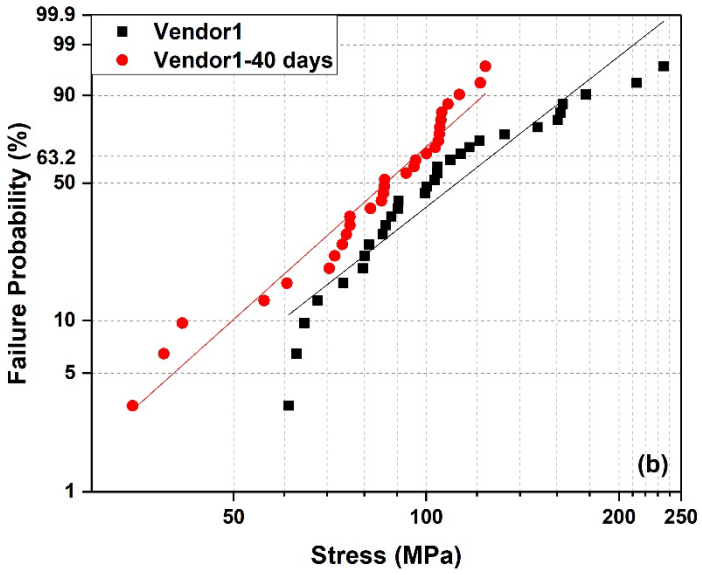

Figure 4-11. Weibull plot of probability of failure for: (a) Alfred glass and (b) Vendor1 glass.

Table 4-II. Weibull Parameters for Alfred and Vendor1 Glasses

Glass	Weibull modulus (*m*)	Characteristic Strength, σ_o (MPa)
Alfred	3.02	110.83
Alfred-40 days	5.65	121.94
Vendor1	2.98	126.68
Vendor1-40 days	3.42	96.24

3.3.3. Wavelength Dispersive X-ray Spectroscopy (WDS)

WDS was used to generate the elemental line profile for glasses tested for 40 days only. The line profile was calculated from an average of 30 scans for each element. Figure 4-12 shows elemental line profile of B, Al and Na for Alfred glass. The Al profile has a sharp cutoff about the scan length of 7 µm indicating the edge of the sample and suggesting less Al leached out of the glass. Compared to Al line profile, the B and Na line profiles do not show a sharp cutoff, suggesting that the B and Na concentrations are lower at the edge of the glass and was possibly leached out due to contact with water. The static mode leaching experiment showed release of Na and B atoms from the glass in presence of high-

purity water. Additionally, the inset graph shows the line profile for Si. Si profile also shows a clear cutoff between 6 and 8 μm scan length. Although the Si shows apparent loss at the surface, the interaction volume of the incident beam could possibly askew the results obtained using WDS technique.

Figure 4-13 shows similar elemental line profiles generated for Vendor1 glass. For this glass, the Si (inset graph), Al and Ba show sharp cutoff edges indicating the surface of the glass and suggesting low amount of elemental release from the glass. B and Na line profiles show gradual change in intensity, suggesting depletion of these elements at the surface. The counts per second (cps) for B, Al and Na were low compared to Si. This is due to the concentration of these elements in the Alfred glass, the elemental response to the incident beam and the low energy of the incident beam used for the glass sample. The low energy of the incident beam creates a smaller interaction volume specially in a low-density material such as glass.

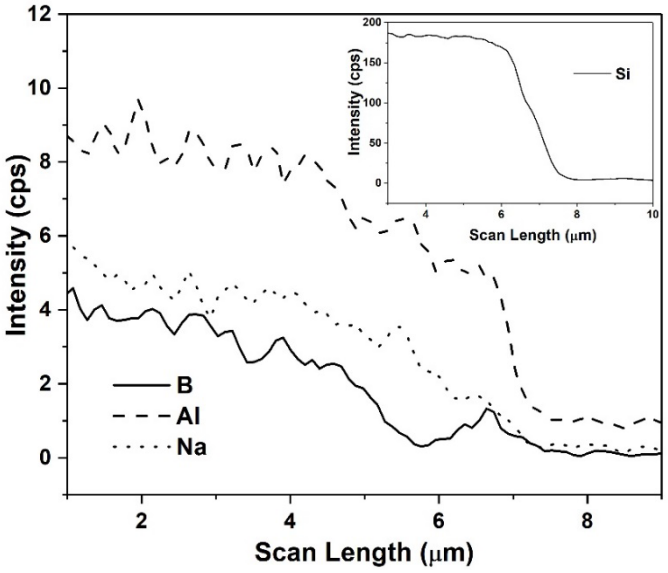

Figure 4-12. Elemental line profile of Alfred glass.

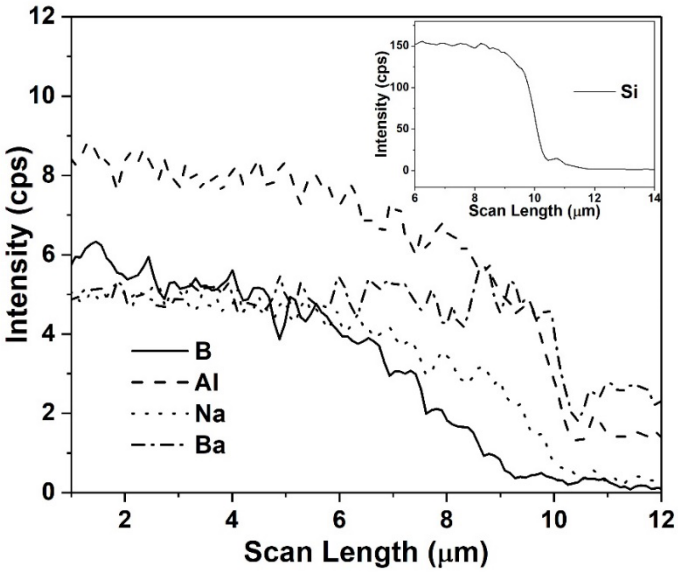

Figure 4-13. Elemental line profile for Vendor1 glass.

3.3.4. X-ray Photoelectron Specroscopy (XPS)

Figure 4-14 (a) and (b) show the survey scans of the surface of the Alfred and Vendor1 glasses, respectively. The survey scans were performed on as-prepared and 1, 5, 14, and 40 days water simulation tested glasses. The binding energy of the elements of interest are identified the graph. For Alfred glasses, the prominent peaks are observed for Si 2s, Si 2p, Na 1s, Na-KLL, O 1s and Al 2p. On the contrary, the B 1s peak is relatively small. In addition to the XPS peaks for glass components, C 1s was also observed due to adsorption of hydrocarbon impurities on the surface. Similar peaks and intensities were observed for Vendor1 glasses. Additionally, in Figure 4-15 (b), the peaks for Ca 2p, Zn 2p3 and Ba 3d5 are identified.

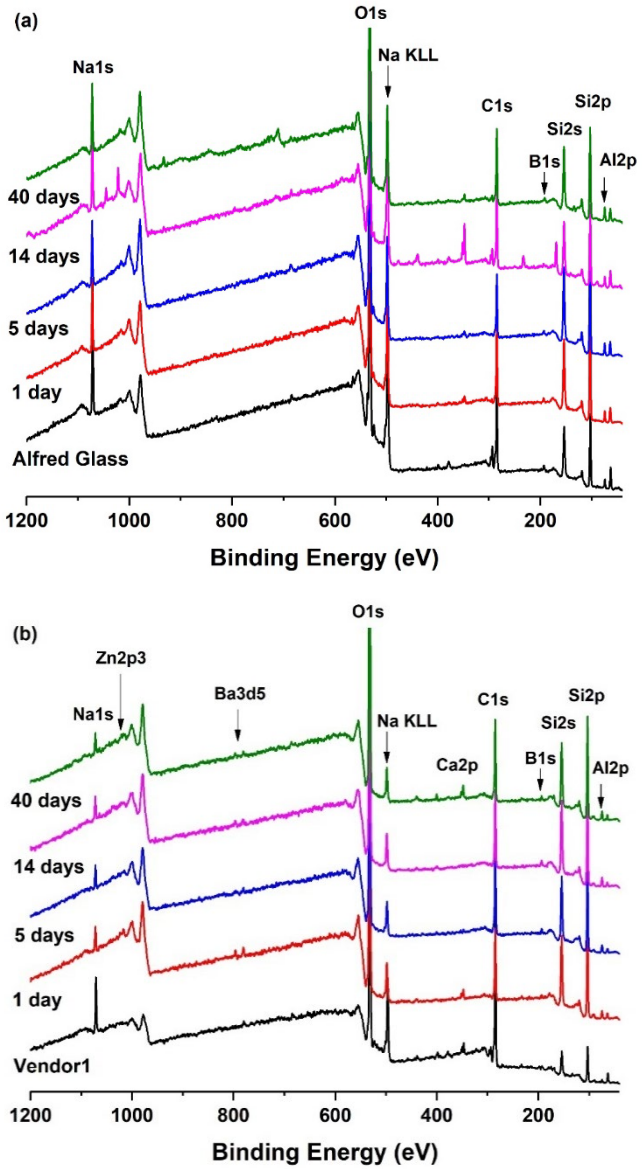

Figure 4-14. XPS survey scans for (a) Alfred glass and (b) Vendor1 glass.

The high-resolution scans of Vendor1 glasses were performed on as-prepared (not treated) glass and 14, and 40 days water simulation tested glasses. Figure 4-15 shows high-resolution XPS peaks for (a) Si 2p, (b) B 1s, (c) Al 2p, and (d) O 1s. The x-axis represents the binding energy of the electrons in eV. The measured XPS peaks are symmetric. The O 1s includes contributions from bridging oxygens (BO) e.g., Si-O-Si, Si-O-Al, Si-O-B and non-bridging oxygens (NBO), e.g., Si-O-R, Al-O-R, and B-O-R; where R = Na, Ca, Ba. The deconvolution of these peaks is difficult due to spectra without any features. The

vertical line in each figure represents the maximum point of the XPS spectra for the as prepared glass samples.

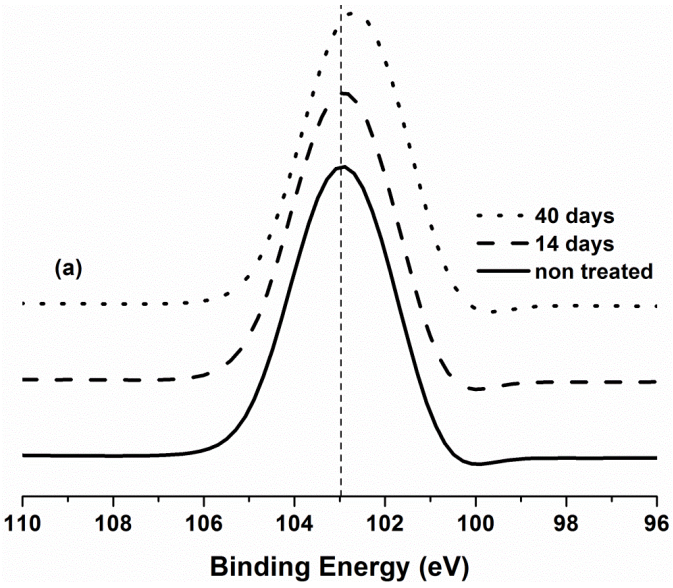

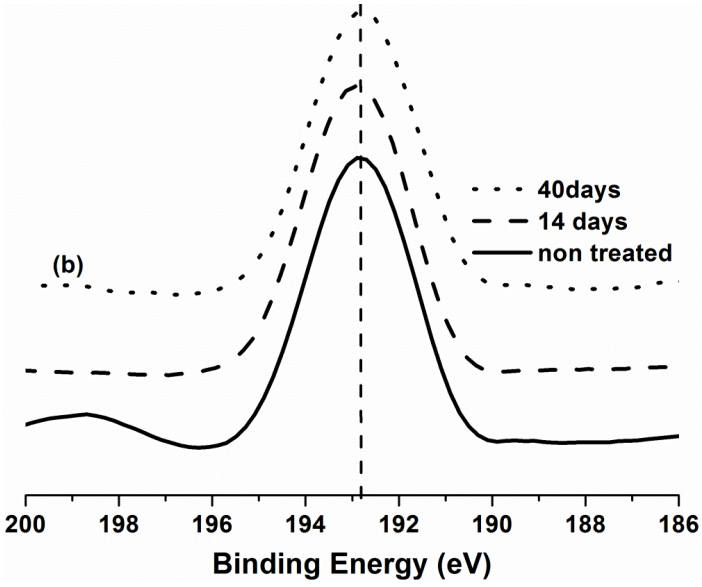

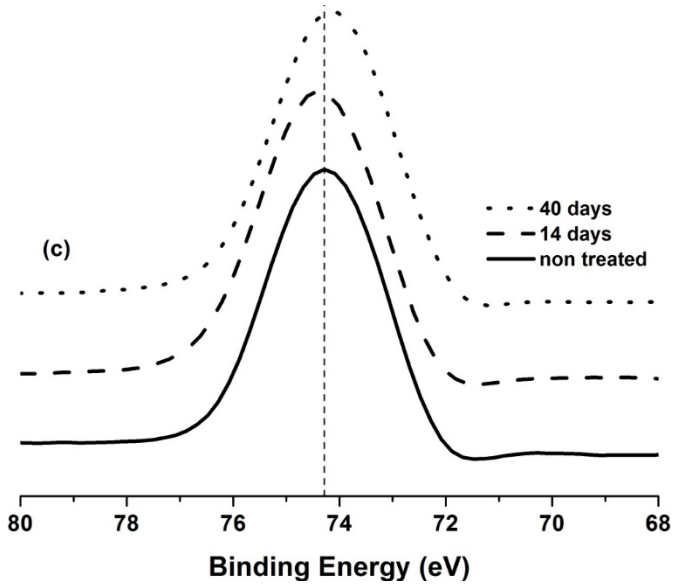

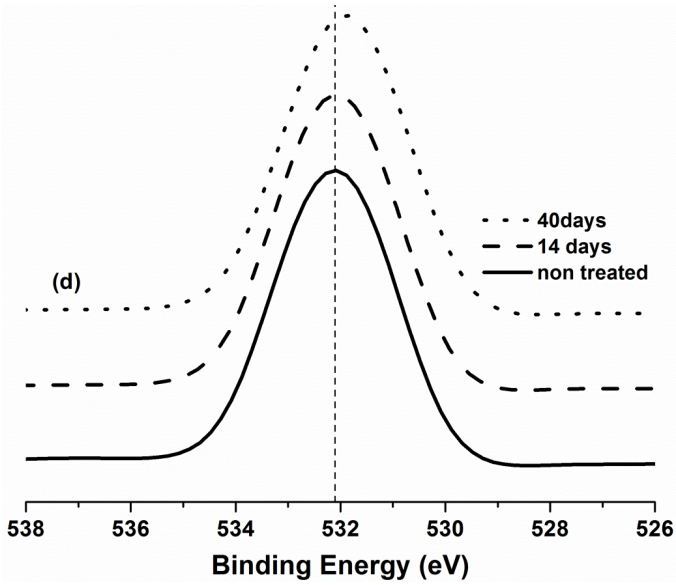

Figure 4-15. High resolution scan of (a) Si2p, (b) B1s, (c) Al2p, and (d) O1s.

The peak shifts are minimal in all scans as shown in Figure 4.16 (a) O 1s and Si 2p and (b) Al 2p and B 1s. O 1s and Si 2p binding energy (BE) values show a linear decrease suggesting simultaneous local structure changes. Al 2p and B 1s XPS peaks also indicate a small decrease in BE with increasing time duration of water simulation test. This decrease is, however, not linear. This decrease of BE to lower energy after 14 and 40 days water exposure suggests and local electronic structure changes due to interaction with

water at the surface of the glass. Table 4-III shows ratios of XPS peak areas of Al, B, and Na to Si. The Na/Si and B/Si show a decreasing trend, which can be attributed to the initial ion exchange process that typically results in depletion of Na and B from the surface confirmed by our ICP results. Since Al is retained in the glass surface during this period, an increase in Al/Si is observed. This shows that the Na and B leached out of the glass surface for vendor glass.

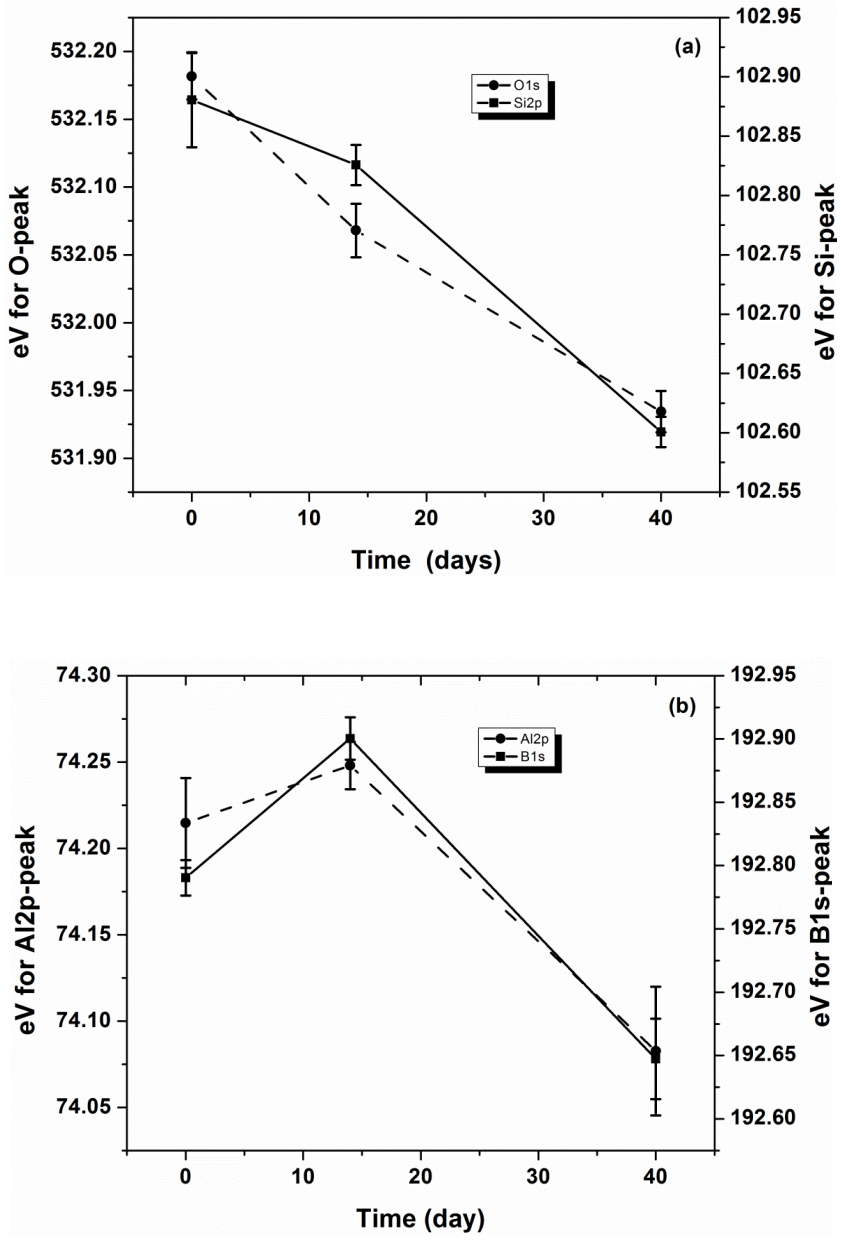

Figure 4-16. Carbon corrected peak positions for (a) O1s and Si2p, (b) Al2p and B1s.

Table 4-III. Area Ratio Calculated from XPS Measurements

Time(days)	Al/Si	error	B/Si	error	Na/Si	error
Initial	0.063	0.001	0.077	0.002	0.460	0.009
14	0.077	0.001	0.065	0.001	0.088	0.004
40	0.076	0.001	0.068	0.001	0.074	0.003

4. Discussion

4.1 Mechanical Properties

The Vickers hardness is a surface property while the flexural strength is a property of the bulk glass. The increase in hardness in the surface of PMTs could reduce the severity of damage caused during handling and placement within the detector system. In general, a hardness value decreased with increasing load for all tested samples. The Vickers hardness results showed an apparent increase in hardness for lower indentation loads (200, 300 gf) for both glasses. The hardness measure after exposure to water showed decrease in the hardness, this could be due to the depletion in Na, B and Si ions at the surface, which would affect to surface chemistry of the glass.

As ring-on-ring test is a bulk strength property measurement, the mechanical behavior of the glass is influenced by presence of critical flaws at the surface. The data from R-O-R test shows low Weibull modulus indicating influence of flaws. The decrease of characteristic strength of Vendor1 glass after 40 days exposure to water through the sharpening on the critical surface flaw. The increase in characteristic strength of Alfred glass could be due to the initial flaw size present at the surface. However, the changes in the strength must be considered while designing future water-Cherenkov neutrino detection projects. The depth effect due to water attack on glass surface depends on various parameters: glass composition, pH, time, temperature, solution saturation.

The preferential ion-leaching of more mobile ions from multicomponent glass systems by ion-exchange process is controlled by the diffusion of hydrogen ion (H^+) and hydronium ion (H_3O^+). Relatively mobile modifier ions are susceptible to the ion-exchange reaction. Additionally, boron is also observed to leach out of the surface leaving an dealkalized and deboronated glass surface. WDS concentration profiles also support

this formation of de-alkalized and deboronated layer formed at the surface of the glass. In addition, small shits of high resolution XPS peaks suggests changes in surface chemistry.

4.2 pH and Temperature Coupling Effect

The initial alteration mechanism affecting glass surface by water is ion exchange and interdiffusion between the protonated species (H^+, H_3O^+) in solution and network-modifying cations in the glass. It has been shown that simultaneous hydrolysis process of nucleophilic attack by OH^- occurs on network forming bonds (Si-O-Si, Si-O-Al, Si-O-B). The interdiffusion and hydrolysis processes result in release of Na, Ba, B, and Si ions from these glasses.[68] The immediate release of B suggests vulnerable B network at the surface, thus interacting with water molecules during initial interaction.

In addition, no Al ion release was detected in our study, in the glasses Al tetrahedral units would be homogeneously distributed. It is known that Al, which forms charged tetrahedral units [$AlO_{4/2}$] with modifier ion as charge compensators, polymerizes and hardens the glass network structure by decreasing NBO, as shown by our NBO estimation in Table 4-IV. In our work, the lack of Al ion release suggests Al retention on the modified surface for both glasses and both tests. Addition of Al in the glass reduces alkali exchange because of stronger bond between Al-tetrahedral. The lower amount of ion release corresponds to shallower depths of the glass surface interaction with water. The subsequent hydrolysis of silicate network is observed, which is dependent on glass composition.

The non-steady state ion release behavior suggests the test duration is not enough to observe this effect at these low temperatures. It is shown that in a test duration of 7 days steady state reaction has been observed at 90 ℃. The significant difference in normalized ion-release behavior of ions at 25 ℃ compared to 14 ℃ suggests thermodynamic effect at the surface of glass, although this increased release does not lead to any significant changes on the surface. In addition, the higher pH value also influence the solution chemistry and thus affects the ion-release behavior of the glass constituents.

4.3 Glass Structure and NBO

The structure of aluminoborosilicate glasses is more complicated compared to well-developed borosilicate structures due to complex role of Al_2O_3. We draw corollary structural discussion with triple quantum magic angle spinning nuclear magnetic resonance (3Q-MAS NMR) work on sodium aluminoborosilicate glass of pristine sodium aluminoborosilicate glass[69] with composition (mol%): $14Na_2O.4Al_2O_3.17B_2O_3.65SiO_2$ to assume possible structures of Alfred glass (mol%): $13.5Na_2O.5.5Al_2O_3.13B_2O_3.68SiO_2$. According to this structural study: 1) NBO contribution to Si-O-Na and B-O-Na are indistinguishable, 2) the excess Na to Al resulted in superposed Si[B]-O-Na and Si-O-Al site attributed to compensation of 4-coordinated Al sites. NMR of ^{27}Al indicates tetrahedral coordination for all Al, and 3) low Al/Si ratio leads to no significant contribution of Al-O-Al and Al-O-B groups as observed in aluminoborates.[51]

Experimental work on low resolution (low field) ^{27}Al MAS NMR suggested that 4-coordinated Al was predominantly present in Na-bearing systems.[70] Du et al. showed that the inclusion of Ca in aluminoborosilicate glass promoted 4-coordinated Al and 4-coordinated B formation with preference to Al sites.[54] The Ca induces formation of 5- and 6-coordinated Al sites due to its higher field strength modifier cation. However, in the vendor glass, the amount of Ca in mol% is small compared to these studies. Thus, we expect the effects of higher coordinated-Al sites to be minimal in vendor glass. Furthermore, Ba (0.26) has lower cation field strength compared to Ca (0.36). As a result, the effect of Ba-containing glasses on 5-coordinated Al and 6-coordinated Al formation would be minimal compared to Ca. In alkali silicate glasses, Zn can be found in 4- and 6-coordinated Zn, with preference to 4-coordinated Zn. In these glasses, the ratio 4-coordinated Zn/6-coordinated Zn is inversely proportional to Zn/Na ratio. Inclusion of Zn (<16 wt% of ZnO) in borosilicate glasses is known to increase mechanical property and enhance chemical durability.[71,72] This improvement in mechanical properties and chemical durability in presence of Zn contents in borosilicate glasses can be explained by network-forming property of Zn, thus the polymerization of glass structure. The presence of Zn decreases the concentration of modifiers, as some of the low field strength cations (e.g., Na) are utilized to charge compensate the ZnO_4 tetrahedra.

Stoichiometric calculation of NBOs is complicated in complex aluminoborosilicate glasses. In alkali/alkaline B containing glasses, uncertainties in conversion of $^{[3]}B$ to $^{[4]}B$ and more complex behavior in NBO formation with role of modifier oxide promote three- to 4-coordination for B: $BO_{3/2} + SiO_{3/2}O^- \leftrightarrow [BO_{4/2}]^- + SiO_{4/2}$. In B-rich glasses, low modifier oxide content, a forward reaction is expected. In this work, we use modified Dell and Bray model proposed by Du and Stebbins to predict N_4 and NBO based solely on the composition of alkali-alkaline aluminoborosilicate glass. The modified Dell and Bray model assumes that the mixing behavior for 4-coordinated Al and 4-coordinated B and the variation of N_4. Therefore, it is reasonable to group Al and B as one type of cation. For example, $20Na_2O.8Al_2O_3.7B_2O_3.65SiO_2$ is equivalent of $20Na_2O.15M_2O_3.65SiO_2$. The values for R ($[Na_2O]/([Al_2O_3]+[B_2O_3])$) and K ($[SiO_2]/[Al_2O_3]+[B_2O_3]$) become 20/15, and 65/15, respectively. The expressions $R_{max} = 0{\cdot}5 + K/16$ and $R_{D1} = 0{\cdot}5 + K/4$. When R is above R_{max}, further addition of Na_2O results in the formation of Si-NBO. B-NBO begins to appear when $R > R_{D1}$. The conditions for NBO and N_4 prediction are:

$$NBO = 2(R - R_{max})/(R + 2K + 3))$$

$$N_4 = \begin{cases} R, & R \leq R_{max} \\ 0.5 + K/16, & R_{max} < R \leq R_{D1} \\ R_{max} - (R - R_{D1})(8 + K)/[12(2 + K)], & R > R_{D1} \end{cases}$$

The general assumptions to predict the NBO and N_4 content for the glasses in Table 4-IV are: 1) all Al in glass are 4-coordinated and 2) negligible oxygen triclusters. The negative number in the NBO column can be assumed to be of zero value. This exercise is to understand NBO distribution in the glasses studied in this work. For the vendor glass, we predict the NBO content in terms of Na content in the glass as our work with ICP-AES on the vendor glass revealed that concentration in mol% of CaO < 0·02, BaO < 1, and ZnO < 0·03. The modified Dell and Bray model predicts absence of NBO in all the glass composition. This is supported by our XPS results as the high-resolution peaks for Si, B and O show no distinction in various energies for BOs and NBOs. These results show that the glass studied were highly polymerized, which would results in high mechanical properties and chemical durability.

Table 4-IV. Prediction of NBO and N_4

Glass	SiO_2	Al_2O_3	B_2O_3	Na_2O	R_{max}	R_{D1}	R	NBO	N_4
Alfred	68	5.5	13	13.5	0.73	1.42	0.73	0	0.73
Vendor1	75	2	14	9	0.79	1.67	0.56	-0.035	0.56
Vendor2	75	4	15	6	0.74	1.48	0.32	-0.076	0.32
Vendor3	75	3	17	5	0.73	1.44	0.25	-0.090	0.25

5. Conclusion

The mechanical and chemical durability of commercial PMT and simplified Alfred glasses were studied using Vickers indentation, R-O-R biaxial flexural strength test, elemental ions release, XPS and WDS. The glasses were tested using static mode leaching experiment and water simulation test. The Vickers hardness and R-O-R biaxial flexural strength test of two commercial PMT glasses shows that the two glasses had similar mechanical properties. The static mode leaching experiment shows that the glass surfaces formed dealkalized and deboronated layer. In addition, the normalized mass loss indicates pH and temperature dependent ion-release behavior of the Vendor1 glass. The water simulation test on bulk glasses shows no visible surface alterations, further confirmation would require spectroscopic analysis. WDS results showed dealkalized and deboronated layer which agrees with the static mode leaching experiment. The effects of high-purity water on the R-O-R flexural strength of the glass was relatively minor as the test measures the bulk strength of the glass.

CHAPTER 5. GADOLINIUM (Gd) – ION RELEASE STUDY

1. Gadolinium in WCD

The sensitivity of the water Cherenkov detector is pivotal to its success and can be enhanced through either building larger water tank that increases the probability of neutrino interaction in WCD, varying the size of PMTs which increases the sensitivity of the PMTs, or including additives, such as gadolinium (Gd), in water that essentially reduces background signals. Construction of larger WCDs would have financial implications, while increasing PMT size, beyond 50 cm diameter semi-spherical PMTs used in Super-K, would severely challenge the manufacturability and their mechanical integrity under WCD's hydrostatic environment. Therefore, additive in water is more financially sound and less risky option to enhance detector sensitivity.

It is known that inclusion of Gd in the WCDs enhances its sensitivity.[73] In an inverse beta decay, an electron antineutrino scattering from a proton creates a positron and neutron. The positron undergoes a prompt matter-antimatter annihilation emitting light of energy calculated as $E_{vis} = E_{\bar{\nu}_e} - 782\ keV$[74] and the neutron capture on hydrogen nucleus release a 2.2 MeV gamma (not detectable in Super-Kamiokande detector). However, the neutron capture by Gd results in 8 MeV gamma with temporal (~30 μs) and spatial (< 200 cm) coincidence with the positron from the initial interaction. A schematic representation of the role of Gd is shown in Figure 5-1. This delayed neutron capture by Gd and higher gamma emission energy compared to neutron capture by hydrogen nucleus, creates a unique signature and improves background reduction to an antineutrino event which allows antineutrino detection in WCDs.

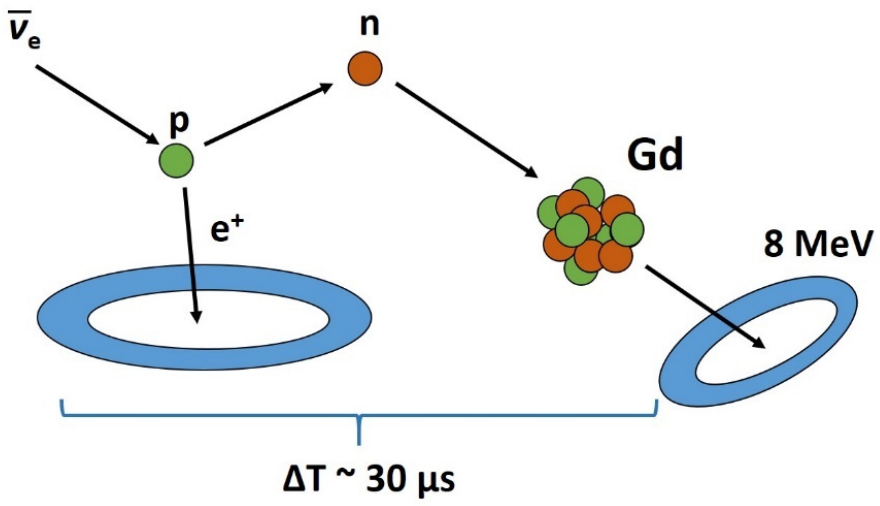

Figure 5-1. An inverse beta decay event followed by neutron capture in Gd nucleus [Image recreated from website: < http://www-sk.icrr.u-tokyo.ac.jp/sk/physics/srn-e.html>].[75]

The inclusion of Gd-based salt compounds in WCDs has been proposed by Beacom and Vagins.[73] In particular, addition of $Gd(SO_4)_3$[76–78] and $GdCl_3$[73,78–81] in the water has been studied. The proposed Accelerator Neutrino Neutron Interaction Experiment (ANNIE)[82,83] and Evaluate the Gadolinium's Action on Detector Systems (EGADS)[76,77,84,85] programs have also used Gd-doped water system. Additionally, Gd inclusion is proposed to improve detection of supernovae ν_e,[86] and detection of low energy neutrino.[87] Beacom and Vagins have shown that inclusion of $GdCl_3$ salt, the least expensive and most readily available Gd compound, in water boosts gamma energy capture. A small amount of $GdCl_3$ (0.2% in weight) has been found to result in ~90% of the neutron being captured on Gd. The neutron capture cross section of Gd is in the energy range of 3 to 225 keV. Additionally, Gd can also be retained in water through special water filtration technologies.[76]

The capture of neutron on Gd would reject majority of the atmospheric neutrino background and substantially enhance the Super-Kamikande detector sensitivity for diffuse supernova neutrino background (DSNB) events. The authors have estimated background reduction by a factor of ~5 with the addition of $GdCl_3$ for cosmic rays, notably muon-

induced spallation and muon-decay electrons. The addition of $GdCl_3$ might sufficiently reduce backgrounds such that the DSNB would become visible at energies between about 10 and 20 MeV. However, a major issue with these additives, especially with $GdCl_3$, is the Cl-based byproducts, which can reduce the transparency of water in the UV region reducing the detector sensitivity. In addition, it might induce corrosion, which would compromise mechanical strength of the detector components, particularly during the long service of detector programs. The corrosion products might absorb UV further reducing detector sensitivity. For example, Coleman[79] has shown that small amount of $GdCl_3$ addition results in formation of $FeCl_3$ compounds as a result of exposure to stainless steel enclosure. Furthermore, iron (Fe^{3+}) ions is a strong absorber of UV.

An alternative method to introduce Gd in the water is to utilize the natural corrosion phenomena of water on glass surface. In contact with water, glass corrosion results in elemental ion release.[88,89] Although the true glass surface alteration mechanism is in debate,[90–92] the elemental ion release is well reported in the literature. In this chapter, we report on the Gd-ion release from a Gd-doped glass composition like the one currently used in some of the detectors. The main idea is to show that Gd-ions can be released from the glass surface when in contact with water. We are not proposing use of the PMT themselves as source of release. A controlled ion release from glasses in the form of beads or powders can be achieved through further composition and production design of the glass. Controlled release glasses have been reported for biological[93] and neurological applications[94] and drug delivery.[95–97] We have studied the Gd-release from Gd-doped peralkaline ([Na]/[Al]>1, ratio of sodium and aluminum oxide concentration) borosilicate glass using chemical durability test method in high-purity water at 14 °C, corresponding to WCD's operational temperature. In addition, we also report the solubility of Gd in a base Alfred glass.

2. Materials and Methods

2.1 Glass Preparation

Gd-doped peralkaline borosilicate glasses were synthesized using reagent-grade SiO_2, Al_2O_3, H_3BO_3, Na_2CO_3, and Gd_2O_3. The Gd_2O_3 concentration was systemically

varied (in mol% = 2, 3, 4, 5, 6, and 8) in the base Alfred glass composition (in mol%): SiO_2=68.1, Al_2O_3=5.6, B_2O_3=12.9, and Na_2O=13.4. The Gd-dopant concentrations were selected to incorporate and test the highest possible amount of Gd into the glass matrix. This will be discussed in detail in Section 3. The Alfred glass was designed to closely represent PMT glass composition used by vendors. 10 g batch size powders were thoroughly mixed in a Pt-Rd crucible, which was placed in an electrically furnace at 1450 °C for 1 h and 0.5 h at 1550 °C. Following the melting schedule, the melt was ice-quenched to form glass by dipping the crucible and ensuring only outside of the crucible in contact with the ice water. The ice-quenching method ensures higher cooling rate, which promotes glass formation. The resulting glass was annealed at 550 °C for an hour and cooled to room temperature at 5 °C/min.

2.2 Gd-ion Release Study

Static mode chemical durability study according to PCT-B[67] procedure was used to determine Gd-ion release. Reagent water of specification as described by ASTM Type-I water (resistivity (MΩ-cm) at 25 °C > 18, organic carbon < 50 ppb, sodium < 1 ppb, chloride < 1ppb, silica < 3 ppb) was used for this work and precooled at 14 °C (WCD optimal operational temperature) before bringing in contact with powdered glass samples in high-density polyethylene (HDPE) reactors. Glasses produced from melt-quench technique described in Section 2.1 were crushed using mortar and pestle. 75-150 µm size of crushed glasses were retrieved through sieving. The crushed samples were ultrasonically cleaned with water and ethanol for 5 mins each and rinsed with water twice. The samples were then dried overnight at 90±1 °C and stored in a desiccator. Specific surface area of the crushed samples was measured by nitrogen adsorption Brunauer-Emmett-Teller (BET) analysis was 0.0403 ± 0.0012 m^2g^{-1}. 10.07 mL volume of high-purity water was used for all tests. A surface area to volume ratio (S/V) = 4000 m^{-1} was maintained for all test periods. One gram of glass powder was placed in separate HDPE reactors followed by precooled ASTM Type-1 water. The reactors were closed firmly wrapped with parafilm around the reactor cap. The reactors were submersed partially into the water bath system as illustrated in Figure 5-2 and the temperature was monitored at 14 °C. The PMT glasses used in WCD application are in bulb format however crushed

samples were used to investigate the chemical durability of glasses. The crushed samples provide a larger surface area for exposure to the reacting agent, in this case water. The time periods for the test were varied for 1, 5, 14, and 40 days to determine Gd-ions release. Three test samples were prepared for each test day. After completion of each test period, the solution was filtered with 0.2 μm Millipore filters and collected for pH measurements and elemental analysis using ICP-OES.

The selected test periods are short compared to the operational lifetime of a WCDs ~10-20 years. However, the goal of the work is to report a possible alternative method of Gd-inclusion in the WCD water systems rather than a comprehensive study of the effects of water on the PMT glasses over an extended period. Additionally, vapor hydration testing (VHT) can be used to expedite measurement to simulate the long-term operation in water.

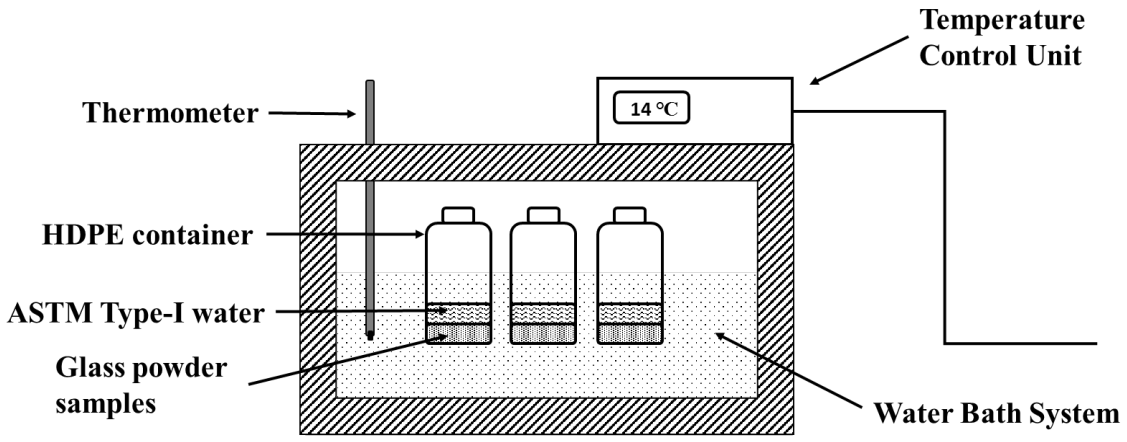

Figure 5-2. Schematic of chemical durability test setup.

3. Results and Discussion

X-ray diffraction (XRD) of powdered glasses confirmed absence of crystallization in all formulated glasses. However, significant amount of phase separation was observed for higher (6 and 8 mol%) Gd-dopant concentration through visual confirmation. Li et al.[98] showed that the Gd-solubility strongly depended on the glass composition, specially by the concentration of each glass former, B, Si, and Al. Additionally, as Gd was added into the

peralkaline borosilicate melt, double chain structure like that of gadolinium metaborate was formed at B to Gd ratio about 3:1. Since B < Gd, no crystallization was observed as it was shown that Gd in silicate would eventually lead to crystallization. The phase separation was possibly due to double chain structure in the peralkaline borosilicate glass. Phase separated glasses were not used for further investigation. A maximum of 5 mol% of Gd_2O_3 addition to the base glass was achieved in a uniform glass with no phase separation which was confirmed by XRD plot.

Density values, measured using He-pycnometer, for concentration of Gd_2O_3 (in mol%): 2, 3, 4, and 5 are 2.60 (2.53), 2.71 (2.62), 2.77 (2.71), and 2.89 (2.80) gcm^{-3}, respectively. The values in parentheses represent SciGlass® calculated densities using Priven 2000 method.[99] The systematic density increase has a linear correlation to concentration of Gd added to the base glass. The measured and calculated values are in very good agreement. We have succeeded in adding up to 5 mol% Gd_2O_3 in base Alfred glass without any crystallization or phase separation for the specific melting procedure. We have used this glass for Gd-release corrosion study.

The pH was measured on an aliquot of the retrieved filtered solution. pH for ATSM Type-I water, 1, 5, 14, and 40 test days are 6.32 (0.02), 6.37 (0.03), 6.51 (0.03), 6.65 (0.05) and 6.72 (0.05), respectively. The bracket in values are statistical errors associated with the triplet corrosion study. Figure 5-3 shows plot of pH as a function of test periods. The pH value levels out for longer time periods. pH increase is an expected behavior due to the corrosion effects of water on glass. These effects are a result of release of modifier (e.g., Na^+) ions from the glass surfaces. In this study, pH increases from 1 to 14 test days at a higher rate that from 14 to 40 test days. The pH remains statistically unchanged for 14 and 40 test days. The overall change in pH for the test periods is ~0.4 pH. The increase in pH is associated with elemental release (in ppm) of Na and Si, which are higher in concentration in the glass than the rest of the glass constituents, as shown in Figure 5-4.

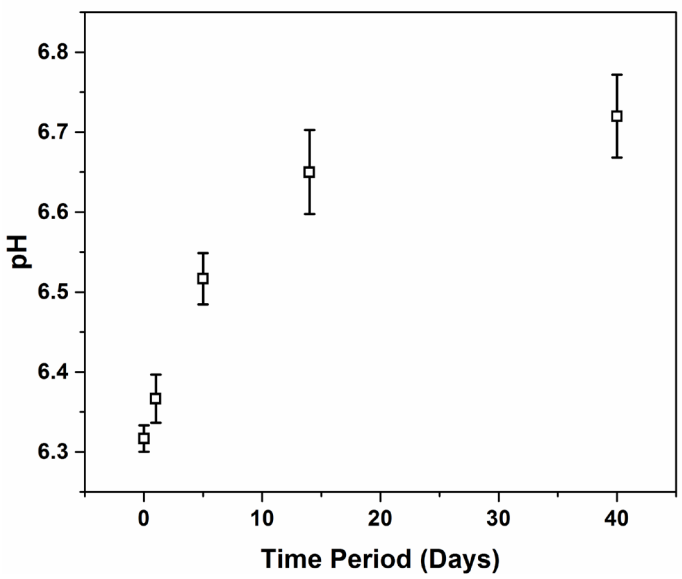

Figure 5-3. pH measurement for PCT-B test

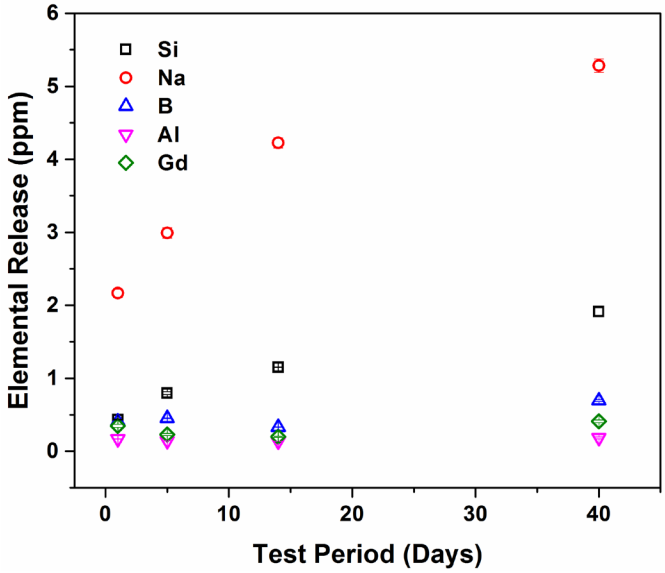

Figure 5-4. Elemental ion release for the Gd-doped peralkaline borosilicate glass

In Figure 5-4, the statistical errors generated using measurements from 3 separate triplet test samples are included in plot but are too small to perceive. Na ion release is the highest among all elements as it has a high mobility due to weaker ionic bonding environment. The surface ion exchange reaction involving network modifiers such as Na

and protons produces silanol (Si-OH) groups which can be described as a leaching process and expressed as:

$$\equiv Si - O - Na^+ + H_2O \rightarrow \equiv Si - OH + Na^+ + OH^- \quad (5.1)$$

Numerous models have been used to describe the glass corrosion mechanism. The chemical affinity model is based on the degree of silica saturation[100,101] and rate law developed by Aagaard-Helgeson.[102] The model neglects the importance of the corrosion layer until a secondary phase precipitates, which affect the long-term solution saturation state. The alkali-proton exchange model is based on the formation of corrosion layer as a product of the rate-limiting ion exchange reactions between protons and network modifiers such as Na.[103–105] The resulting silanol (Si-OH) groups are believed to polymerize in the solid-state, forming a hydrated glass layer. A variant of third model is GRAAL (Glass Reactivity with Allowance for the Alteration Layer),[106] assumes that the corrosion layer constitutes a protective 'gel' layer.[107–109] In this model, the release of elements to solution (the corrosion rate) is governed by the transport properties of the "leach layer". A "Passivating Reactive Interface" (PRI), characterized as dense and constricted pores, becomes relatively impermeable with time and forms, as the alkali-proton exchange proceeds, a dynamically restructured, residual, hydrated glass. Furthermore, a new model on silica based glasses has proposed the spatial and temporal coupling of glass dissolution and silica precipitation and growth, and explains the formation of glass corrosion layer by congruent glass dissolution that is coupled in space and time to the precipitation/deposition of amorphous silica at a moving reaction interface, forming a corrosion layer that is composed of spherical silica aggregates of variable size and porosity.[91]

The Gd-ion release for 1, 5, 14, and 40 test days are 0.34 (0.02), 0.23 (0.02), 0.2 (0.01), and 0.41 (0.02) ppm, respectively. The elemental release for Gd-ions shows a slight decrease for 5 and 14 days. This behavior is congruent to the small decrease in elemental ion release for B and Al. Typically, Gd acts as a network modifier, which depolymerizes the glass structure by interrupting bonds between glass forming units such as tetrahedral Si, B, and 4-coordinated Al. The stability of cations in the glass structures may be determined by the strength of the electrostatic bond in terms of z/CN (where z is the charge

and CN is the coordination number of the cations with its nearest oxygen).[110,111] In addition, Gd cations favorably compete with Na cations for the B-rich environment.[112] As discussed above, the Gd- and B-rich environment resemble the Gd-metaborate structure, $1BO_4{:}1Gd_2O_3{:}2BO_3$.[113–116] Furthermore, Brow and Tallant[116,117] have showed that the tetrahedral Al substitutes tetrahedral B site in presence of lanthanides (Ln) for Ln_2O_3-Al_2O_3-B_2O_3 glasses. The presence of this structure could possibly explain the linear relationship between Gd and Al elemental release, shown in Figure 5-5, in Gd-doped glass system. However, a comprehensive detailed structural and morphological analysis is required to validate such claim, which is beyond the scope of this work.

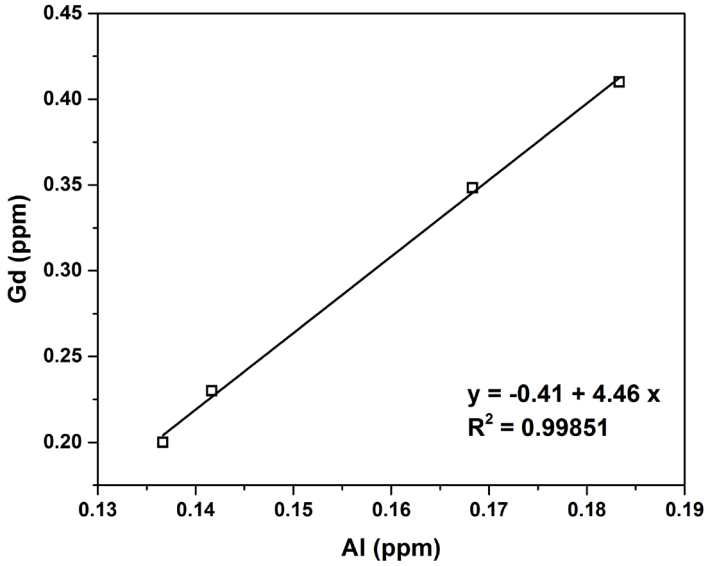

Figure 5-5. Correlation between Al and Gd elemental release.

4. Conclusion

In this chapter, we have studied the incorporation of Gd-ions in the peralkaline borosilicate glasses, representative of PMT glass systems for application in neutrino detection. We have shown a maximum of 5 mol% of Gd_2O_3 was doped in the matrix of base peralkaline borosilicate glass through melt-quench technique without phase separation. The ion release study clearly indicates the Gd-ion release from the glass powder at 14 °C. Our results demonstrate that Gd-doped glass compositions can be designed in the form of beads or powders for controlled Gd-release when in contact with water, which may be added to pure water to enhance neutrino detector in the future.

CHAPTER 6. MD SIMULATION USING THE REACTIVE FORCE FIELD (REAXFF)

1. Glass Surface-Water Reactions

Glass surface-water reactions are of interest in many applications of silicate glasses that range from display technology[118] and nuclear waste glass[88,119,120] to photomultiplier tube application[121–123] in neutrino detectors[9,35,37] among others. The macroscopic aspects of glass-water interactions have been investigated using various experimental techniques, such as Fourier transform infrared (FTIR) spectroscopy, X-ray photoelectron spectroscopy (XPS),[124] inductively coupled plasma atomic emission spectrometry (ICP-AES)[121,122] and secondary ion mass spectrometry (SIMS). These experiments were designed to study the long-term effects of water on glasses and have explained the outcome using various models.[101,103,104,106] In addition, computational techniques have been used to understand the glass surface-water reactions at an atomic level.

Computational techniques such as quantum mechanical (QM) *ab initio*[125–127] and classical molecular dynamics (MD)[64,128–133] simulation methods have been used to study glass structures and glass-water reactions. QM *ab initio* methods can achieve high degree of numerical accuracy and simulation chemical reactions by calculating electronic contributions of a system and is therefore, computationally expensive, limited to sub-nanometer length and picoseconds time scales, and unable to simultaneously simulate bulk and interface properties. Meanwhile, classical MD techniques are desirable due to the low computation cost, ability to simulate larger systems and longer time scales; however, it cannot simulate chemical reactions, the dissociation and formation of bonds, unless appropriate potentials are applied. Some of these potentials have been developed to study the structure and energy of SiO_2-H_2O interactions and the water adsorption onto vitreous silica by using non-dissociative[134,135] and dissociative potential,[128,132] respectively. In addition, the physisorption of water on silica and silicate glass fracture surfaces has been studied by Leed and Pantano[130] and the chemisorption of water has been studied by Du and Cormack[131] by developing hydroxyl groups and hydroxyl group-glass interaction models. Although these methods have been vastly successful in providing insights to the glass surface structures, surface defects and glass surface-water reactions, reactive MD

potentials, such as reactive force field (ReaxFF), offer an alternative method to simulate structures and chemical reactions within a MD framework.

ReaxFF potential, a MD force field developed by van Duin et al.,[65] is an empirical force field based on bond order concept that allows chemical reactions to occur within a MD framework. The central idea is that the bond order (strength of the bond) depends upon the local environment.[136] The bond order theory is the foundation for potentials such as the Tersoff potential,[137] REBO[138] (reactive empirical bond order), BOP[139] (bond-order potential) and AIREBO[140] (adaptive intermolecular REBO). The ReaxFF potential, initially developed for hydrocarbon system,[65] has been extended to study various systems such as zinc oxide[141] and hydration of ZnO,[142] Al-water reactions[143] and dynamics of reactive water in smectite clay-zeolite composites[144] among others. Furthermore, ReaxFF potential has been used to study the structure and properties of silica,[145,146] sodium silicates,[147] organosilicate glasses,[148] and silica-water interface.[127,149]

In this chapter, we extend the application of ReaxFF potential to simulate a ternary sodium aluminosilicate glass structures and the glass surface-water reactions. The parameters used for this work were developed by Pitman et al.,[144] who studied the dynamics of confined reactive water in smectite clay-zeolite composites. These parameters were selected as the primary constituents are the same, namely Si, Al, Na and water. We compared the bulk and surface structures generated by using ReaxFF and classical MD potentials, and showed the diffusion of water molecules and formation of hydrolyzed surface structural sites in the glass surface-water reaction model.

2. Simulation Details

2.1 Simulation Techniques

The composition of the simulated sodium aluminosilicate glass was (mol%): SiO_2=75, Al_2O_3=10, and Na_2O=15. The bulk and surface structures of sodium aluminosilicate glass were first built using GROMACS[150] with Buckingham potential, which was previously used to study calcium aluminosilicate glass systems.[151] The algorithmic and processor-specific optimization techniques applied in GROMACS can help to achieve a faster energy convergence.[152,153] The glass surface-water reactions were

simulated in LAMMPS[154] due to the versatility of the simulation package and the ability to implement ReaxFF potential. The details of the Buckingham and ReaxFF potentials are discussed in Chapter 3, Sections 3.1.2 and 3.1.3, respectively. The water models were generated consistent with TIP3P[155,156] potential, using a solvation procedure in visual molecular dynamics (VMD) software.[157] Before simulating the reactions on the glass surfaces, the water models were allowed to relax. The Coulombic interactions for both simulations were calculated by Ewald summation method with a cutoff of 10 Å. Typical cutoff (R_{cutoff}) lengths for Coulombic interactions are between 8-12 Å. For large systems, $N > 10^4$, a $R_{cutoff} < L/2$ is used, where L is the dimension of the simulation cell.

The bulk glass and surface were simulated in a constant-pressure-and-temperature (NPT) ensemble with a modified velocity rescaling[158] to control temperature fluctuations. This thermostat is a modified form of standard velocity rescaling with stochastic terms and smoother formulation which resembles Berendesen thermostat. In our study, the glass surface-water reactions simulation was performed using the Nosé-Hoover thermostat and a constant-volume-and-temperature (NVT) ensemble. The NVT ensemble was preferred over NPT to avoid unrealistic pressure effects due to difference in compressibility of glass and water.

2.2 Bulk Glass

Buckingham potential was used to generate the bulk glass structures from an initial random array of 5994 atoms in a cubic simulation box of length 55.46 Å, using a "melt-quench" technique. The time step (Δt) of 1 fs was used. The atoms were held at elevated temperature of 3000 K for 600 ps to erase all memory of the initial atomic configuration. Following the melt, the structures were subjected to a series of discrete temperature equilibration step schedule. The structures were equilibrated for 400 ps at every 20 K decrease in temperature until it reached 300 K, representing a nominal quenching rate of 0.05 K/ps. The final simulation cell dimensions were 43.94 Å × 43.94 Å × 43.94 Å.

2.3 Surface Creation

The glass surface structures were created using the vacuum gap method implemented in previous works by Du[159] and Garofalini.[160,161] Figure 6-1 illustrates the

schematic of the creation of glass surface. The initial bulk glass structure, Figure 6-1 (I), was duplicated in z-direction, Figure 6-1 (II). The vacuum gap method utilizes immobilization of bottom portion of the simulation cell to represent the bulk structure and allows the adjacent (upper) portion to essentially become free structure shown in Figure 6-1 (III). The atoms in the bottom half were 'frozen' to represent bulk structure, which were allowed to exert force on each other; however, their movements were inhibited. A vacuum gap of 40 Å in length, which exceeded the short-range potential cutoff, was inserted on top of the free structure as shown in Figure 6-1 (IV). The resulting simulation cell of dimension 43.94 Å × 43.94 Å × 127.84 Å was equilibrated using a step-wise thermal quench method at 100 K, 300 K, 600 K, and 900 K for 50 ps and 1200 K for 200 ps. These steps were necessary to prevent surface atoms from ejecting. The resulting atomic configurations were made compatible for LAMMPS program. The glass surface structures were equilibrated at 300 K for 300 ps with ReaxFF potential using a time step (Δt) of 0.25 fs before simulating the glass surface-water reactions.

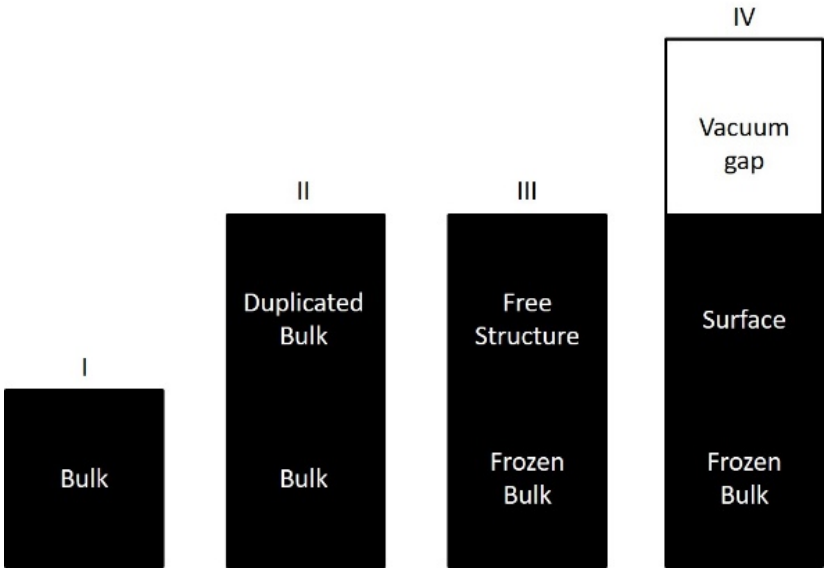

Figure 6-1. Schematic of the surface creation process: I – bulk structure, II – duplicated bulk structure in z-direction, III – distinction between 'frozen' structure and free structure and IV – vacuum gap added in z-direction.

2.4 Glass-Water System

1853 water molecules were inserted into the vacuum gap shown in Figure 6-1 (IV). A small gap was placed in the initial frame between the glass surface atoms and water molecules to minimize the electrostatic effects, Figure 6-2 (a). The initial gap was determined through trial and error method. In Figure 6-2, the water molecules (upper portion) are represented by a frame model with oxygen (red) atom connecting two hydrogen (white) atoms. The glass surface (lower portion) is represented by Si (yellow) and Al (green) tetrahedral units, and Na (blue) spheres. The oxygen in the glasses are assumed to be at the ends of tetrahedral units. The dimensions of the glass-water system were 43.926 Å × 43.926 Å × 120.00 Å. No distinctions were made between the O atoms in glass and water. The glass surface-water reaction simulation was performed at 300 K for 1625 ps with time step (Δt) of 0.25 fs. Figure 6-2 (b) shows final simulation step for the glass surface-water simulation model.

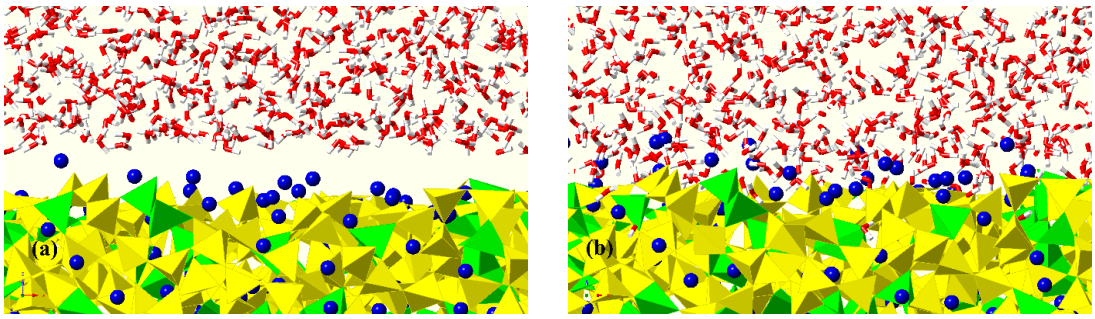

Figure 6-2. Snapshot of the (a) initial and (b) final frames of the glass surface-water reaction simulation. Color scheme: yellow tetrahedral = Si-tetrahedral unit, green tetrahedral = Al-tetrahedral unit, blue sphere = Na atom, white = hydrogen end of water, red = oxygen end of water. [Image generated with CrystalMaker].

3. Results and Discussion

3.1 Bulk and Surface Structural Properties

The bulk and surface structural properties were investigated in terms of bond length, bond angle, coordination number (CN), and Q_n-species distributions. These distributions were calculated as an average over the final 300 frames (300 ps – each frame was 1 ps apart) of the simulation. Table 6-I lists the cation-oxygen (M-O, where M = Si,

Al and Na), O-O and Si-Si bond distances for the bulk and surface structures (second and third column) generated with Buckingham potential and surface structures generated using ReaxFF potential. Additionally, The bond lengths reported by van Duin,[145] other MD simulation and experimental works are included.

The bond lengths calculated in this work are in good agreement with previous reported values. The Si-O and O-O bond distances for ReaxFF potential are much closer to other simulated and experimental values. A point to note is that the parameters for the classical Buckingham potential have been specifically parameterized to represent oxide systems; however, Reaxff potential was parameterized to represent aluminosilicate clay-zeolite structures. A good agreement between our data and previous studies is promising for the application of ReaxFF potential to study the glass structures and glass surface-water reactions.

Table 6-I. Bond Length Information for Bulk and Surface Simulation Compared to Previous Work

Species	Current Work			Previous Work		
	Bulk	Surface	ReaxFF	van Duin[145]	MD	Experimental
Si-O	1.605	1.615	1.63	1.56	1.60,[133] 1.59-1.61[129]	1.608,[162] 1.62[163]
O-O	2.605	2.645	2.75	2.53	---	2.626,[162] 2.65[163]
Al-O	1.765	1.755	1.79	---	1.74-1.78,[133] 1.74-1.75[129]	1.77[164]
Si-Si	3.155	3.185	3.065	3.06	3.155[165]	3.077, 3.12[163]
Na-O	2.415	2.455	2.385	---	2.42-2.46,[133] 2.4-2.6[129]	2.61[166]

Figure 6-3 (a) shows the bond angle distribution for inter-glass network former tetrahedral units, Si-O-Si and Si-O-Al, to be 153.1º and 144.5º, respectively. This difference in bond angles is due to different charges of Si and Al. The bond angle calculated for Al-O-Al was 137.5º. The low count of Al-O-Al suggests a homogeneous distribution of Al-tetrahedral units in the silicate glass network. Figure 6-3 (b) shows intra-

tetrahedral angle for the glass forming tetrahedral units, where BO and NBO are bridging oxygen and non-bridging oxygen, respectively. The overall O-Si-O angle is 109º, which includes contribution from both BO and NBO. The presence of NBO increases the bond angle from 108.8º for BO-Si-BO to 110.7º for BO-Si-NBO. In contrast, the intra-tetrahedral angle distribution for Al-tetrahedral units remain unaffected (O-Al-O=108.7º and BO-Al-BO=108.7º), which suggests that NBOs are primarily associated with Si-tetrahedral units.

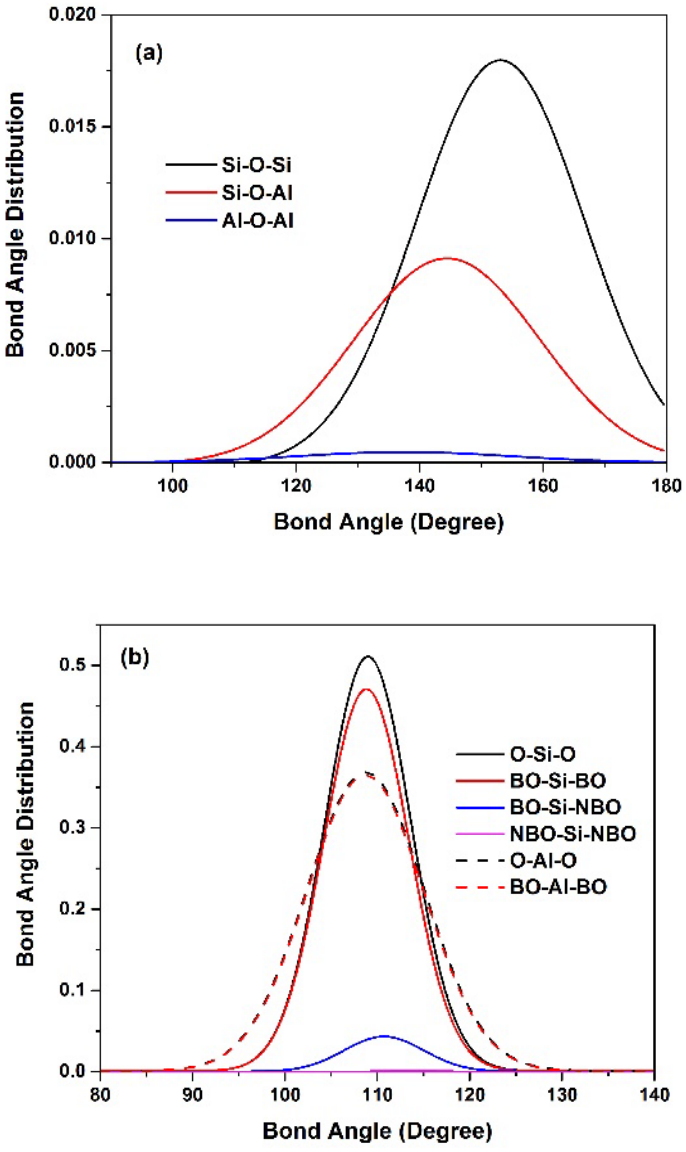

Figure 6-3. Bond angle distribution (a) between glass forming units (b) of central tetrahedral cations to oxygen atoms with distinction between bridging and non-bridging oxygen species.

The coordination number (CN) and Q_n-species distribution can provide further insights into the local environment of Si and Al atoms in the glass structure. Figure 6-4 (a) and (b) shows the CN and Q_n-species distribution for the bulk and surface glass structures, respectively. The CN was calculated within a predefined cutoff length of 2.1 Å for Si and 2.4 Å for Al, which were essentially the estimated first minimum of the radial distribution function (RDF), in this case for cation-oxide (Si-O and Al-O) RDF. Coordination number (CN) was calculated using:

$$CN = \int_0^{r_m} \varrho g(r) 4\pi r^2 \, dr \tag{6.1}$$

where r_m is the first minimum for RDF, $g(r)$ and ϱ is the probability density. In the bulk glass structure, all the Si atoms were 4-coordinated while lower coordinated Si atoms were observed in the surface structure. This trend was also observed for Al; however, 3- and 5-coordinated Al is already present in the bulk structure, albeit in small amounts.

The Q_n-species describes the nature of the glass forming tetrahedral unit in terms of the number of BO associated with it, for example, a tetrahedral unit with 4 BO is Q_4-species, 3 BO is Q_3-species, and so forth. The Si Q_4-species decreased from 84.39% for bulk to 81.67% for surface. The Q_4-species converts to Q_3- and Q_2-species as shown in Figure 6-4 (b). The amount of Al Q_4-species of 98.82% for bulk decreased to 96.08% for surface. Additionally, the bulk structure contained 93.44% of 2-coordinated O, 6.43% of 1-coordinated O and 0.13% of 3-coordinated O, and the surface structure consisted of 92.29% of 2-coordinated O, 7.44% of 1-coordinated O, and 0.23% of 3-coordinated O. The 3-bonded oxygens are considered as defects in the glass structure and are not necessarily due to formation of surface because they might already be present in the bulk glass. The under-coordinated Si and Al atoms are considered as structural defects as no such species have been detected by experimental methods and are therefore treated as structural defects generated by simulation techniques. The creation of surface increases the probability of formation of such defects and lower Q_n-species as it interrupts a continuous structural network. These defects are highly energetic and susceptible to chemical attacks from external agents such as water molecules.

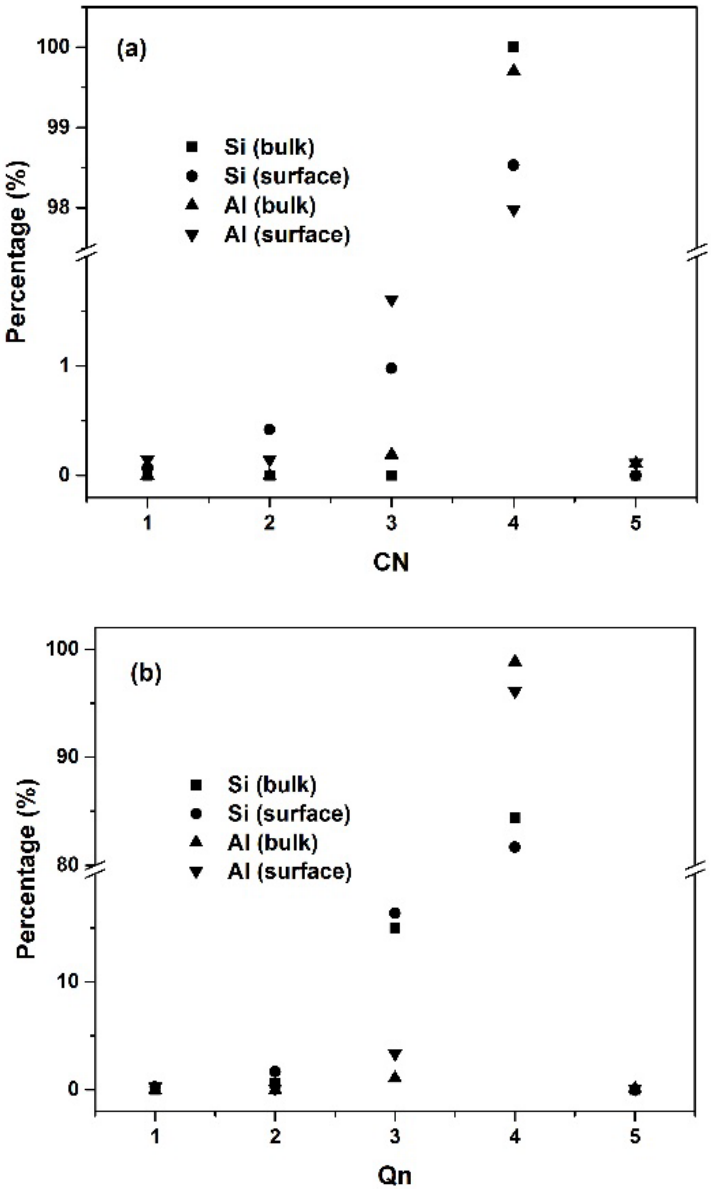

Figure 6-4. (a) Coordination number (CN) and (b) Q_n-species distributions.

The simulated glass surfaces were further investigated by calculating the atomic density profiles for Si, Al, Na and O atoms. The oxygen atom density profiles were identified as BO and NBO density profiles. Figure 6-5 shows comparison of atomic density profiles calculated for surface structures using Buckingham potential (solid lines with markers) and ReaxFF (dashed lines with open markers). The vertical dashed and dotted lines are an estimation of the surface boundary as defined by change in density for Buckingham potential and ReaxFF, respectively.

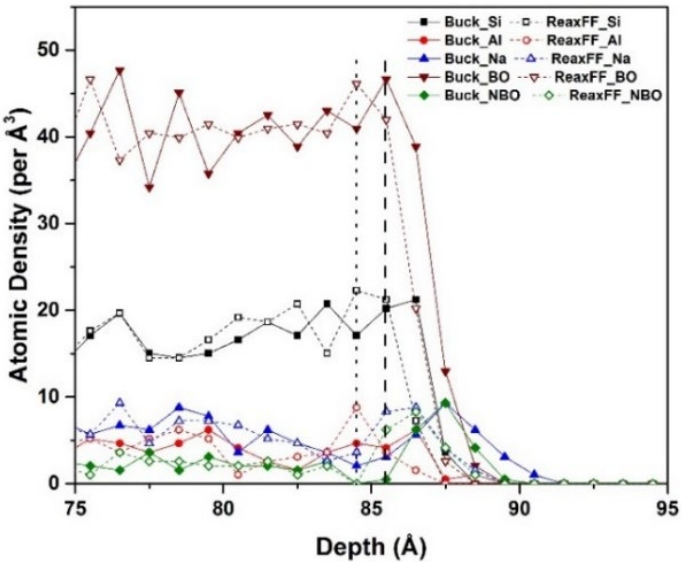

Figure 6-5. Atomic density profile (per Å) generated from Buckingham potential (solid lines and markers) and ReaxFF (dashed lines and open markers).

The atomic density profiles for surface structures generated using the two potentials were slightly different. On comparison of the atomic density profiles, the profiles calculated for the surface structure generated using ReaxFF potential contract a couple of angstroms than the ones generated using Buckingham potential. The contraction of the surface structure could be a manifestation of the effect of ReaxFF potential on the bond angle distributions as shown in Figure 6-6. The solid and dashed lines represent bond angle distributions generated by Buckingham potential and ReaxFF, respectively.

The bond angle distribution for inter-glass network former tetrahedral units calculated for surface structure using ReaxFF showed a smaller angle for Si-O-Si = 146.2º and Si-O-Al = 141.5º than compared to Buckingham potential, Si-O-Si = 153.1º and Si-O-Al = 144.5º. A smaller angular distribution between the glass forming tetrahedral units could bring them closer, resulting in a more compact structure. The surface structure generated using ReaxFF potential should be more realistic as ReaxFF can simulate better surface and interface properties. The ReaxFF application on silica surface has shown excellent agreement of structural, chemical and electrical properties to experimental and quantum chemical data.[149]

However, despite the difference in the atomic density profiles at the surface, the bulk atomic density profiles were similar. Most notably, the Si atomic density profiles below 80 Å were the same and the Na atomic density profiles extended the furthest with higher concentration at the surface, for both potential models. Similar behavior was observed for NBO density profiles, as the presence of Na atoms are typically accompanied by NBOs in a glass structure.

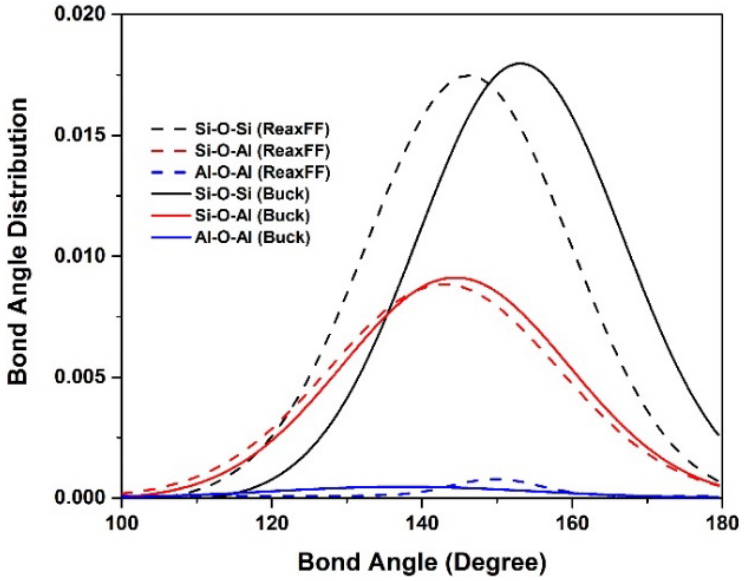

Figure 6-6. Bond angle comparison for Buckingham potential and ReaxFF.

3.2 Glass-Water Simulation

Figure 6-7 shows the atomic density profiles for (a) initial – 0 ps and (b) final – 1625 ps configurations of the glass surface-water reaction model. The estimated glass, interface and water regions are differentiated with vertical dashed lines based on the change in density. The interface region shows a significant change between the initial and final atomic density profiles. As the simulation proceeds, the water molecules approach glass surface which is indicated by H and O profiles. The hydrogen density profiles suggest that the water molecules diffuse into the glass surface. The nature of the hydrogen species, either associated with hydroxyl group (OH^-) or water molecule (H_2O) group was not distinguished, when calculating the hydrogen atomic density profile.

Additionally, in Figure 6-7, the Na atomic density profiles illustrate the 'leaching' of Na atoms from the glass surface. The leaching is described as the movement of mobile

atoms in the glass towards the glass surface in presence of a fluid media. This can be expressed by the following surface reaction:

$$\equiv Si - O - Na + H - O - H \rightarrow Si - O - H + Na^{+} + OH^{-} \qquad (6.2)$$

Na plays two different roles in an aluminosilicate glass: first as a network modifier by breaking up the glass network and second as a charge compensator for 4-coordinated Al-tetrahedral unit to maintain the charge neutrality.[167,168] The bond strength of Na associated with either NBO or 4-coordinated Al-tetrahedral unit depends on the ionicity of the interaction and is weaker compared to covalently bonded polymerized glass network.[168] Thus, the Na atoms at the surface are susceptible to diffusion when in contact with water molecules. Meanwhile, the Si and Al profiles suggest that the structural integrity at the glass surface remains intact throughout the simulation duration.

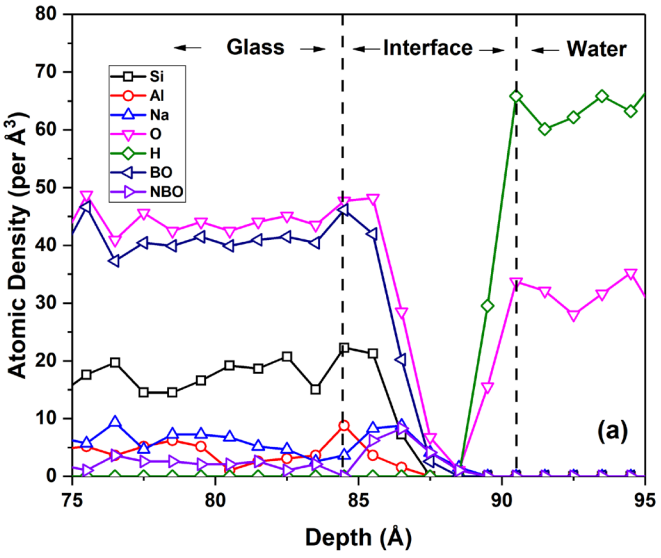

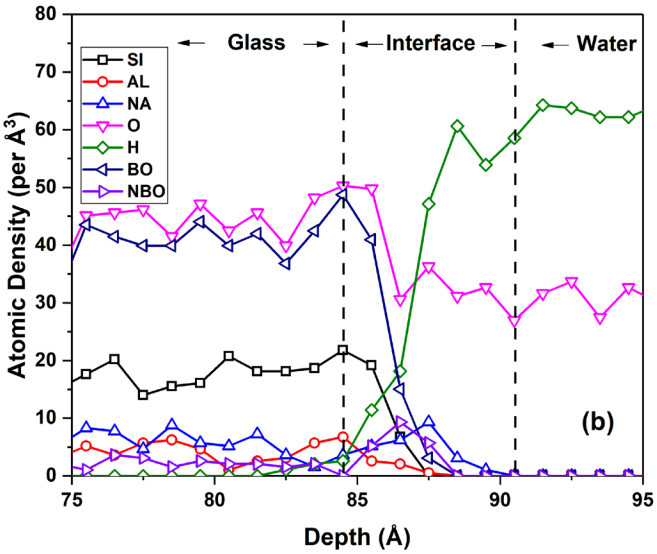

Figure 6-7. Atomic density profile at the (a) initial (0 ps) and (b) final (1625 ps) glass surface-water simulation frames.

Our results show that the H atoms at the glass surface exist in the form of hydrolyzed glass network and diffused water molecules. In Figures 6-8 and 6-9, the rest of the water molecules are hidden to highlight the hydrolyzation and diffusion processes, respectively. Figure 6-8 shows a series of snapshots of the hydrolyzation of NBO site to form a silanol (Si-OH) species. A water molecule approaches a NBO site shown in Figure 6-8 (a). Figure 6-8 (b) shows the transition of H atom, essentially breaking the O-H bond and separating from the OH^- group. Figure 6-8 (c) shows the formation of a new O-H bond, resulting in Si-OH and OH^- groups. The snapshots in Figure 6-8 were captured within 0.125 ps, which indicates that once the water molecule comes close to the NBO site, the hydrolyzation process is instantaneous. Additionally, beyond the timeframe shown in this scenario, the OH^- group, formed after the transfer of H^+, continues to be around the Si-OH. The H atom was observed to oscillation between the NBO site and OH^- group forming Si-OH and H_2O at different simulation timeframe.

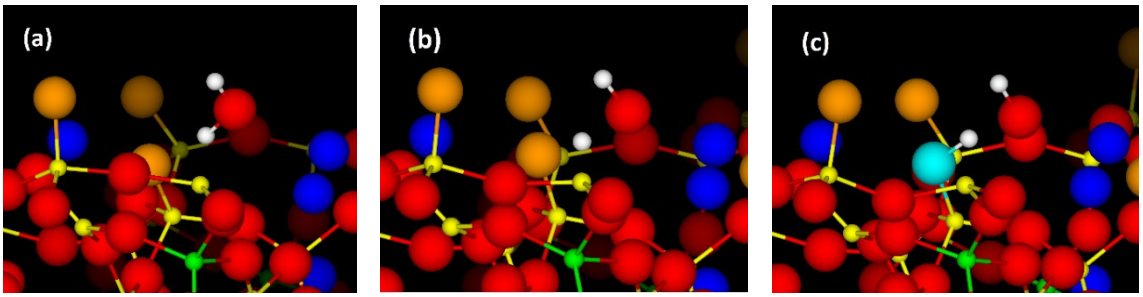

Figure 6-8. Snapshots illustrating the formation of Si-OH species at the glass surface. Color scheme: yellow = Si, green = Al, red = oxygen (both BO and oxygen associated with water molecule), blue = sodium, white = hydrogen, gold = NBO, and cyan = oxygen in Si-OH species. a) A water molecule near a NBO attached to Si at the surface. b) One of the hydrogen atom detaches from the water molecule and moved toward the NBO site. c) Formation of Si-OH species along with a OH^- [image generated with CrystalMaker].

Figure 6-9 shows the diffusion process of a single water molecule. In figure 6-9 (a), the water molecules are above the first atomic layer of the glass surface at 2.5 ps. Figures 6-9 (b), (c), and (d) show a rapid diffusion of the water molecule into the glass surface structure. This transition occurs within the initial 30 ps of the simulation. Figures 6-9 (e) and (f) show the water molecule at 750 ps and 1625 ps, respectively. Figure 6-9 illustrates a case where after the initial rapid diffusion of water molecule, the diffusion has slowed down. The initial rapid diffusion could be due to the relatively open surface structures of glass. As the water molecules approaches less-open glass structures, further diffusion is restricted. Additionally, Figures 6-9 (e) and (f) show the formation of multiple Si-OH species (cyan), which were previously NBO site (gold) associated with Si. Furthermore, Figure 6-9 shows a gradual outward diffusion of Na atoms from the glass surface.

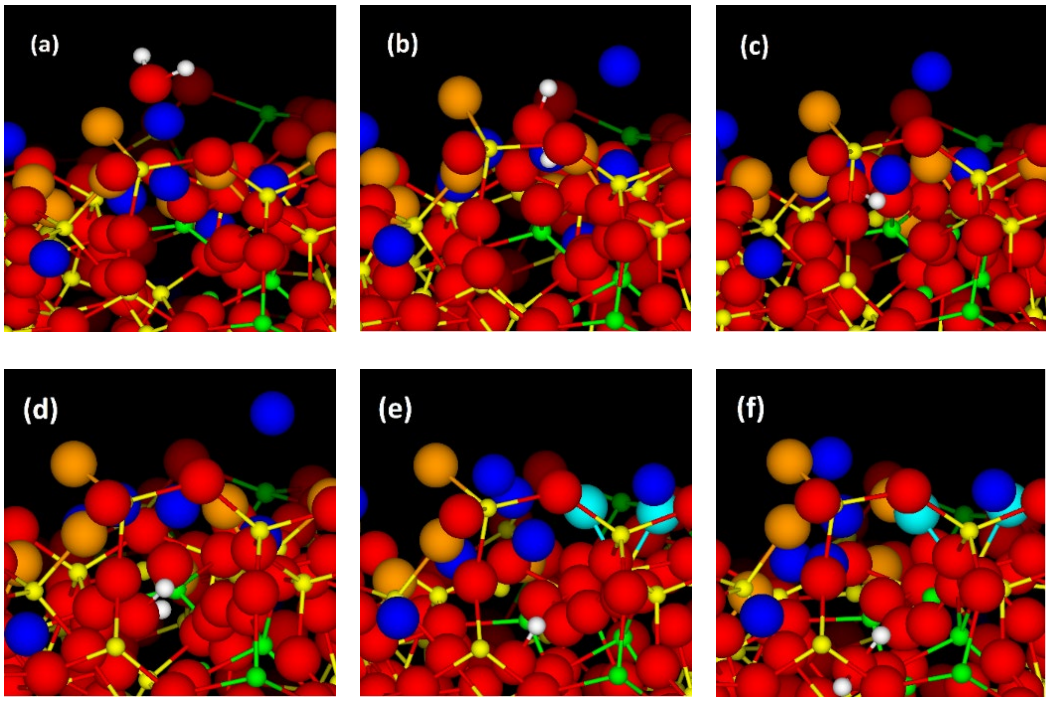

Figure 6-9. Snapshots illustrating the diffusion of a single water molecule into the glass surface. Color scheme: refer to Figure 6-8. The simulation time for the snapshots a) 2.5 ps, b) 13.75 ps, c) 15 ps, d) 30 ps, e) 750 ps and f) 1625 ps [image generated with CrystalMaker].

4. Conclusion

In this chapter, the glass surface-water reactions were simulated using ReaxFF potential. The bulk and surface structures were generated using a combination of Buckingham and ReaxFF potentials. The fundamental structural properties such as bond lengths and angles were in good agreement with previously reported values, in spite of our use of ReaxFF parameters, which were originally parameterized for clay-zeolite composite and water model. The surface structure generated using ReaxFF resulted in a compact glass structure compared to Buckingham potential. This difference is attributed to the bond angle distribution between glass forming tetrahedral units (Si-O-Si and Si-O-Al). The glass surface-water reaction simulation showed the formation of Si-OH at a NBO site and the diffusion of water molecules at the glass surface. Our work demonstrates that ReaxFF potential can be applied to study the glass structures and glass surface-water reactions.

CHAPTER 7. MD SIMULATION OF MULTICOMPONENT SODIUM ALUMINOBOROSILICATE GLASSES

1. Introduction

MD simulation provides atomistic level of information about the structure and properties of glasses. Numerous simulations have been performed on silicate, sodium silicate, aluminosilicate glasses. However, B-containing glasses have been less studied using MD simulations. Previous studies include *ab initio* molecular dynamics (AIMD) and MD simulations. AIMD method is ideal to study B-containing glasses because of its inclusion of electronic contribution; however, it is computationally very expensive and restricts the size- and time-scale of simulation. MD provides an alternative method to study glass structures and properties as it has the advantage of computational efficiency, and simulation of longer time-scale and large systems. MD simulation is an important tool to investigate the structures and properties of multicomponent B-containing glasses.

In this chapter, the composition-structure-property of aluminoborosilicate glasses are studied using MD simulations. The glass compositions were designed within the compositional space of the commercial PMT glasses. In addition, the Young's modulus (E) was calculated from uniaxial tensile simulation and insights into its compositional and structural relationship.

2. Simulation Details

2.1 Glass Composition

Table 7-I shows the sixty-nine different glass compositions studied in this work along with the number of atoms used to simulate each glass. The glass compositions were statistically designed within the compositional space of commercially available PMT glass composition. The aluminoborosilicate glasses used for PMT application have high SiO_2 content with minor concentration of CaO, BaO and ZnO. The statistical process ensures the designed compositions have good orthogonal and space filling properties. A good orthogonal property is desirable for uncorrelated estimation for the regression coefficients and good space-filling property has data points scattered throughout the domain in a

uniform-like manner. Figure 7-1 shows a scatter-matrix plot as a function of individual oxide component indicating the random distribution of oxide concentrations in the designed compositions.

Table 7-I. Aluminoborosilicate Glass Compositions (mol%) and the Number of Atoms used to Simulate Each Glass

Formulation	Composition (mol%)							Number of atoms
	SiO_2	B_2O_3	Al_2O_3	Na_2O	CaO	BaO	ZnO	
G1	72.58	15.90	2.85	7.15	0.15	0.64	0.73	50005
G2	71.81	15.57	3.36	8.40	0.21	0.51	0.13	50012
G3	70.60	15.91	2.92	9.17	0.62	0.14	0.64	50008
G4	71.14	15.46	2.76	7.23	0.01	1.01	2.39	50007
G5	72.17	14.84	4.21	8.67	0.04	0.04	0.04	50011
G6	70.33	15.93	4.16	8.58	0.26	0.20	0.55	50011
G7	71.00	14.28	4.42	7.61	0.26	1.03	1.40	50002
G8	71.81	15.64	2.92	7.26	0.86	0.44	1.07	50011
G9	70.91	14.20	4.44	6.86	0.68	0.54	2.37	50014
G10	68.85	16.67	2.69	9.12	1.12	0.11	1.43	50016
G11	72.08	15.90	3.15	8.11	0.21	0.44	0.11	50011
G12	70.61	15.10	3.12	8.53	0.83	0.15	1.66	50010
G13	70.22	16.27	3.77	6.96	0.54	1.02	1.22	50013
G14	70.23	14.52	4.37	7.61	0.69	0.31	2.28	50003
G15	73.56	15.05	3.29	6.98	0.10	0.77	0.25	50013
G16	70.93	15.60	3.78	6.91	0.46	0.35	1.97	50006
G17	70.38	14.62	4.13	8.50	0.53	1.21	0.63	50002
G18	73.73	15.11	2.98	6.92	0.41	0.38	0.47	50005
G19	72.81	15.33	3.58	7.04	0.02	1.12	0.10	50012
G20	71.12	16.98	2.72	6.48	1.04	0.96	0.70	50008
G21	70.26	16.95	3.24	6.91	0.05	0.61	1.98	50010
G22	71.81	15.26	3.75	6.67	0.42	0.46	1.63	50003
G23	68.31	16.71	4.01	7.90	0.66	0.42	1.99	50008
G24	68.89	15.49	3.52	7.97	0.68	1.16	2.29	50012
G25	73.23	15.13	2.56	7.07	1.14	0.42	0.44	50016
G26	71.10	15.46	3.00	7.31	0.94	0.75	1.45	50008
G27	73.15	14.93	2.86	8.33	0.08	0.52	0.12	50011

G28	73.26	14.58	2.57	7.74	0.39	0.26	1.2	50011
G29	70.61	14.25	4.40	8.09	0.44	0.94	1.27	50007
G30	69.00	16.69	3.78	8.49	0.47	1.19	0.38	50011
G31	71.66	14.13	2.75	9.26	1.06	0.63	0.51	50009
G32	69.67	14.85	2.98	9.05	0.75	0.51	2.18	50007
G33	73.51	15.13	2.76	6.93	0.39	1.21	0.06	50010
G34	70.74	16.47	2.95	7.63	0.60	0.55	1.05	50011
G35	68.50	16.28	3.69	8.73	0.53	0.63	1.64	50009
G36	69.94	15.64	2.92	8.00	1.06	0.99	1.45	50001
G37	72.73	16.04	3.17	7.72	0.15	0.00	0.18	50002
G38	70.27	15.73	3.37	7.35	0.49	0.89	1.91	50001
G39	70.03	15.14	3.39	8.57	0.43	0.47	1.96	50009
G40	70.92	15.92	2.80	8.11	0.58	0.29	1.37	50002
G41	70.49	16.35	4.30	7.00	0.56	0.90	0.39	50007
G42	71.43	16.15	4.04	7.69	0.02	0.31	0.35	50011
G43	73.38	14.24	2.67	6.49	0.91	0.34	1.96	50005
G44	68.08	16.98	4.27	7.20	0.29	1.16	2.02	50011
G45	69.10	15.07	4.26	8.12	0.93	0.66	1.86	50003
G46	72.53	14.09	3.45	8.43	0.25	0.35	0.88	50005
G47	70.20	15.33	3.39	7.69	0.27	0.81	2.31	50012
G48	69.71	15.75	3.18	7.94	0.95	0.51	1.96	50009
G49	69.43	14.85	4.23	8.47	0.03	0.68	2.31	50012
G50	73.87	14.57	3.10	7.09	0.43	0.48	0.46	50007
G51	70.04	14.84	4.30	7.29	0.86	0.33	2.35	50007
G52	69.52	16.64	3.50	6.81	0.93	0.52	2.08	50009
G53	69.73	16.34	3.82	6.96	0.88	0.05	2.21	50015
G54	69.91	16.09	3.64	6.81	1.06	1.25	1.25	50007
G55	71.41	14.34	2.66	9.30	0.91	0.6	0.78	50010
G56	70.26	15.14	3.15	7.73	0.86	1.03	1.84	50010
G57	69.17	15.94	3.22	7.85	0.85	0.76	2.21	50007
G58	72.86	14.36	3.38	8.29	0.54	0.04	0.53	50014
G59	68.94	15.75	3.34	8.89	0.78	0.37	1.94	50014
G60	68.29	15.63	3.80	8.73	0.68	0.92	1.96	50008
G61	69.90	15.21	4.05	8.58	0.77	0.41	1.09	50010
G62	72.69	14.38	2.56	6.96	0.58	0.98	1.85	50005
G63	71.15	15.31	3.93	7.39	1.01	0.97	0.25	50008

G64	71.70	15.26	3.22	6.68	0.96	0.71	1.47	50009
G65	68.58	15.80	4.45	9.49	0.49	0.04	1.16	50014
G66	73.32	14.65	3.83	6.66	0.43	0.49	0.63	50009
G67	69.72	15.58	3.13	9.20	0.04	0.34	1.99	50014
G68	71.69	14.44	3.46	8.96	0.26	1.06	0.13	50003
G69	72.82	14.64	3.00	8.22	0.15	0.47	0.69	50006

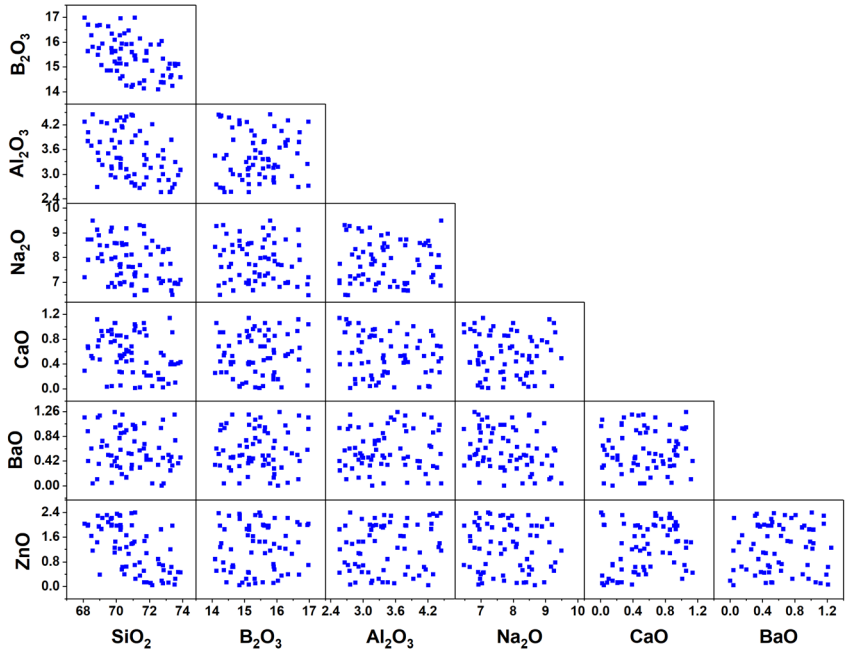

Figure 7-1. Scatter matrix plot for statistically designed glass compositions as a function of individual oxide component.

2.2 Bulk Glass Simulation

Pedone[62] potential was used to simulate the glasses for this work. The velocity verlet algorithm was used to integrate the Newton's equations of motion with a time step (Δt) of 1 fs. The electrostatic interaction was calculated via the Ewald's summation technique with a relative precision of 10^{-5} in force. Periodic boundary condition (PBC) was imposed on all three-axis. The temperature and pressure of the simulations were controlled using Berendsen thermostat and barostat, respectively. GROMACS simulation package was used to simulate bulk glass structures. The bulk glass structures for sixty-nine different glasses were simulated using ~50,000 atoms using a melt-quench technique.

The melt-quench technique is applied to represent experimental glass fabrication; however, the methodology is different. The cooling procedure in experimental preparation of a glass relies on radiative and conductive process, while in MD, the cooling procedure is performed using controlled kinetic thermostat that uniformly removes the energy of a system.

Initially, the atoms were randomly distributed in a cubic cell and held at 4000 K for 300 ps. The atoms in the cubic cell were held at a temperature of 4000 K for 300 ps and decreased to 300 K at a nominal cooling rate of 0.5 K/ps. The structures were further equilibrated at 300 K for 1ns using NPT ensemble. The glass structures were analyzed using radial distribution function (RDF), coordination number (CN), Q_n speciation, bridging oxygens (BO) and non-bridging oxygen (NBO) distributions.

2.3 Uniaxial Tensile Simulation

The uniaxial tensile simulation was performed using LAMMPS simulation package. An engineering strain of 0.01% was applied to the simulation cell for 50 ps in a NPT ensemble. The nominal strain rate was 1×10^9 s^{-1}. The strain rate used in this work is comparable to the ones used in MD studied[169–171] and is relatively fast compared to experimental strain rates. In an experimental test, strain rates achieved using a split Hopkinson tensile test set up are typically in the order of 10^3 s^{-1}. The use of fast strain rate is required by the computational resource constraints. The NPT ensemble would allow structural relaxation normal to the direction of strain. A stress-strain curve was generated from the tensile simulation. The Young's modulus (E) was measured by performing a linear fit in the elastic region of 0-0.03 strain. The pressure was held constant at 0.1 MPa (1 atm).

2.4 Temperature and Pressure Simulation fg

The structural properties and E of selected glasses were studied at various pressure condition and 300 K (27 ℃) and 287K (14 ℃). Eighteen (nine highest and nine lowest) out of sixty-nine glasses were selected based on the *E* calculated from uniaxial tensile simulation. Figure 7-2 illustrates the procedure for pressure simulation study. The pressure of the system was increased from 0.1 MPa to 1 MPa in 300 ps at a nominal rate of 0.003

MPa/ps using NPT ensemble. The 1 MPa pressure was selected because it represents a maximum hydrostatic pressure experienced by the PMT glasses in a WCD; however, the pressures in a WCD do depend on the size and several other aspects of the detector. At 1 MPa, the glass structures were equilibrated for 3 ns. Subsequently, the system pressure was decreased to 0.1 MPa in 300 ps at a nominal rate of 0.003 MPa/ps and further equilibrated at 0.1 MPa for 300 ps. The structural properties were calculated and uniaxial tensile simulations were performed after each equilibration step as shown in Figure 7-2. Furthermore, the pressure simulation steps were replicated to investigate the glass structures and *E* variation at 287 K. In this case, the temperature was reduced from 300 K to 287 K with a nominal rate of 0.026 K/ps.

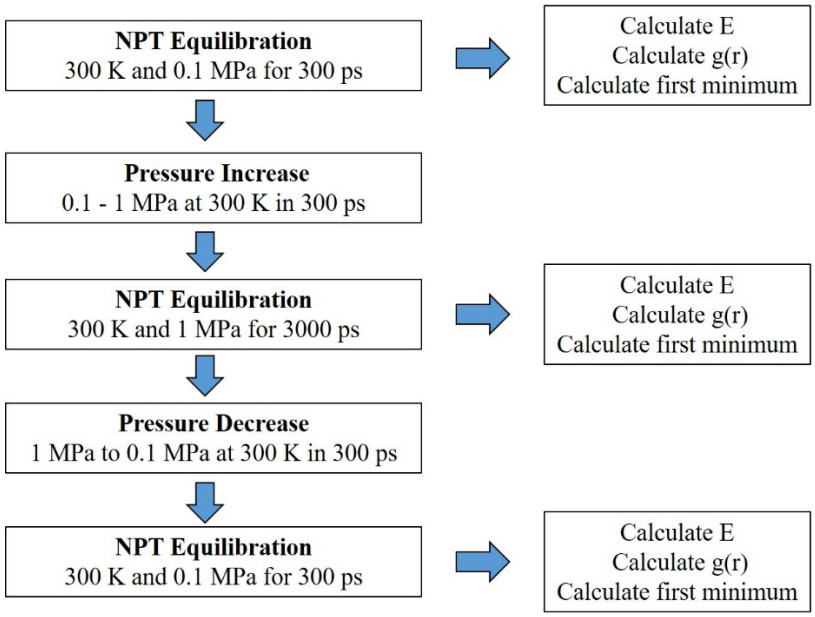

Figure 7-2. Simulation steps performed and properties calculated for the pressure effects study.

2.5 Radial Distribution Function

The conditional probability of finding another particle at a distance of r from the origin is

$$\int_{r=0}^{\infty} \rho g(r) \cdot 4\pi r^2 \, dr = N - 1 \tag{7.1}$$

where the radial distribution function (RDF), $g(r)$, is defined by Equation 7.2:

$$g(r) = \frac{1}{N\rho} \sum_{i=1}^{N} \sum_{j \neq i}^{N} \langle \delta(r + r_j - r_i) \rangle \tag{7.2}$$

where N is the number of atoms, ρ is the number density, and δ is Dirac function. The angle brackets represent a time average meaning the RDF is summed over all central atoms i and all neighbor $j \neq i$. A partial pair distribution function $g_{ij}(r)$ is the summation over one particular type of center atom i and one particular neighbor atom j.

2.6 Coordination Number Analysis

Coordination number (CN) describes the local environment of an atom by calculating the number of first nearest neighbor of the center atom i. The CN can be obtained through counting the number of atom type j within the sphere of radius r_m. The CN can be mathematically expressed as in Equation 7.3. The integral of $g(r)$ to the cutoff distance or first minimum, r_m, is used to determine the number of neighbors around a central atom.

$$CN = \int_0^{r_m} \varrho g(r) 4\pi r^2 \, dr \tag{7.3}$$

The r_m can be determined for individual cation-oxide RDF. The r_m was determined by curve fitting Equation 7.4 to the nearest values. A representative curve fit is shown in Figure 7-3.

$$y = \left(k/2\right) * (x - a)^2 + c \tag{7.4}$$

where k, a and c are parameters and the value of a is the first minimum value of a RDF plot.

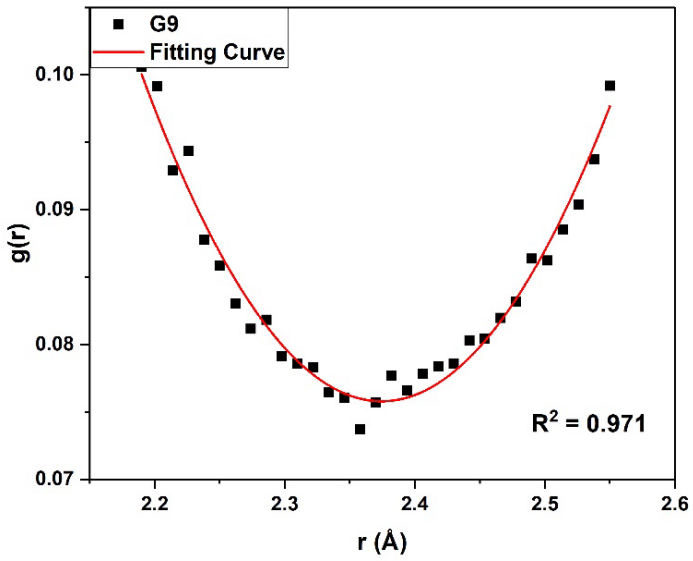

Figure 7-3. Curve fitting to determine the first minimum of a RDF plot.

The cutoff distance of all oxide RDFs was measured for all simulated glasses, and for all temperature and pressure conditions using this method. Figure 7-4 shows the r_m determined for all the oxides for selected glasses equilibrated at 300 K and 0.1 MPa. The average cutoff distance for Si-O, B-O, Al-O, Na-O, Ca-O, Ba-O, Zn-O, and O-O were 2.186±0.022 Å, 1.969±0.005 Å, 2.363±0.023 Å, 3.445±0.034 Å, 3.164±0.059 Å, 3.890±0.187 Å, 2.588±0.030 Å, and 2.951±0.012 Å, respectively. Individual cutoff distance was determined for each cation-oxygen species in the simulated glasses and used to analyze CN, Q_n species, and O environment.

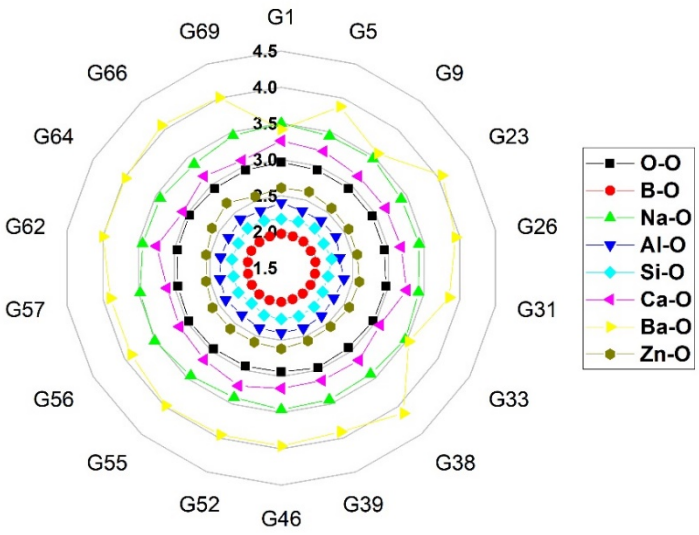

Figure 7-4. Radar plot of first minimum values for selected glasses equilibrated at 300 K and 0.1 MPa.

3. Results

3.1 Density

The density of simulated glasses was calculated by the mass of the atoms present in the glass and the volume of the simulated cell after equilibration. Table 7-II shows the calculated densities for the glasses at different temperature and pressure conditions, and predicted densities using Demkina-76 SciGlass® at 20 °C and atmospheric pressure. The explanation of the glass selection in Table 7-II is provided in Section 3.4. The glasses shown are based on the glasses selected for the temperature and pressure simulation study. The calculated densities are listed for the three pressures, initial 0.1 MPa, 1 MPa, and final 0.1 MPa, equilibrated for 300 K and 287 K. The calculated densities have higher values compared to the corresponding predicted densities. Although the predicting algorithm provides a starting point for comparison, it fails to incorporate the structural details that could possibly influence the final glass density. In addition, the glass densities calculated at different temperature and pressure conditions showed no statistical significant variations as illustrated by the box and whiskers plot in Figure 7-5. The upper and lower edges of the box represent the 25%-75% of the data set. The center marker and horizontal line inside the box represent the mean and median values of the data, and finally, the whiskers

represent the entire range of the data set. There were no statistically significant changes in calculated glass densities under the temperature and pressure simulation conditions.

Table 7-II. Density (g/cm^3) of Selected Glasses Calculated at Different Temperature and Pressure Conditions

Glass	300 K			287 K			Demkina-76
	Initial 0.1 MPa	1 MPa	Final 0.1 MPa	Initial 0.1 MPa	1 MPa	Final 0.1 MPa	
G46	2.675	2.674	2.675	2.678	2.676	2.677	2.349
G66	2.670	2.669	2.669	2.672	2.673	2.671	2.309
G9	2.664	2.664	2.664	2.667	2.666	2.667	2.352
G52	2.695	2.695	2.695	2.697	2.697	2.696	2.351
G23	2.670	2.669	2.669	2.672	2.673	2.672	2.348
G62	2.673	2.673	2.672	2.673	2.674	2.674	2.386
G69	2.661	2.662	2.660	2.663	2.662	2.663	2.346
G26	2.681	2.682	2.680	2.682	2.683	2.683	2.370
G64	2.712	2.712	2.713	2.716	2.714	2.714	2.354
G55	2.692	2.693	2.693	2.696	2.697	2.695	2.402
G1	2.664	2.662	2.662	2.664	2.665	2.665	2.326
G56	2.655	2.655	2.654	2.656	2.655	2.656	2.400
G38	2.645	2.645	2.646	2.647	2.646	2.647	2.370
G57	2.638	2.638	2.638	2.641	2.640	2.640	2.389
G5	2.686	2.686	2.687	2.687	2.688	2.687	2.303
G33	2.674	2.673	2.674	2.676	2.676	2.677	2.353
G31	2.683	2.681	2.682	2.682	2.683	2.685	2.402
G39	2.644	2.647	2.646	2.648	2.648	2.647	2.377

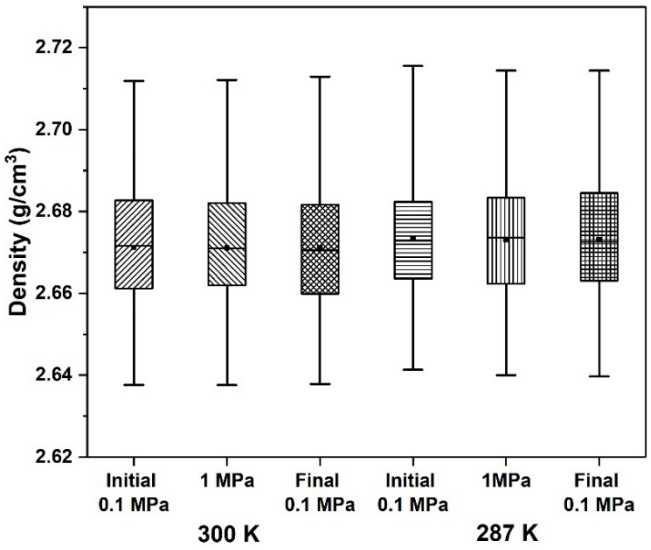

Figure 7-5. Box and whisker plot showing the statistical distribution of calculated densities.

3.2 Radial Distribution Function

Figure 7-6 shows a representative RDF plot for a simulated glass. The RDF plot of each oxide was calculated using the final 300 trajectories of the equilibration steps. Each trajectory was 1 ps apart. The bond lengths derived from RDF are presented in Table 7-III, which shows that the calculated values are in good agreement with previous MD and experimental works. The RDF was calculated for all temperature and pressure conditions.

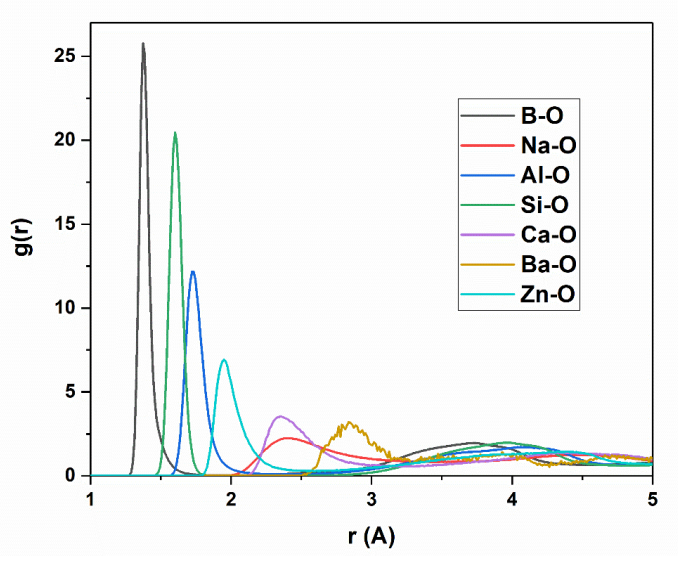

Figure 7-6. RDF plots for cation-oxide.

Table 7-III. Bond Length (Å) Comparison with MD and Experimental Values

	This work	Pedone[62]	MD	Experimental
Si-O	1.602	1.616/1.618	1.600[133]	1.608,[162] 1.620[172]
B-O	1.374-1.377	---	1.390,[173] 1.400-1.470[174]	1.370-1.470[175]
Al-O	1.730-1.734	---	1.740,[133] 1.730[171]	1.750,[176] 1.770[166]
Na-O	2.400-2.405	2.307	2.420,[133] 2.390[173]	2.360-2.388,[172] 2.300-2.430[177]
Ba-O	2.828-2.852	---	---	2.700[178]
Ca-O	2.345-2.535	---	---	2.320[176]
Zn-O	1.949-1.957	---	---	1.960[179]
O-O	2.598-2.601	2.624/2.626	2.610-2.640[171]	2.626[162], 2.650[172]

The corresponding bond distances were determined from first peak of RDFs. Table 7-III represents the bond length for cation-oxide and O-O species. The second column list the range of average bond lengths measured in this work for the 18 selected glasses simulated at 300 K and 0.1 MPa. Columns three, four and five shows the bond lengths reported in Pedone et al. work,[62] other MD and experimental works, respectively. The B-O has the smallest bond length of 1.374-1.377 Å. The B-O bond length is a contribution of 3-coordinated $^{[3]}$B-O and 4-coordinated $^{[4]}$B-O. Previous MD study on sodium boroaluminosilicate glasses reported bond length of $^{[3]}$B-O and $^{[4]}$B-O at 1.40 Å and 1.47 Å, respectively.[174] Additionally, previous experimental study on vitreous boron oxide structure for $^{[3]}$B and $^{[4]}$B are 1.37 Å and 1.47 Å, respectively.[175] The bond length reported in this work is closer to $^{[3]}$B-O as there is higher percentage of $^{[3]}$B than $^{[4]}$B in the simulated glasses. The concentration of B species in glasses is discussed later in the chapter. The Si-O bond length is 1.602. The bond lengths calculated are in good agreement with reported values shown in Table 7-III. The bond length for Al-O is 1.733, which is in good agreement with previously reported values. *Ab initio* simulation and experimental results showed Al-O distance of 1.71 and 1.77 Å.[180,181] The Al-O bond length is a contribution of 4-, 5-, and 6-coordinated Al. In previously study, it has been shown that the 4-coordinate Al has smaller bond length (1.81 Å),[182] 5-coordinated Al (1.83 Å)[183] and 6-coordinated Al (1.91 Å).[184]

The O-O distance reported in this work is in agreement with the reported values shown in Table 7-III. There are no real O-O bonds in the glass; however, reporting these values provide a reference to compare the glass structures. The modifier cation-oxygen bond lengths for Na, Ca and Ba were determined to be 2.404 Å, 2.345 Å, and 2.838 Å, respectively. The Ca-O bond length is smaller than Na-O due to higher charge of Ca. The Ba-O is the largest bond length among all the elements in the glass, which is consistent with the size of the Ba ion. The average Zn-O bond length was determined to be 1.949 Å. The value is in good agreement with the experimental value reported. Additionally, Zn-O shows a well-defined RDF comparable to glass forming elements Si, B and Al. A considerable skewness of Zn-O is observed, it could be due to the presence of higher (5- and 6-) coordinated Zn. It should be noted that the glass former bond length showed minimal to no deviation from the average value; however, modifier ions showed a larger deviation. This deviation could be due to the different local environment of the modifier ions in the glasses, which could be explained through coordination analysis.

Furthermore, bond lengths were determined for glass structures equilibrated at different temperature and pressure conditions. Table 7-IV shows the average bond length determined for bonding species at different temperature and pressure conditions. The values in the bracket represent last two decimal places of the standard deviation for the 18 glasses studied. Under the pressurized and depressurized conditions, the bond lengths for glass formers and O-O species showed small to no changes. The Si-O and B-O bond length remained constant throughout the temperature and pressure simulation. The average bond length determined for modifier ions (Na^{+}, Ca^{2+} and Ba^{2+}), on the other hand showed small changes and higher standard deviations. These changes could be associated with the pressure effects; however, the change in bond length did not show a linear relationship with changing conditions. As the glass formers form a strong covalent bond, they could be less susceptible to change during pressurization at 300 K and 287 K. However, due to the ionic nature of the modifier ions bond, the small changes could be a result of external environmental influences.

Table 7-IV. Average Bond Length (Å) Calculated for All Oxides at Different Temperature and Pressure Conditions. The Values in the Bracket Show the Standard Deviation for the 18 Selected Glasses

	287 K			300 K		
	Initial 0.1 MPa	**1 MPa**	**Final 0.1 MPa**	**Initial 0.1 MPa**	**1 MPa**	**Final 0.1 MPa**
O-O	2.600 (04)	2.598 (00)	2.600 (04)	2.603 (08)	2.598 (00)	2.601 (05)
Al-O	1.733 (03)	1.734 (00)	1.734 (00)	1.730 (07)	1.734 (00)	1.734 (00)
B-O	1.374 (00)	1.374 (00)	1.374 (00)	1.377 (00)	1.374 (00)	1.374 (00)
Si-O	1.602 (00)	1.602 (00)	1.602 (00)	1.602 (00)	1.602 (00)	1.602 (00)
Na-O	2.404 (15)	2.401 (10)	2.401 (19)	2.405 (34)	2.400 (10)	2.402 (14)
Zn-O	1.949 (05)	1.949 (04)	1.951 (06)	1.957 (17)	1.949 (04)	1.949 (07)
Ba-O	2.838 (47)	2.852 (48)	2.833 (40)	2.852 (88)	2.828 (41)	2.838 (48)
Ca-O	2.345 (18)	2.353 (16)	2.353 (17)	2.347 (34)	2.355 (15)	2.351 (16)

3.2.1. Coordination Number Analysis

Table 7-V shows the average CN calculated for eighteen glasses subjected to the temperature and pressure simulation. The bracket values represent last two decimal places of the standard deviation. The CN for glass formers Si, B, and Al was 4.00, 3.18, and 4.10, respectively and these values did not change on application of pressure. The coordination for modifier ions were found to be higher than compared to the glass formers. The average coordination for Na, Ca, and Ba was calculated to be 8.62-8.76, 6.76-7.07, and 10.73-11.47, respectively. Although the average CN values were similar for different temperature and pressure conditions, the standard deviation suggests a larger distribution in the average CN. The average coordination of Zn was calculated to be 4.27-4.39 with a smaller standard deviation. The coordination of Zn was similar to Si and Al. The CN of the elements are further analyzed in the following sections.

Table 7-V. Coordination Number for the Glass Constituents

Element	300 K			287 K		
	Initial 0.1 MPa	1 MPa	Final 0.1 MPa	Initial 0.1 MPa	1 MPa	Final 0.1 MPa
Si	4.00 (00)	4.00 (00)	4.00 (00)	4.00 (00)	4.00 (00)	4.00 (00)
B	3.18 (00)	3.18 (00)	3.18 (00)	3.18 (00)	3.19 (00)	3.18 (00)
Al	4.13 (00)	4.10 (00)	4.10 (00)	4.10 (00)	4.10 (00)	4.10 (00)
O	1.98 (00)	1.97 (00)	1.97 (00)	1.97 (00)	1.97 (00)	1.97 (00)
Na	8.76 (05)	8.62 (06)	8.62 (06)	8.62 (06)	8.63 (06)	8.63 (06)
Ca	7.07 (08)	6.80 (09)	6.76 (08)	6.79 (09)	6.81 (08)	6.79 (07)
Ba	10.73 (69)	11.47 (25)	11.40 (29)	11.29 (33)	11.15 (30)	11.26 (34)
Zn	4.39 (02)	4.27 (02)	4.27 (02)	4.28 (02)	4.28 (02)	4.28 (02)

3.2.1.1. Glass Former Coordination

Glass formers play an important role in determining the glass structure. The bonding environment of the glass formers are essential in predicting the structures and the properties of a glass. In the simulated glasses, Si is almost entirely 4-coordinated (>99.5%) with a small amount of 5-coordinated Si, shown in Table 7-VI. The explanation of the glass selection in Table 7-VI is provided in Section 3.4. The 4-coordinated Si form tetrahedral glass forming units. B, on the other hand, is found in two distinct coordination number 3 and 4. In the simulated glasses, most of B atoms are 3-fold coordinated. The 4-coordinated B requires a charge compensating modifier ions. Additionally, the Al was found in 4- and 5-fold coordination. The 5-coordinated Al has been reported in previous studies.[185] In the simulated glasses, the 5-coordinated Al was found to be between 9.6-14.1%. In the MD study performed by Xiang et al.,[133] higher amount of 5-coordinated Al was observed using Pedone potential for short range interaction. In aluminoborosilicate glasses, the Al and B compete for the modifier ions for charge compensation of the negatively charged $[AlO_4]^-$ and $[BO_4]^-$ structural units.

Table 7-VI. Coordination Number of Si, B and Al in the Simulated Glasses

Glass	Si		B		Al	
	4	5	3	4	4	5
G46	99.6	0.4	80.1	19.9	87.6	11.8
G66	99.5	0.5	79.4	20.6	88.0	10.5
G9	99.6	0.4	81.5	18.5	86.9	11.9
G52	99.7	0.3	79.5	20.5	88.6	10.7
G23	99.6	0.4	81.4	18.6	89.0	10.4
G62	99.7	0.3	81.1	18.9	86.7	12.4
G69	99.5	0.5	80.9	19.1	87.7	10.8
G26	99.5	0.5	78.7	21.3	89.3	10.3
G64	99.6	0.4	80.4	19.6	87.7	11.7
G55	99.9	0.1	82.4	17.6	87.0	11.8
G1	99.7	0.3	84.9	15.1	86.1	12.4
G56	99.8	0.2	83.7	16.3	88.3	10.9
G38	99.6	0.4	80.7	19.3	85.8	13.3
G57	99.7	0.3	82.8	17.2	89.8	9.6
G5	99.7	0.3	81.9	18.1	89.9	9.6
G33	99.8	0.2	83.6	16.4	87.3	11.3
G31	99.7	0.3	81.9	18.1	85.4	13.4
G39	99.6	0.4	83.7	16.3	85.2	14.1

Figure 7-7 shows a linear relationship for the atomic percent of Si and the number of 4-coordinated Si atoms in the simulated glasses. The plot shows that almost all Si were completely 4-coordinated. A small amount of 5-coordinated Si, 0.35±0.10 %, was observed. Previous experimental work has reported observation of 5-coordinated Si atoms.[186]

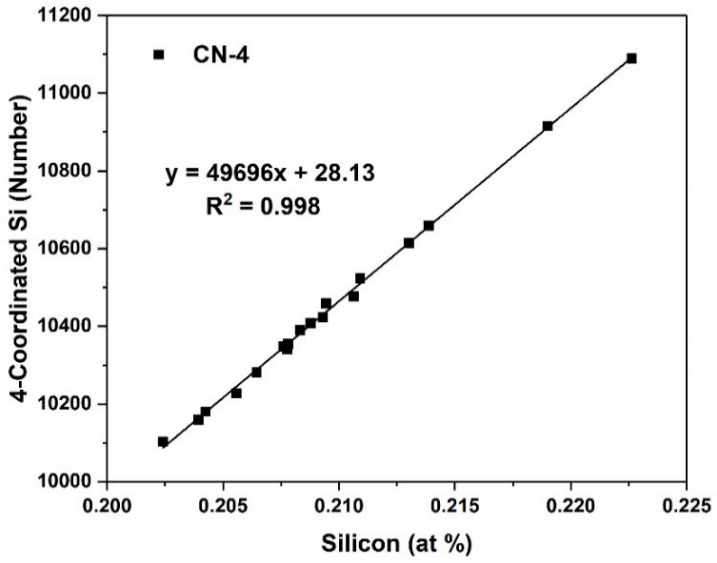

Figure 7-7. 4-coordinated Si as a function of atomic percent of Si

Figure 7-8 shows the relationship between the atomic percent of B and the 3- and 4-coordinated B atoms in the simulated glasses. The 3-coordinated B atoms show a moderate degree of linearity with the amount of B atoms in the glasses with the coefficient of determination (R^2) equal to 0.825, which suggests that the B primarily forms 3-coordinated structures within the compositional space we have studied. The 4-coordinated B atoms, on the other hand, do not show a strong correlation (R^2 = 0.122) with the concentration of B in the glasses. It is known that the formation of 4-coordinated B requires a charge compensating modifier ions (e.g. Na^+). The simulated glasses contain both alkali and alkaline earth modifier ions, whose presence promotes the formation of 4-coordinated B in aluminoborosilicate glasses. The relationship between the B coordination and Na concentration will be discussed later in Section 4.4.

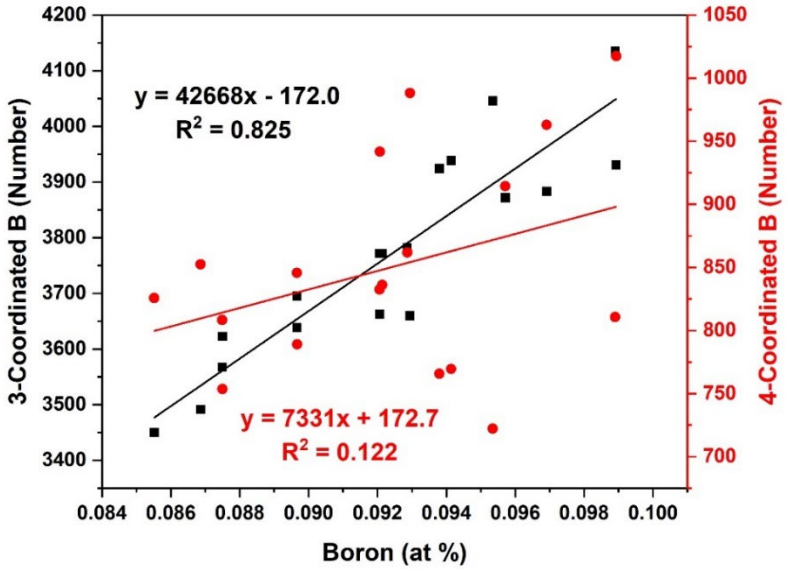

Figure 7-8. 3- and 4-fold coordination of B atoms as a function of B concentration.

Figure 7-9 shows the relationships between the atomic percent of Al and the number of 4- and 5-coordinated Al atoms in the simulated glasses. Both coordination showed a strong linear correlation with the increasing amount of Al in the glasses. The R^2 values of 0.993 and 0.844 were calculated for 4- and 5-coordinated Al, respectively. In addition, a minor (0.9±0.1%) amount of 6-coordinated Al was observed. The higher coordinated Al has been reported in previous MD work.[185] Higher Al coordination (5 or 6) usually exist when there are not enough alkali and alkaline earth for charge compensation.

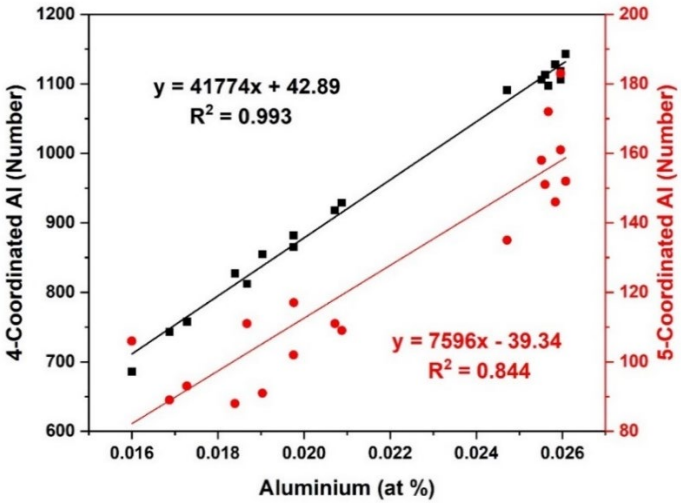

Figure 7-9. 4- and 5-fold coordination of Al atoms as a function of Al concentration.

3.2.1.2. Oxygen Coordination

The local environment of oxygen in a glass structure can be differentiated into BO, NBO and oxygen tricluster (TBO). The BO bridges two glass forming structural units of Si, B and Al, thus is 2-coordinated. The NBO is a terminal oxygen atom in the glass former tetrahedral associated with a modifier cation and in 1-coordinated. The presence of TBO has been reported in previous work[133] on multicomponent aluminoborosilicate glasses; however, its role is not fully understood. Although the formation of TBOs are energetically unfavorable, it is assumed that TBOs energetically balances structure such as an O atom bonded to two Al and one Si. Figure 7-10 shows the distribution of the 1-, 2-, and 3-coordinated O in the simulated glasses at 300 K and 0.1 MPa. In the simulated glasses, 93.4±0.6% were BO, 4.4±1.0% of O atoms were NBO, and 2.2±0.7% were TBO. A high BO percentage suggests highly polymerized glass structure. Moreover, the presence of NBOs suggest that the Na atoms not only act as a charge compensator for 4-coordinated B and Al but also create terminal oxygens at Si and B.

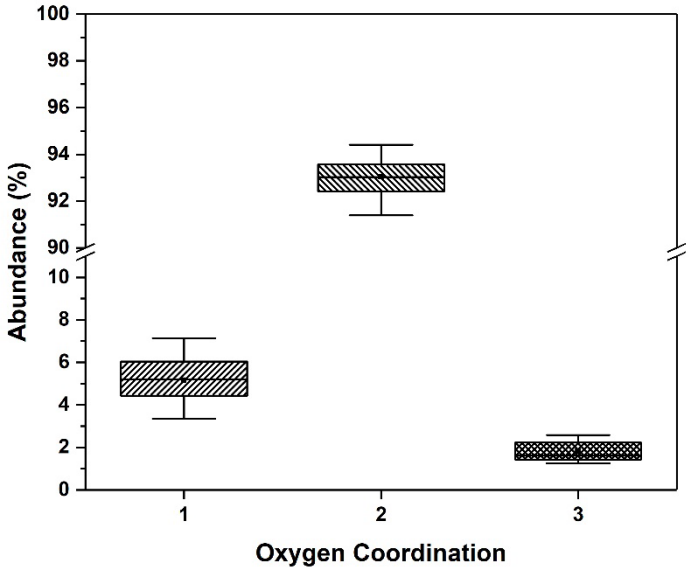

Figure 7-10. Box and whiskers plot for CN distribution of Oxygen.

3.2.1.3. Glass Modifier Ions Coordination

The addition of alkali and alkaline earth metals in a aluminoborosilicate glass modifies the glass structure by creating a NBO in the Si and B network or acting as a charge compensator for 4-coordinated Al and B tetrahedral structural units. The modifier ions form non-directional ionic bonds in the glass structure. In general, the coordination of modifier ions (e.g. Na^{+}, Ca^{2+}, Ba^{2+}, etc.) are higher than those of the glass formers.

The average coordination number of Na was calculated to be 8.61-8.76 as shown in earlier Section. In the simulated glasses, the CN of Na was calculated to be between 4 and 13. Figure 7-11 shows linear relationships between different CN of Na and its atomic percentage of Na in the glass. The CN are identified by a prefix of 'CN-'. The R^2 values suggest good correlations. The degree of linearity between different coordination numbers and Na concentration vary, indicating that Na preferentially occupies 8 and 9 coordination. High average coordination number for Na of 6-7 in silicate and 7-8 for aluminosilicate glasses have been confirmed through NMR studies.[187]

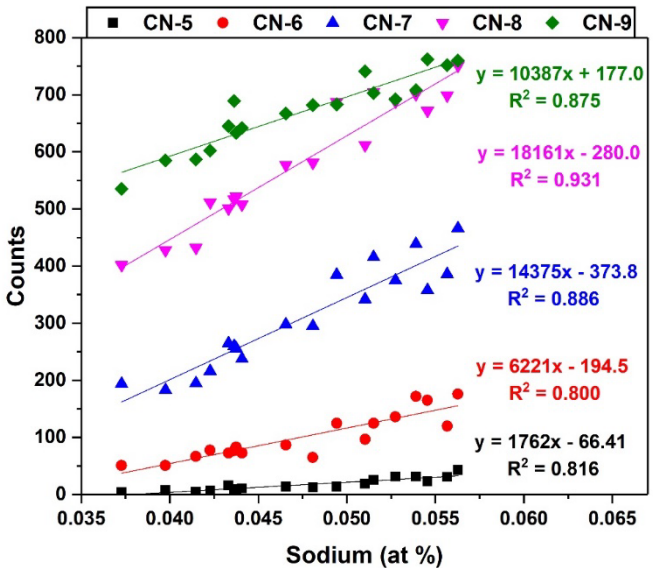

Figure 7-11. Correlations of CN distribution to atomic percentage of Na atoms.

Figures 7-12 and 7-13 show the linear relationship between different CN and atomic percentages of Ca and Ba, respectively. Similar to Na, Ca and Ba show high degree of correlation with multiple CN distributions. The R^2 values suggest high degree of correlation between preferred coordination and atomic percentages. The average coordination of Ca was lower compared to Na and Ba as listed in Table 7-V. The CN of Ca was found between 4 and 11, with preference to 7 and 8 coordination as shown in Figure 7-12. Ba, on the other hand, was calculated to have higher coordination between 8-15. Figure 7-13 shows that most of Ba ions were found to be between 10-14 coordinated. In general, the Ba coordination was higher than either Na or Ca. This could be due to the larger ionic size and ionic charge of Ba. It should be noted that the concentrations of Ca and Ba were small compared to Si, B, Al and Na content, which is primarily due to the composition of the commercial PMT glasses.

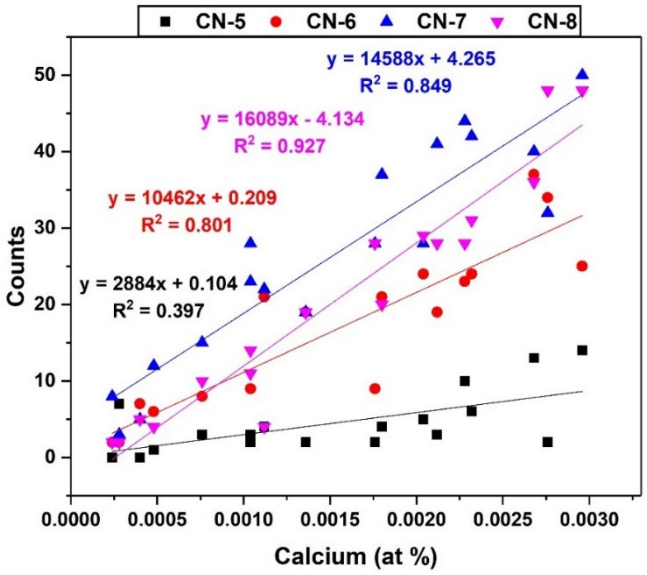

Figure 7-12. Correlations of CN distribution to atomic percentage of Ca atoms.

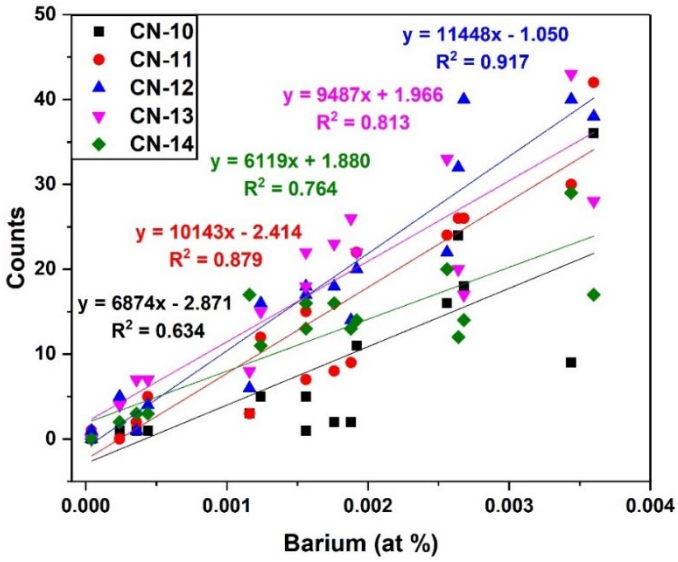

Figure 7-13. Correlations of CN distribution to atomic percentage of Ba atoms.

3.2.1.4. Zinc Coordination

Zinc plays a role of an intermediate (much like Al) in glasses. Figure 7-14 shows the variation of CN of Zn as a function to the atomic percentage of Zn. In the simulated glasses, Zn was primarily observed in 4- and 5-fold coordination with a small amount of 6-coordinated Zn. A high degree of linearity was observed for 4- and 5-coordinated Zn within the compositional space we have studied with R^2 values of 0.994 and 0.899, respectively. Previous studies of Zn structures in silicate, borosilicate and aluminoborosilicate glasses have shown that Zn prefers 4-fold coordination but is also able to form higher coordinated structures.[188] Similar to Ca and Ba concentrations, the percentage of Zn in the simulated glasses was small compared to Si, B, Al, and Na concentrations.

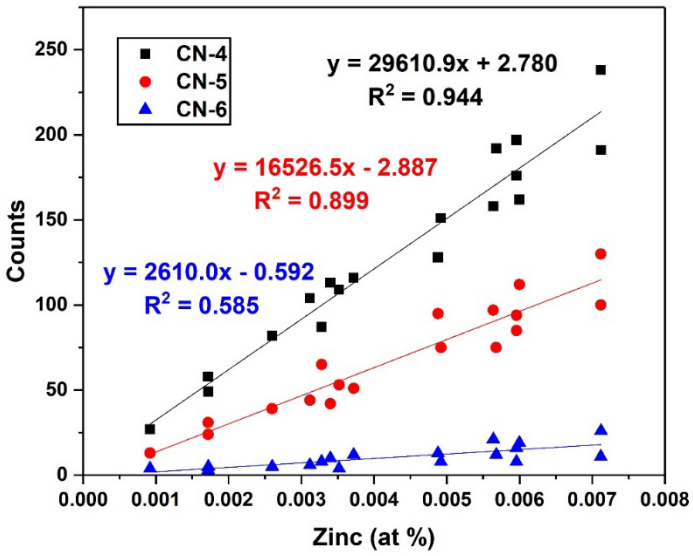

Figure 7-14. Correlation between CN of Zn and number of Zn atoms.

3.3 Q_n Speciation

The Q_n speciation describes the nature of glass forming tetrahedral unit in terms of the BO and NBO associated with it, e.g., a tetrahedral unit with 4 BO is Q_4 species, 3 BO is Q_3 species, and so forth. The Q_n distribution provides important information about how the network formers connect with each other. The network connecting the structural units for the glass former cations are Si-O-Al, Si-O-B, and B-O-Al, in addition to the similar glass former connection. Table 7-VII shows the Q_n species for [SiO_n] and [AlO_n] polyhedrons. The values in Table 7-VII are listed with the lowest E values at the top and highest E values at the bottom, in ascending order. The 4-coordinated Si was primarily found in Q_4 units, suggesting high connectivity of network formers. The Q_4 speciation for Si suggests that the low-E glasses have lower Q_4 units compared to high-E glasses. Conversely, The Q_3 unit shows decreasing number for higher E glasses. The small amount of 5-coordinated Si was almost entirely in Q_5 speciation. However, it should be noted that only a small percentage of Si was 5-coordinated in the simulated glasses. Similarly, both 4- and 5-coordinated Al were also entirely found in Q_4 and Q_5 species, respectively. It suggests that the Al in the simulated glasses were connected to the other network formers in the glass network. The presence of lower Q_n species for 4- and 5-coordinated Al has been reported in MD work.[185]

Table 7-VII. Percentage of Q_n Speciation of [SiO_n] and [AlO_n] Units in the Simulated Glasses

Glass	[SiO_4]			[SiO_5]		[AlO_4]		[AlO_5]	
	Q_2	Q_3	Q_4	Q_4	Q_5	Q_3	Q_4	Q_4	Q_5
G46	0.6	12.7	86.8	5.9	94.1	0.6	99.4	0.0	100.0
G66	0.5	11.9	87.6	0.0	100.0	0.7	99.3	0.0	100.0
G9	0.6	13.1	86.3	0.0	100.0	1.3	98.7	0.0	100.0
G52	0.8	14.2	85.0	4.8	95.2	1.3	98.7	1.1	98.9
G23	0.4	12.5	87.1	0.0	100.0	0.7	99.3	0.0	100.0
G62	0.4	10.3	89.4	0.0	100.0	0.5	99.5	0.0	100.0
G69	0.3	10.7	89.0	0.0	100.0	0.9	99.1	0.0	100.0
G26	0.3	11.4	88.3	0.0	100.0	0.8	99.2	1.4	98.6
G64	0.5	12.8	86.7	0.0	100.0	0.8	99.2	0.0	100.0
G55	0.4	10.5	89.1	0.0	100.0	1.2	98.8	0.0	100.0
G1	0.2	7.7	92.0	13.3	86.7	0.6	99.4	0.7	99.3
G56	0.1	7.1	92.8	0.0	100.0	0.6	99.4	0.0	100.0
G38	0.2	9.1	90.6	0.0	100.0	0.7	99.3	0.0	100.0
G57	0.3	9.0	90.7	0.0	100.0	0.6	99.4	0.0	100.0
G5	0.4	10.9	88.7	0.0	100.0	1.3	98.7	1.4	98.6
G33	0.4	9.4	90.2	0.0	100.0	0.7	99.3	1.0	99.0
G31	0.3	9.3	90.4	7.1	92.9	0.7	99.3	0.0	100.0
G39	0.2	7.2	92.6	6.7	93.3	0.7	99.3	0.8	99.2

The relative abundance of B atoms in 3- and 4-fold coordination in terms of atomic percentage of B atoms has been discussed earlier. Unlike the Si and Al, 3- and 4-coordinated B were observed in significant amount. Table 7-VIII shows the Q_n distribution of 3-coordianted B [BO_3] and 4-coordinated B [BO_4] units. The main species were Q_3 and Q_4 for [BO_3] and [BO_4] units, respectively. The explanation of the glass selection in Table 7-VIII is provided in Section 3.4. The presence of Q_2 and Q_1 species for [BO_3] units and Q_3 species for [BO_4] units are due to the association of NBO with B polyhedral units. The observation of Q_3 species for [BO_4] units have been reported by Deng et al.[185] The presence of lower Q_n speciation of 3- and 4-coordinated B suggests that B does not completely convert from [BO_3] to [BO_4] unit in the presence of Na atoms. The Na concentration in the simulated glasses is higher than the Al concentration. The excess Na first converts the [BO_3] to [BO_4]; however, as observed not all the [BO_3] units are converted to [BO_4], which leads to the formation of lower Q_n units at Si and B glass forming units. In Table 7-VIII,

the glasses with higher E have higher Q_3 speciation of [BO_3] units. The abundance of Q_n speciation of Si and B and their effects on Young's modulus are discussed in detail below.

Table 7-VIII. Percentage of Q_n Speciation of [BO_n] Units in the Simulated Glasses

	[BO_3]			[BO_4]	
Glass	**Q_1**	**Q_2**	**Q_3**	**Q_3**	**Q_4**
G46	0.4	9.9	89.7	3.1	96.9
G66	0.3	10.2	89.6	3.9	96.1
G9	0.4	12.4	87.2	3.6	96.4
G52	0.6	12.8	86.7	6.7	93.3
G23	0.3	11.4	88.3	4.4	95.6
G62	0.2	9.8	90.0	3.9	96.1
G69	0.3	9.7	89.9	3.0	96.9
G26	0.3	10.1	89.6	4.1	95.9
G64	0.3	11.8	87.9	5.5	94.5
G55	0.2	10.1	89.6	3.2	96.8
G1	0.2	7.3	92.5	1.9	98.1
G56	0.1	6.4	93.5	2.0	98.0
G38	0.2	8.3	91.5	3.4	96.6
G57	0.2	7.9	91.9	2.5	97.5
G5	0.3	10.0	89.7	4.0	95.9
G33	0.2	8.5	91.3	3.3	96.5
G31	0.1	7.9	92.0	2.8	97.2
G39	0.2	6.5	93.3	2.1	97.9

3.4 Young's Modulus

The E values calculated for selected glasses at different temperature and pressure conditions are shown in Table 7-IX. Eighteen glasses were selected based on the E values calculated at 300 K and 0.1 MPa, nine glasses with high-E and nine glasses with low-E. In Table 7-IX, these glasses are listed in ascending order of Young's modulus. The first nine glasses (indicated by green fonts) are low-E glasses and the rest are high-E glasses. Figure 7-15 shows the average E value for the low-E (red) and high-E (blue) glasses calculated for all the temperature and pressure condition simulations. The error bars represent one standard deviation of uncertainty. The color and error bar representations for similar graphical illustrations are followed for rest of the work unless it is explicitly specified.

The average E values of low-E glasses simulated at 300 K were 83.80±0.85 GPa, 85.34±2.06 GPa, and 86.32±1.59 GPa for initial 0.1 MPa, 1 MPa, and final 0.1 MPa

pressures, respectively. For high-E glasses at 300 K, 90.68±1.09 GPa, 90.88±0.92 GPa and 91.04±1.70 GPa were calculated for initial 0.1 MPa, 1 MPa, and final 0.1 MPa pressures, respectively. At 287 K, the average E values of low-E glasses was 85.87±1.52 GPa, 84.55±1.54 GPa, and 85.96±2.13 GPa for initial 0.1 MPa, 1 MPa, and final 0.1 MPa pressures, respectively; and high-E glasses were 89.07±1.47 GPa, 89.34±1.75 GPa, and 89.60±1.48 GPa for initial 0.1 MPa, 1 MPa, and final 0.1 MPa pressures, respectively. In general, the average E values calculated for different temperature and pressure conditions were within one standard deviation. Our results show that no significant change in Young's modulus were observed for glasses simulated at different temperature and pressure conditions. Although no statistical variations of E were observed for the simulated temperature and pressure conditions within the compositional space studied, additional composition-structure and structure-properties were investigated and are presented below in Section 4.

Table 7-IX. Young's Modulus (GPa) Calculated for Selected Glasses

Formulation	300 K			287 K		
	Initial 0.1 MPa	1 MPa	Final 0.1 MPa	Initial 0.1 MPa	1 MPa	Final 0.1 MPa
G46	82.07	85.49	87.42	85.90	84.73	86.43
G66	83.11	83.54	84.74	85.01	85.16	86.03
G9	83.40	82.28	86.32	84.75	81.65	82.76
G52	83.40	83.54	83.34	83.73	83.82	82.72
G23	83.85	85.17	85.14	85.02	82.52	84.15
G62	84.32	86.35	86.23	86.17	86.19	87.57
G69	84.48	89.75	88.55	87.62	85.58	88.04
G26	84.80	86.80	88.23	89.11	86.57	86.97
G64	84.82	85.18	86.90	85.56	84.77	88.95
G55	89.16	89.27	87.72	88.47	87.29	87.55
G1	89.16	91.15	92.95	87.97	91.39	88.94
G56	89.97	90.40	90.33	90.10	87.24	90.04
G38	90.20	90.34	92.80	88.99	89.54	89.18
G57	90.58	90.86	89.50	88.19	88.22	87.55
G5	91.21	92.21	93.21	90.79	91.40	90.97
G33	91.54	90.26	91.54	87.15	90.25	89.27
G31	91.94	91.12	91.02	88.04	87.33	90.64
G39	92.33	92.35	90.26	91.94	91.42	92.31

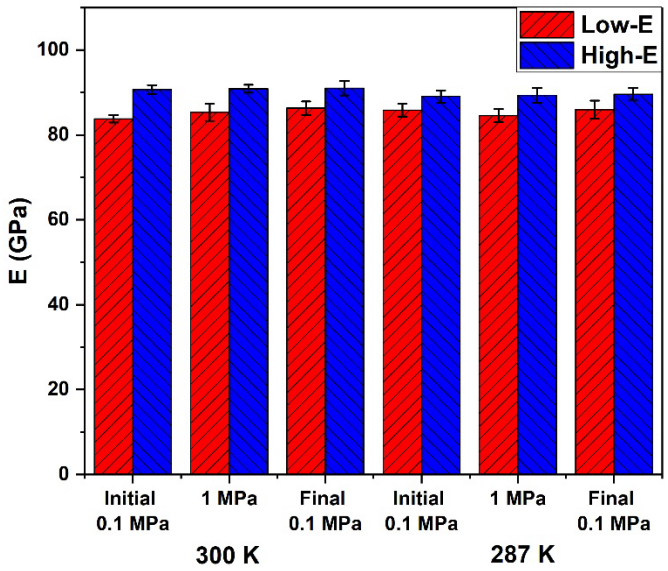

Figure 7-15. Statistical variations in the low- and high-E glass at various temperature and pressure conditions.

4. Discussions

4.1 Young's Modulus and Oxygen Environment

The E of the simulated glasses were investigated in terms of oxygen environment, NBO and BO distributions. Figure 7-16 (a) and (b) show the distribution of BO and NBO abundance calculated for the low-E and high-E glasses at different temperature and pressure conditions. In Figure 7-16 (a), the percentage of BO in low-E glasses were 92.47±0.62%, 92.45±0.59%, and 92.48±0.61% for initial 0.1 MPa, 1 MPa, and final 0.1 MPa pressures, respectively at 300 K. For high-E glasses, the BO concentration were slightly higher with 93.61±0.61%, 93.62±0.60%, and 93.61±0.62% for initial 0.1 MPa, 1 MPa, and final 0.1 MPa pressures, respectively at 300 K. Additionally, in Figure 7-16 (b), the NBO abundance in low-E glasses at 300 K were 5.94±0.63%, 5.96±0.61, and 5.95±0.63% for initial 0.1 MPa, 1 MPa, and final 0.1 MPa pressures, respectively. For high-E glasses at 300K, 4.35±0.66%, 4.35±0.65%, and 4.36±0.67% of NBO concentrations were calculated for initial 0.1 MPa, 1 MPa, and final 0.1 MPa pressures, respectively. In general, the abundance of BO in low-E glasses was lower than that of high-E glasses. On the contrary, higher NBO concentration were found in low-E glasses. Similar BO and NBO distributions in low-E and high-E glasses were observed for glasses simulated at 287

K. Our results show that under the simulated conditions, the BO and NBO concentrations do not undergo significant change, which is an expected result due to small strains induced by the application of 1 MPa hydrostatic pressure on the simulated glasses.

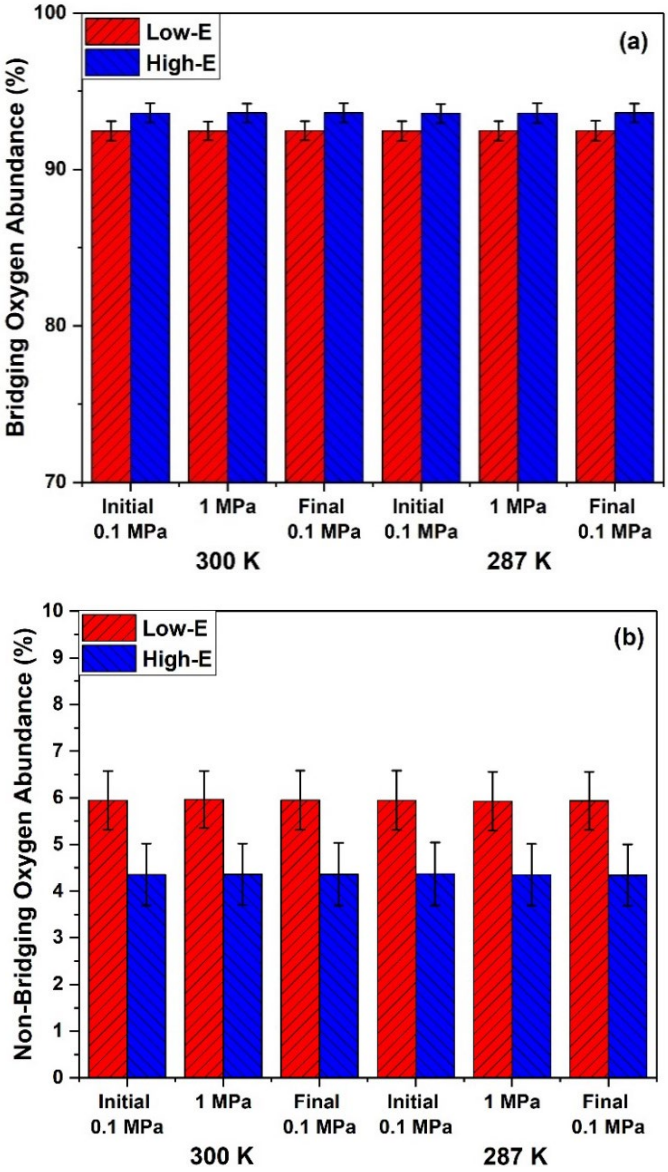

Figure 7-16. (a) BO and (b) NBO atom abundance for different temperature and pressure simulation studies

Furthermore, the relationship between E and NBO concentration for the eighteen selected glasses within the compositional space studied is shown in Figure 7-17. Figure 7-17 shows that values calculated for glasses equilibrated at 300 K and 0.1 MPa. The NBOs associated with B (B-NBO (black)) and Si (Si-NBO (red)) structural units along with the

total amount of NBO (All-NBO (blue)) in the simulated glasses are shown. A linear regression was performed for B-NBO, Si-NBO and All-NBO concentration, which resulted in the coefficient of determination (R^2) of 0.60, 0.61 and 0.61, respectively. The values of the R^2 suggests a moderate correlation. Additionally, it indicates that the variation in calculated E does not entirely depend on the NBO concentration and most likely are affected by other structural properties. On comparison, higher amount of NBOs were associated with Si than B. This is due to the fact that creating a NBO at Si tetrahedral is energetically favorable than at B structural units. Overall, all glasses with higher NBO concentration have lower E compared to glasses with lower NBO concentration. The presence of NBO in the glasses indicate the extent of depolymerization of the glass network. Glasses with lower NBO concentration would be more polymerized, hence would require more energy for deformation under stress resulting in higher E values.

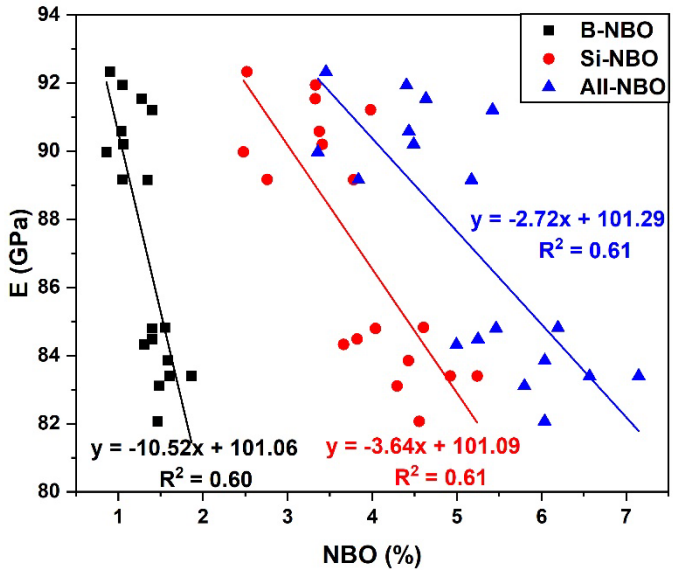

Figure 7-17. Correlation between E and NBO for glasses equilibrated at 300 K and 0.1 MPa

4.2 Young's Modulus and Coordination Number

The distribution of coordination number (CN) in low- and high-E glasses are discussed in this section. The CN of these glasses were analyzed separately. Figure 7-18 shows the average value calculated for the prominent coordination of Si, B and Al

calculated for glasses equilibrated at 300 K and 0.1 MPa. In Figure 7-18, the values are reported for 4-coordinated Si (4-Si), 3- and 4-coordinated B (3-B and 4-B, respectively), and 4-coordinated Al (4-Al). The 4-coordinated Si were 99.59±0.07% and 99.71±0.08% for the low- and high-E glasses, respectively. The abundance of 3-coordinated B was 80.36±0.92% and 82.83±1.18% for low- and high-E glasses, respectively, and 4-coordinated B was 19.64±0.92% and 17.17±1.18% for low- and high-E glasses, respectively. The 3- and 4-coordinated B showed small change in the average values. The abundance of 4- and 5-coordinated Al were 87.94±0.82% and 11.17±0.72%, respectively for low-E glasses, and 87.20±1.68% and 11.81±1.54% for high-E glasses. The variation in distribution of 4- and 5-coordinated Al for low- and high-E are within one standard deviation.

Ideally, higher amount of 4-coordinated B is associated with glasses with higher E because it promotes polymerization of glass network structure. However, in the simulated glasses within the compositional space studied, high-E glasses were associated with lower 4-coordinated B glasses compared to low-E glasses. A reason for this behavior could be due to the interactions of multiple glass formers and the complex role of alkali ions (Na^+) in these glasses with multiple competing roles including charge compensation for $[AlO_4]^-$ and $[BO_4]^-$, conversion of 3-coordinated to 4-coordianted B, and creating NBOs on Si and B structural units.

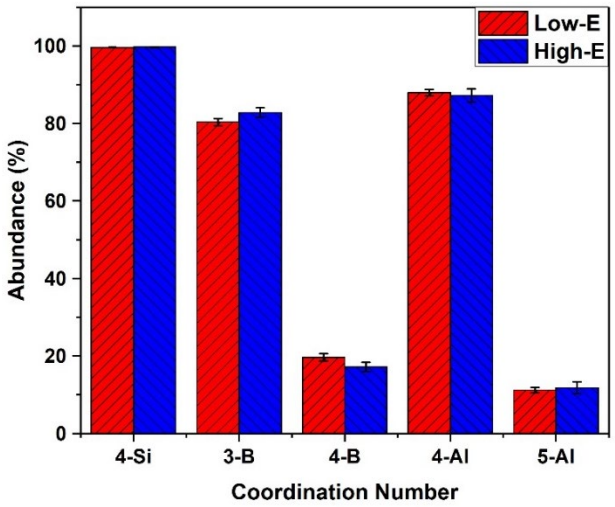

Figure 7-18. CN distribution for low- and high-E glasses.

4.3 Young's Modulus and Q_n Speciation

In this section, the low- and high-E glasses are discussed through Q_n speciation of Si and B. Figure 7-19 shows the distribution of Q_n species for 4-coordinated Si, which are differentiated in terms of low- and high-E glasses. As discussed in Section 3.3, the Si in simulated glasses were highly polymerized with Q_3 species and minor amount of Q_2 species. For low-E glasses (red), Q_3 species abundance of 12.18±1.16% is higher than 8.91±1.27% for high-E glasses (blue). Conversely, the abundance of Q_4 species of 87.36±1.30% in low-E glasses is lower than 90.79±1.36% in high-E glasses.

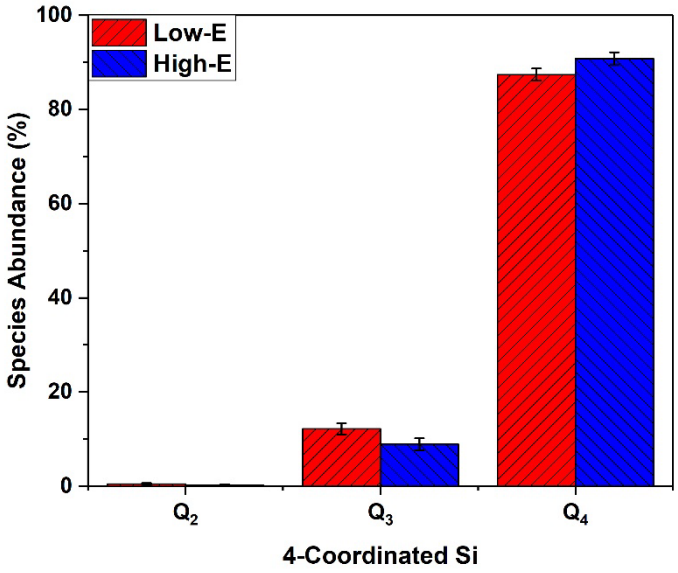

Figure 7-19. Q_n speciation of 4-coordinated silicon for low- and high-E glasses

On further discussion of polymerization of glasses, Figures 7-20 and 7-21 show that Q_n speciation of 3- and 4-coordinated B, respectively for low- and high- E glasses. In both figures, the Q_n speciation for low and high E glasses show similar behavior to that of 4-coordinated Si. In Figure 7-20, the abundance of Q_2 species for 3-coordinated B were 10.9±1.14% and 8.1±1.25% for low and high E glasses, respectively. Meanwhile, 88.77±1.19% and 91.7±1.30% of Q_3 species were calculated for low- and high-E glasses, respectively. In Figure 7-21, for 4-coordinated B the Q_3 species abundance were 4.24±1.11% and 2.8±0.69% for low- and high-E glasses, respectively, and Q_4 species

abundance were 95.74±1.10% and 97.17±0.72% for low- and high-E glasses, respectively. Additionally, the Q_n speciation of 4- and 5-coordinated Al was investigated using similar analysis. However, as discussed in Section 3.3, the Al structural units were almost entirely fully polymerized.

For low- and high-E glasses, the quantity of change among the Q_n species decreases for 4-coordinated Si, 3-coordinated B and 4-coordinated B. For example, the difference between low- and high-E glasses for 4-coordinated Si Q_4 species was 3.43%, 3-coordinated B Q_3 species was 2.92%, and 4-coordinated B Q_4 species was 1.43%. A primary reason for this behavior might be due to the ease of formation of NBO site at Si compared to 3- and 4-coordinated B, in that order. Additionally, in the simulated glasses within the compositional space studied, the Q_n speciation results indicate that a higher polymerized glass network is desirable for higher E values. These results agree with the convention that a highly polymerized glass would possibly resist more strain energy yielding a higher E. These factors should be considered in designing new PMT glasses for neutrino application.

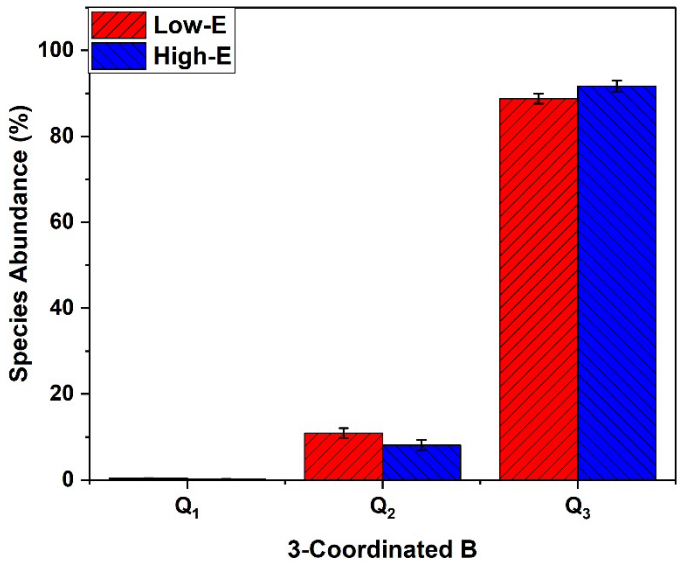

Figure 7-20. Q_n speciation of 3-coordinated B for low- and high-E glasses.

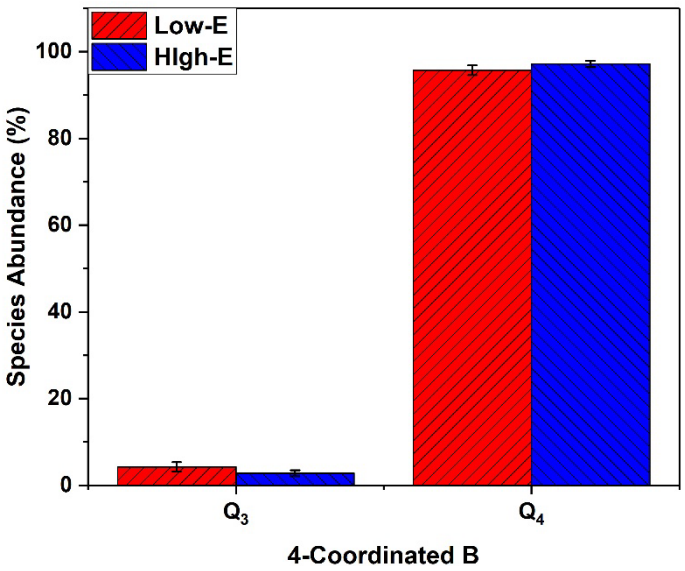

Figure 7-21. Q_n speciation of 4-coordinated B for low- and high-E glasses.

4.4 Role of Sodium

Figure 7-22 shows linear relationships of E values calculated at different pressure conditions and 300 K for the simulated glasses to the atomic percentage of Na. The correlations are shown for three different pressure conditions, initial 0.1 MPa, 1 MPa and 0.1 MPa with the R^2 values of 0.71, 0.73 and 0.61, respectively. The values of the R^2 suggests a moderate correlation, taking in consideration that the glass compositions were statistically generated. The figure shows that E decreases with higher amount of Na in the simulated glasses. This relationship remains consistent for all the simulated pressure conditions.

Figure 7-23 shows that a linear relationship exists between amount of Na and the number of NBOs calculated for the simulated glasses. The NBOs associated with B (B-NBO (black)) and Si (Si-NBO (red)) structural units along with the total amount of NBO (All-NBO (blue)) in the simulated glasses are shown. A linear regression performed for B-NBO, Si-NBO, and All-NBO concentration resulted in the coefficient of determination (R^2) of 0.71, 0.75, and 0.75, respectively. The R^2 indicates a moderate correlation between atomic concentration of Na and B-NBO, Si-NBO, and All-NBO. The total NBO content in the simulated glasses, along with the Si-NBO and B-NBO, increases with the increase of Na in the glasses within the compositional space studied. The formation of NBO in the

glasses leads to depolymerization of the glass structure resulting in a decrease of E values. As discussed in previous section, the E depends on the amount of polymerization and depolymerization of the glass.

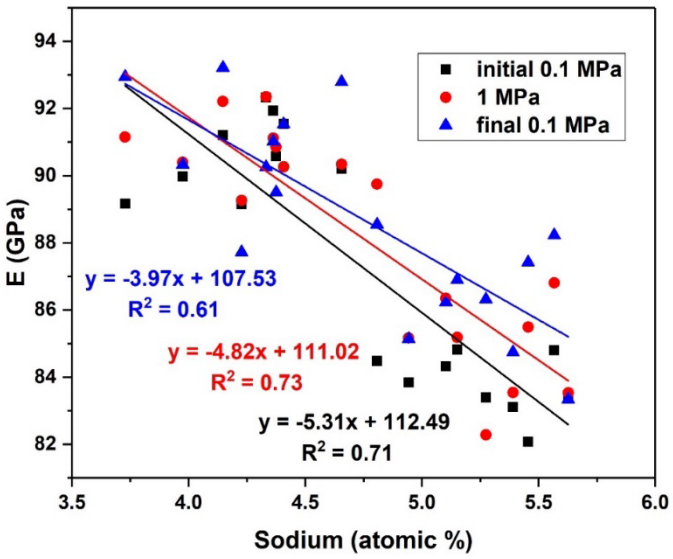

Figure 7-22. Correlation between E and atomic percentage of Na

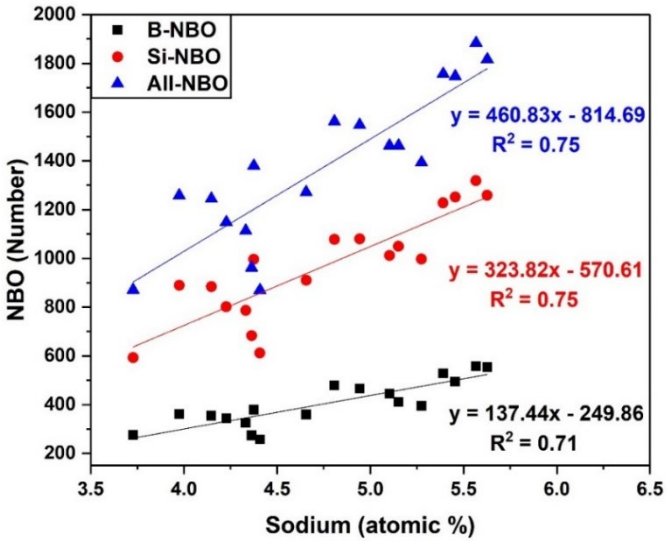

Figure 7-23. Correlation between NBO content and atomic percentage of Na

Figure 7-24 shows a linear relationship between 3- and 4-coordinated B and the atomic percentage of Na for the simulated glasses at 300 K and 0.1 MPa. The 3- and 4-coordinated B are expressed in fractional quantities. The linear regression with R^2 value of 0.75 for both 3- and 4-coordinated B suggests a reasonably good correlation between the Na concentration and 3- and 4-coodinated B atoms in the simulated glasses. The simulated glasses with higher amount of Na showed lower 3-coordinated B and higher 4-coordinated B.

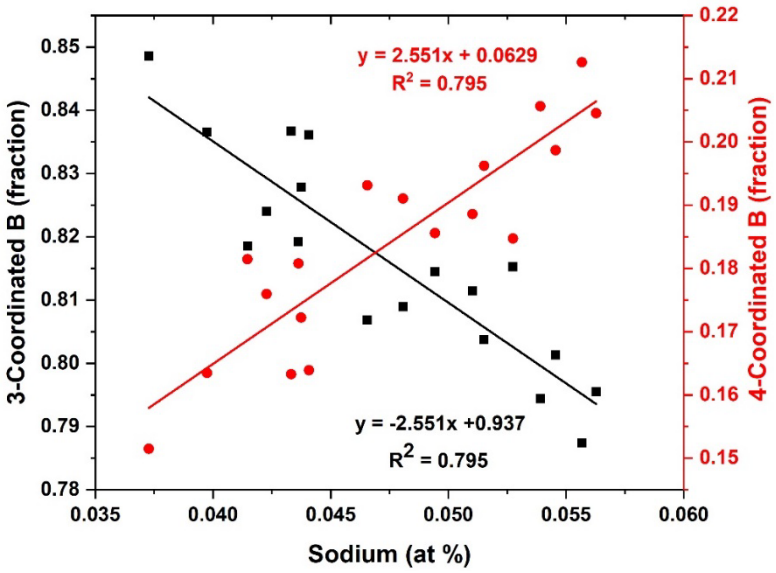

Figure 7-24. Effect of Na atoms on the coordination of B

It is known that the addition of Na in B containing glasses promotes the formation of 4-coordinated B by conversion of $[BO_3]$ to $[BO_4]^-$ structural units. The $[BO_4]^-$ unit is accompanied by a charge compensating Na ions (Na^+) for the negative charge due to an extra O bonded to B. Additionally, Na^+ acts in a charge compensating role for the formation of $[AlO_4]^-$ units in aluminoborosilicate glasses. Furthermore, Al and B compete for the charge compensating Na ions. It is known that the formation of $[AlO_4]^-$ unit is energetically more favorable than $[BO_4]^-$ unit.

Although the formation of 4-coordinated Al is energetically more favorable compared to tetrahedral B, in the simulated glasses, our results show that higher abundance of 4-coordinated B. This could be a result of Na atoms attached to B sites before complete

conversion of Al^{3+} to 4-coordinated Al, which could also explain the higher amount of 5-coordianted Al. In the simulated glasses, a higher amount of 5-coordinated Al was calculated, which could be the results of Na acting as charge compensators for $[BO_4]^-$ unit and being used to form NBOs in Si and B structural sites. The lack of alkali modifier ions for Al promotes higher coordinated Al. Additionally, alkaline earth modifier ions have been shown to favor higher coordinated Al. Even though, the simulated glasses contain both alkali and alkaline earth modifier ions, the higher concentration of Na ions compared to alkaline earths had direct influence in determining the glass structure, specially the distribution of 3- and 4-coordinated B atoms and formation of NBO.

4.5 Glass Former Connectivity

The glass former network connectivity provides information about the medium range glass structure. Figure 7-25 shows the calculated probability of possible structural unit network connections. The possible network connection between structural units are described as MO_x-NO_x, where M, N = Si, B or Al, and x represents the coordination of the glass former. The highest connection probability is that of SiO_x-SiO_x (~0.49), followed by BO_x-SiO_x (~0.31). The connection probability for BO_x-BO_x and AlO_x-SiO_x are ~0.065 and ~0.096, respectively. For BO_x-AlO_x, the probability of connection is much less ~0.035. Among all the possible network connections, AlO_x-AlO_x is the lowest with a probability ~0.0015. Additionally, the glass former network connectivity was predicted by assuming a random distribution of network former atoms, where the percentage of A-O-A or A-O-B (A/B = Si, B, Al) linkages is given by:

$$X_{A-O-A} = \frac{N_A\,(N_A - 1)}{(N_{Si} + N_B + N_{Al})(N_{Si} + N_B + N_{Al} - 1)} \tag{7.5}$$

or,

$$X_{A-O-B} = \frac{2 * N_A * N_B}{(N_{Si} + N_B + N_{Al})(N_{Si} + N_B + N_{Al} - 1)} \tag{7.6}$$

where, N_{Si}, N_B and N_{Al} are the number of Si, B and Al atoms in the simulated glasses, respectively.

In general, the glass network former connectivity calculated for the simulated glasses matches well with the predictions of a random network distribution (blue) as shown in Figure 7-25. The low occurring connectivity of BO_x-BO_x, AlO_x-SiO_x, and BO_x-AlO_x are very well predicted. Although, the calculated probability of SiO_x-SiO_x and BO_x-SiO_x were different than the predicted values, the probability trend of predicted and simulated values are matched. The result suggests a random distribution of network former atoms in the simulated glasses within the compositional space studied.

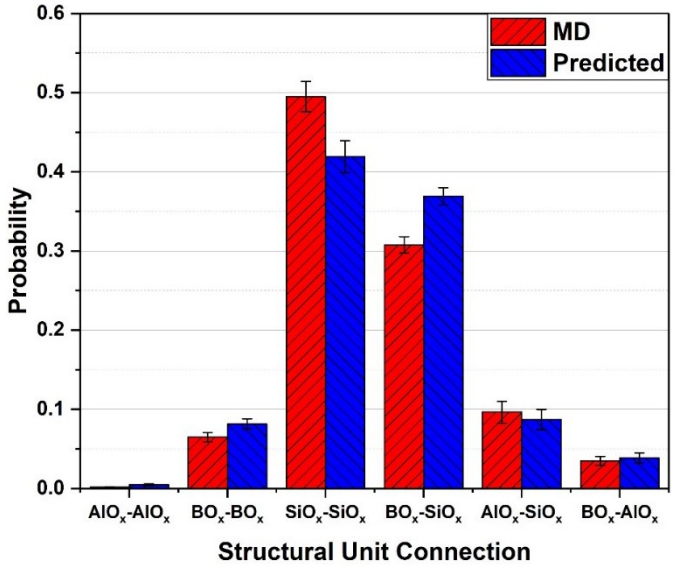

Figure 7-25. The probability of different glass former structural unit connection in the simulated glasses at 300 K and 0.1 MPa. A comparison between MD results (red) and theory value calculated by assuming a random distribution of network former atoms (blue).

5. Conclusions

The composition-structure-property of multicomponent aluminoborosilicate glasses were studied using classical MD simulation. Glass structural properties such as bond distance, coordination number (CN), Q_n speciation, BO and NBO concentrations, and E were calculated. The E value was calculated by using a linear regression of the stress-strain curve generated by uniaxial tensile simulation. The glasses were grouped in terms of low-E and high-E glasses and subjected to temperature and pressure simulations. The densities and E values calculated showed no statistically significant variations for the

glasses simulated at different temperature and pressure conditions. The bond distance for cation-oxygen and O-O species showed good agreement with previously reported values. The coordination number analysis of the simulated glasses showed that Si was found almost entirely in 4-coordination, B was observed in 3- and 4-cooridination, and Al was mostly found between 4- and 5-coordination with a small amount of 6-coordination. The average BO concentration of 93.4±0.84% suggests highly polymerized simulated glasses. The high-E glasses were composed of relatively higher BO and lower NBO abundance compared to low-E glasses. Furthermore, high-E glasses consisted of higher amount of fully polymerized glass former Q_n species for Si and B compared to low-E glasses. The polymerization of the simulated glasses was influenced by the presence of Na ions in the glasses. Glasses with higher Na concentration showed an increase in NBOs content. Additionally, higher Na concentration in the simulated glasses showed formation of higher amount of 4-coordinated B in the glasses. The polymerization of the simulated glasses was influenced by the presence of Na, which takes up multiple roles as charge compensating ions for 4-coordinated Al and B, and as network modifier ions by creating NBO sites at Si and B structural units. Our results suggest that the E values calculated for the simulated glasses within the compositional space studied depend on the polymerization of the network formers, BO, and NBO contents, and the concentration of Na in the glasses.

CHAPTER 8. SUMMARY AND CONCLUSION

In this work, experimental measurements and MD simulations were performed to investigate the structural and mechanical properties, and chemical durability of aluminoborosilicate glasses. These glasses are used in photomultiplier tube (PMT) application in water Cherenkov detector (WCD) for neutrino detection. The thesis is divided into four distinct projects.

In the first project, the mechanical property and chemical durability of commercial PMT and simplified Alfred glasses were studied using Vickers indentation, R-O-R biaxial flexural strength test, elemental ions release, XPS and WDS techinques. The Vickers hardness and R-O-R biaxial flexural strength test of two commercial PMT (Vendor1 and Vendor2) glasses showed that they had similar mechanical properties. The static mode leaching experiment showed that the glass surfaces formed dealkalized and deboronated layer. In addition, the normalized mass loss indicated pH and temperature dependent ion-release behavior of the Vendor1 glass. WDS line profile results showed dealkalized and deboronated layers, which agreed with the static mode leaching experiment. The effects of high-purity water on the R-O-R flexural strength of the glass was minor as the test measures the bulk strength of the glass.

In the second project, Gd doping of peralkaline borosilicate glasses and the Gd elemental release were studied. A maximum of 5 mol% of Gd_2O_3 doping was achieve through melt-quench technique. The ion releases study clearly indicated the Gd-ion release from powdered glasses in high-purity water at 14 ℃. Our results demonstrated that Gd-doped glass compositions could be designed in the form of beads or powders for controlled Gd-release when in contact with water, which might be added to pure water to enhance neutrino detector in the future.

In the third project, the glass structures and glass surface-water reactions of sodium aluminosilicate glass were investigated in a reactive molecular dynamics framework using a combination of Buckingham potential and reactive force field (ReaxFF) potential models. The fundamental structural properties such as bond lengths and angles showed good agreement with previously reported values, even though the ReaxFF potential was parameterized for clay-zeolite composite and water model. The surface equilibration with

ReaxFF potential resulted in a compact glass structure compared to that with Buckingham potential. This difference in the glass surface structure was correlated to the oxygen bond angle distributions between glass forming tetrahedral units (Si-O-Si and Si-O-Al). In this work, the atomic density profiles show diffusion of hydrogen atom into the glass surface, achieved through the hydrolyzation of NBO sites at the glass surface and diffusion of water molecules.

In the fourth project, the composition-structure-property of multicomponent aluminoborosilicate glasses were studied using classical MD potential. Glass structures and E values were calculated for selected glasses at different temperature and pressure conditions. The glasses were further differentiated in terms of low-E and high-E glasses and subjected to temperature and pressure simulations. The densities and Young's modulus calculated showed no statistically significant variations for the glasses simulated at different temperature and pressure conditions. The high-E glasses were composed of relatively higher BO, lower NBO abundance, and higher amount of fully polymerized glass former Q_n species for Si and B compared to low-E glasses. The polymerization of the simulated glasses was influenced by the presence of Na, which takes up multiple roles as charge compensating ions for 4-coordinated Al and B, and as network modifier ions by creating NBO sites at Si and B structural units. Our results suggest that the E values calculated for the simulated glasses within the compositional space studied, depends on the polymerization of the network formers, BO and NBO contents, and the concentration of Na in the glasses. In summary, our investigation results revealed new perspective on the structural and mechanical properties, and chemical durability of the glass studied. These results could be used to design better glass compositions for future photomultiplier tube application in water Cherenkov detectors for neutrino detection. Future work of the photomultiplier tube glasses could include investigation of glass properties in hydrostatic pressure environment, static corrosion of glasses and explore alternative compositional spaces.

CHAPTER 9. REFERENCES

1 W. Pauli, "Rapports du Septieme Conseil de Physique Solvay," *Brussels (Gauthier Villars, Paris, 1934)*, (1933). As cited in T. Kahita, *Experimental Studies of Neutrino Observations,* p. 1. World Scientific, Hackensack, NJ, 2016.

2 C. L. Cowan Jr., F. Reines, F. B. Harrision, H. W. Kruse, and A. D. McGuire, "Detection of the Free Neutrino: A Confirmation," *Science*, **124** [3212] 103–4 (1956).

3 "The Nobel Prize in Physics 2002" (2002) Nobel Media AB 2014. Accessed on: February 2018. Available at <https://www.nobelprize.org/nobel_prizes/physics/laureates/2002/>.

4 "The Nobel Prize in Physics 2015" (2015) Nobel Media AB 20142. Accessed on: February 2018. Available at <https://www.nobelprize.org/nobel_prizes/physics/laureates/2015/>.

5 E. K. Akhmedov, Neutrino Physics, Centro de F´ısica das Interac¸oes Fundamentais (CFIF), Lisboa, Portugal, 1999, Lecture Notes.

6 K. S. Hirata, T. Kajita, M. Koshiba, M. Nakahata, S. Ohara, Y. Oyama, N. Sato, A. Suzuki, et al., "Experimental Study of the Atmospheric Neutrino Flux," *Phys. Lett. B*, **205** [2–3] 416–20 (1988).

7 K. Hirata, K. Inoue, T. Ishida, T. Kajita, K. Kihara, M. Nakahata, K. Nakamura, S. Ohara, et al., "Observation of a Small Atmospheric ν_μ/ν_e Ratio in Kamiokande," *Phys. Lett. B*, **280**, 146–52 (1992).

8 R. Becker-Szendy, C. B. Bratton, D. Casper, S. T. Dye, W. Gajewski, M. Goldhaber, T. J. Haines, P. G. Halverson, et al., "Electron- and Muon-Neutrino Content of the Atmospheric Flux," *Phys. Rev. D*, **46** [9] 3720–24 (1992).

9 S. Fukuda, Y. Fukuda, T. Hayakawa, E. Ichihara, M. Ishitsuka, Y. Itow, T. Kajita, J. Kameda, et al., "The Super-Kamiokande Detector," *Nucl. Instruments Methods Phys. Res. Sect. A Accel. Spectrometers, Detect. Assoc. Equip.*, **501** [2–3] 418–62 (2003).

10 T. Kajita, "Atmospheric Neutrino Results from Super-Kamiokande and Kamiokande — Evidence for νμ Oscillations," *Nucl. Phys. B - Proc. Suppl.*, **77** [1] 123–32 (1999).

11 Y. Fukuda, T. Hayakawa, E. Ichihara, K. Inoue, K. Ishihara, H. Ishino, Y. Itow, T. Kajita, et al., "Evidence for Oscillation of Atmospheric Neutrinos," *Phys. Rev. Lett.*, **81** [8] 1562–67 (1998).

12 S. Fukuda, Y. Fukuda, M. Ishitsuka, Y. Itow, T. Kahita, J. Kameda, K. Kaneyuki,

K. Kobayashi, Y. Koshio, M. Miura, et al., “Tau Neutrinos Favored over Sterile Neutrinos in Atmospheric Muon Neutrino Oscillations,” *Phys. Rev. Lett.,* **85** [19] 3999-4003 (2000).

13 R. Oerter, *The Theory of Almost Everything: The Standard Model, the Unsung Triumph of Modern Physics*. Penguin Group, New York, 2006.

14 M. C. Gonzalez-Garcia, M. Maltoni, and T. Schwetz, “Global Analyses of Neutrino Oscillation Experiments,” *Nucl. Phys. B*, **908**, 199–217 (2016).

15 S. Choubey, “Atmospheric Neutrinos: Status and Prospects,” *Nucl. Phys. B*, **908**, 235–49 (2016).

16 T. Kajita, E. Kearns, and M. Shiozawa, “Establishing Atmospheric Neutrino Oscillations with Super-Kamiokande,” *Nucl. Phys. B*, **908**, 14–29 (2016).

17 M. H. Ahn, H. Aliu, A. Andringa, S. Aoki, Y. Aoyama, J. Argyriades, K. Asakura, R. Ashie, et al., “Measurement of Neutrino Oscillation by the K2K Experiment,” *Phys. Rev. D*, **74** [72003] 1–40 (2006).

18 P. Adamson, I. Anghel, C. Backhouse, G. Barr, M. Bishai, A. Blake, G. J. Bock, D. Bogert, et al., “Measurement of Neutrino and Antineutrino Oscillations Using Beam and Atmospheric Data in MINOS,” *Phys. Rev. Lett.*, **110** [25] 1–6 (2013).

19 K. Abe, J. Adam, H. Aihara, T. Akiri, C. Andreopoulos, S. Aoki, A. Ariga, S. Assylbekov, et al., “Neutrino Oscillation Physics Potential of the T2K Experiment,” *Prog. Theor. Exp. Phys.*, **2015** [4] 1–112 (2015).

20 K. Abe, N. Abgrall, H. Aihara, Y. Ajima, J. B. Albert, D. Allan, P. A. Amaudruz, C. Andreopoulos, et al., “The T2K Experiment,” *Nucl. Instruments Methods Phys. Res. Sect. A Accel. Spectrometers, Detect. Assoc. Equip.*, **659** [1] 106–35 (2011).

21 K. Abe, Y. Hayato, T. Iida, M. Ikeda, J. Kameda, Y. Koshio, A. Minamino, M. Miura, et al., “Search for Matter-Dependent Atmospheric Neutrino Oscillations in Super-Kamiokande,” *Phys. Rev. D*, **77** [52001] 1–6 (2008).

22 K. K. Shiraishi, “Super-Kamiokande Atmospheric Neutrino Analysis of Matter-Dependent Neutrino Oscillation Models”; Ph.D. Thesis. University of Washington, Seattle, WA, 2006.

23 G. Mitsuka, K. Abe, Y. Hayato, T. Iida, M. Ikeda, J. Kameda, Y. Koshio, M. Miura, et al., “Study of Non-Standard Neutrino Interactions with Atmospheric Neutrino Data in Super-Kamiokande I and II,” *Phys. Rev. D*, **84** [113008] 1–12 (2011).

24 K. Abe, Y. Haga, Y. Hayato, M. Ikeda, K. Iyogi, J. Kameda, Y. Kishimoto, M. Miura, et al., “Test of Lorentz Invariance with Atmospheric Neutrinos,” *Phys. Rev. D - Part. Fields, Gravit. Cosmol.*, **91** [5] 1–17 (2015).

25 A. Aguilar, L. B. Auerbach, R. L. Burman, D. O. Caldwell, E. D. Church, A. K. Cochran, J. B. Donahue, A. Fazely, et al., "Evidence for Neutrino Oscillations from the Observation of Electron Anti-Neutrinos in A Muon Anti-Neutrino Beam," *Phys. Rev. D*, **64**, 1–22 (2001).

26 J. N. Abdurashitov, V. N. Gavrin, V. V. Gorbachev, P. P. Gurkina, T. V. Ibragimova, A. V. Kalikhov, N. G. Khairnasov, T. V. Knodel, et al., "Measurement of the Solar Neutrino Capture Rate with Gallium Metal. III. Results for the 2002-2007 Data-Taking Period," *Phys. Rev. C*, **80** [1] 1–16 (2009).

27 S. W. Barwick, J. J. Beatty, D. Z. Besson, W. R. Binns, B. Cai, J. M. Clem, A. Connolly, D. F. Cowen, et al., "Constraints on Cosmic Neutrino Fluxes from the Antarctic Impulsive Transient Antenna Experiment," *Phys. Rev. Lett.*, **96** [17] 1–4 (2006).

28 D. G. Michael, P. Adamson, T. Alexopoulos, W. W. M. Allison, G. J. Alner, K. Anderson, C. Andreopoulos, M. Andrews, et al., "Observation of Muon Neutrino Disappearance with the MINOS Detectors in the NuMI Neutrino Beam," *Phys. Rev. Lett.*, **97** [19] 1–6 (2006).

29 D. Akimov, J. B. Albert, P. An, C. Awe, P. S. Barbeau, B. Becker, V. Belov, A. Brown, et al., "Observation of Coherent Elastic Neutrino-Nucleus Scattering," *Science*, **357** [6356] 1123–26 (2017).

30 G. Battistoni, A. Ferrari, T. Montaruli, and P. R. Sala, "High Energy Extension of the FLUKA Atmospheric Neutrino Flux;" p. 10 in *Proc. 28th Int. Cosm. Ray Conf. 2003*, Universal Academy Press, Tokyo, 2004.

31 G. D. Barr, T. K. Gaisser, P. Lipari, S. Robbins, and T. Stanev, "Three-Dimensional Calculation of Atmospheric Neutrinos," *Phys. Rev. D*, **70** [2] 1–24 (2004).

32 M. Honda, T. Kajita, K. Kasahara, and S. Midorikawa, "New Calculation of the Atmospheric Neutrino Flux in a Three-Dimensional Scheme," *Phys. Rev. D*, **70** [4 A] 1–31 (2004).

33 M. Honda, T. Kajita, K. Kasahara, and S. Midorikawa, "Calculation of the Flux of Atmospheric Neutrinos," *Phys. Rev. D*, **52** [9] 4985–5005 (1995).

34 M. Honda, K. Kasahara, K. Hidaka, and S. Midorikawa, "Atmospheric Neutrino Fluxes," *Phys. Lett. B*, **248** [1] 193–98 (1990).

35 R. Becker-Szendy, R. M. Bionta, C. B. Bratton, D. Casper, R. Claus, B. Cortez, S. T. Dye, S. Errede, et al., "IMB-3: A Large Water Cherenkov Detector for Nucleon Decay and Neutrino Interactions," *Nucl. Inst. Methods Phys. Res. A*, **324** [1–2] 363–82 (1993).

36 M. Koshiba, "Observational Neutrino Astrophysics," *Phys. Rep.*, **220** [5] 229–381 (1992).

37 A. Bellerive, J. R. Klein, A. B. McDonald, A. J. Noble, and A. W. P. Poon, "The Sudbury Neutrino Observatory," *Nucl. Phys. B*, **908** [June] 30–51 (2016).

38 T. Nakaya, S. Hirota, K. Huang, A. K. Ichikawa, M. Ikeda, A. Minamino, E. Kearns, J. L. Stone, et al., "Hyper-Kamiokande Physics Opportunities" (2013). Accessed on: January 2018. Available at: <https://arxiv.org/abs/1309.0184 >.

39 S. Ahmed, M. S. Athar, R. Hasan, M. Salim, S. K. Singh, S. S. R. Inbanathan, V. Singh, V. S. Subrahmanyam, et al., "Physics Potential of the ICAL Detector at the India-Based Neutrino Observatory (INO)," *J. Phys.*, **88** [5] (2017).

40 M. G. Aartsen, M. Ackermann, J. Adams, J. A. Aguilar, M. Ahlers, I. Al Smarai, D. Altmann, K. Andeen, et al., "Letter of Intent: The Precision Icecube Next Generation Upgrade (PINGU)," *Proc. Sci.*, **11**–**15**–**Marc**, (2014).

41 S. Adrián-Martínez, M. Ageron, F. Aharonian, S. Aiello, A. Albert, F. Ameli, E. Anassontzis, M. Andre, et al., "Letter of Intent for ARCA and ORCA," *J. Phys. G Nucl. Part. Phys.*, **43** [8] 1–119 (2016).

42 Y.-F. Li, "Jiangmen Underground Neutrino Observatory: Status and Prospectives," *Part. Phys. Year Light*, [August] 27–33 (2017).

43 A. Suzuki, M. Mori, K. Kaneyuki, T. Tanimori, J. Takeuchi, H. Kyushima, and Y. Ohashi, "Improvement of 20-inch Diameter Photomultiplier Tubes," *Nucl. Instruments Methods Phys. Res. Sect. A Accel. Spectrometers, Detect. Assoc. Equip.*, **329**, 299–313 (1993).

44 Y. Koshio, "Study of Solar Neutrinos at Super Kamiokande"; Ph.D. Thesis, University of Tokyo, Tokyo, Japan, 1998.

45 C. Yanagisawa and T. Kato, *Report on the Super-Kamiokande Accident*. 2001.

46 W. H. Zachariasen, "The Atomic Arrangement in Glass," *J. Am. Ceram. Soc.*, **54**, 3841–51 (1932).

47 W. J. Dell and P. J. Bray, "^{11}B NMR Studies and Structural Modeling of Na_2O-B_2O_3-SiO_2 Glasses of High Soda Content," *J. Non. Cryst. Solids*, **58**, 1–16 (1983).

48 Y. H. Yun and P. J. Bray, "Nuclear Magnetic Resonance Studies of the Glasses in the System Na_2O-B_2O_3-SiO_2," *J. Non. Cryst. Solids*, **27** [3] 363–80 (1978).

49 R. J. Araujo, "Statistical Mechanical Model of Boron Coordination," *J. Non. Cryst. Solids*, **42** [1] 209–29 (1980).

50 T. Abe, "Borosilicate Glasses," *J. Am. Ceram. Soc.*, **35** [11] 284–99 (1952).

51 S. Wang and J. F. Stebbins, "Multiple-Quantum Magic-Angle Spinning ^{17}O NMR Studies of Borate, Borosilicate, and Boroaluminate Glasses," *J. Am. Ceram. Soc.*,

82 [6] 1519–28 (1999).

52 T. J. Kiczenski, L. S. Du, and J. Stebbins, "The Effect of Fictive Temperature on the Structure of E-Glass: A High Resolution, Multinuclear NMR Study," *J. Non. Cryst. Solids*, **351** [46–48] 3571–78 (2005).

53 S. Sen, Z. Xu, and J. F. Stebbins, "Temperature Dependent Structural Changes in Borate, Borosilicate and Boroaluminate Liquids: High-Resolution ^{11}B, ^{29}Si and ^{27}Al NMR Studies," *J. Non. Cryst. Solids*, **226** [1–2] 29–40 (1998).

54 L. S. Du and J. F. Stebbins, "Network Connectivity in Aluminoborosilicate Glasses: A High-Resolution ^{11}B, ^{27}Al and ^{17}O NMR Study," *J. Non. Cryst. Solids*, **351** [43–45] 3508–20 (2005).

55 W. F. Du, K. Kuraoka, T. Akai, and T. Yazawa, "Study of Al_2O_3 Effect on Structural Change and Phase Separation in Na_2O-B_2O_3-SiO_2 Glass by NMR," *J. Mater. Sci.*, **35** [19] 4865-4871 (2000).

56 J. J. De Yoreo, A. Navrotsky, and D. B. Dingwell, "Energetics of the Charge-Coupled Substitution $Si^{4+} \rightarrow Na^{+} + T^{3+}$ in the-Glasses $NaTO_2$–SiO_2 (T = Al, Fe, Ga, B)," *J. Am. Ceram. Soc.*, **73** [7] 2068–72 (1990).

57 J. Wu and J. F. Stebbins, "Effects of Cation Field Strength on the Structure of Aluminoborosilicate Glasses: High-Resolution ^{11}B, ^{27}Al and ^{23}Na MAS NMR," *J. Non. Cryst. Solids*, **355** [9] 556–62 (2009).

58 A. Tandia, M. Reveil, K. D. Vargheese, J. Luo, J. C. Mauro, and P. Clancy, "Modeling the Thermal Poling of Glasses Using Molecular Dynamics. Part 1: Effects on Glass Structure," *J. Non. Cryst. Solids*, **461**, 98–103 (2017).

59 M. Reveil, A. Tandia, J. Luo, K. D. Vargheese, S. Goyal, J. C. Mauro, and P. Clancy, "Modeling the Thermal Poling of Glasses Using Molecular Dynamics. Part 2: Effects on Elastic Properties," *J. Non. Cryst. Solids*, **468**, 17–26 (2017).

60 L. Verlet, "Computer 'Experiments' on Classical Fluids. I. Thermodynamical Properties of Lennard-Jones Molecules," *Phys. Rev.*, **159** [1] 98–103 (1967).

61 W. C. Swope, H. C. Andersen, P. H. Berens, and K. R. Wilson, "A Computer Simulation Method for the Calculation of Equilibrium Constants for the Formation of Physical Clusters of Molecules: Application to Small Water Clusters," *J. Chem. Phys.*, **76** [1] 637–49 (1982).

62 A. Pedone, G. Malavasi, M. C. Menziani, A. N. Cormack, and U. Segre, "A New Self-Consistent Empirical Interatomic Potential Model for Oxides, Silicates, and Silicas-Based Glasses," *J. Phys. Chem. B*, **110** [24] 11780–95 (2006).

63 A. N. Cormack, Alfred University, Alfred, NY, 2013, Private Communication.

64 A. N. Cormack, J. Du, and T. R. Zeitler, "Sodium Ion Migration Mechanisms in Silicate Glasses Probed by Molecular Dynamics Simulations," *J. Non. Cryst. Solids*, **323** [1–3] 147–54 (2003).

65 A. C. T. van Duin, S. Dasgupta, F. Lorant, and W. A. Goddard III, "ReaxFF: A Reactive Force Field for Hydrocarbons," *J. Phys. Chem. A*, **105** [41] 9396–9409 (2001).

66 A. K. Rappe and W. A. Goddard III, "Charge Equilibration for Molecular Dynamics Simulations," *J. Phys. Chem.*, **95** [8340] 3358–63 (1991).

67 "Standard Test Methods for Determining Chemical Durability of Nuclear, Hazardous, and Mized Waste, Glasses: The Product Consistency Test (PCT)," ASTM Designation C 1285-97. American Society of Testing and Materials International, West Conshohocken, PA, 1997.

68 H. Scholze, "Chemical Durability of Glasses," *J. Non. Cryst. Solids*, **52** [1–3] 91–103 (1982).

69 F. Angeli, T. Charpentier, S. Gin, and J. C. Petit, "^{17}O 3Q-MAS NMR Characterization of a Sodium Aluminoborosilicate Glass and Its Alteration Gel," *Chem. Phys. Lett.*, **341** [1–2] 23–28 (2001).

70 G. El-Damrawi, W. Muller-Warmuth, H. Doweidar, and I. Gohar, "^{11}B, ^{29}Si and ^{27}Al Nuclear Magnetic Resonance Studies of Na_2O-Al_2O_3-B_2O_3-SiO_2 Glasses," *Phys. Chem. Glass*, **35** [2] 52–57 (1993).

71 G. Della Mea, A. Gasparotto, M. Bettinelli, A. Montenero, and R. Scaglioni, "Chemical Durability of Zinc-Containing Glasses," *J. Non. Cryst. Solids*, **84**, 443–51 (1986).

72 G. Calestani, A. Montenero, E. Ferraguti, G. Ingletto, and M. Bettinelli, "Influence of Some Oxides on the Durability of a Borosilicate Glass," *J. Non. Cryst. Solids*, **84**, 452–62 (1986).

73 J. F. Beacom and M. R. Vagins, "Antineutrino Spectroscopy with Large Water Čerenkov Detectors," *Phys. Rev. Lett.*, **93** [17] 20–23 (2004).

74 G. Bellini, J. Benziger, S. Bonetti, M. B. Avanzini, B. Caccianiga, L. Cadonati, F. Calaprice, C. Carraro, et al., "Observation of Geo-Neutrinos," *Phys. Lett. Sect. B*, **687** [4–5] 299–304 (2010).

75 "Search for Supernova Relic Neutrinos" (2015). Accessed on: February 2018. Available at <http://www-sk.icrr.u-tokyo.ac.jp/sk/physics/srn-e.html>.

76 M. R. Vagins, "GADZOOKS! The Future of Super-Kamiokande?," *Nucl. Phys. B (Proc. Suppl.)*, **168**, 128–30 (2007).

77 L. M. Margo, “EGADS Progress;” pp. 3–6 in *33rd International Cosmic Ray Conference (ICRC 2013): The Astroparticle Physics Conference*, Curran Associates, Red Hook, NY, 2015.

78 A. Kibayashi, “Gadolinium Study for a Water Cherenkov Detector” pp. 4–7 in *Proceeding of Division of Particles and Fields (DPF)-2009 Conference*, (2009). Accessed on: February 2018. Available at < https://arxiv.org/abs/0909.5528 >.

79 W. Coleman, A. Bernstein, S. Dazeley, and R. Svoboda, “Transparency of 0.2% $GdCl_3$ Doped Water in a Stainless Steel Test Environment,” *Nucl. Instruments Methods Phys. Res. Sect. A Accel. Spectrometers, Detect. Assoc. Equip.*, **595** [2] 339–45 (2008).

80 W. F. Coleman, “Testing of GdCl3 Doping in Water Cherenkov Antineutrino Detectors”; Ph.D. Thesis. Louisiana State University, Baton Rouge, LA, 2009.

81 H. Watanabe, H. Zhang, K. Abe, Y. Hayato, T. Iida, M. Ikeda, J. Kameda, K. Kobayashi, et al., “First Study of Neutron Tagging with a Water Cherenkov Detector,” *Astropart. Phys.*, **31** [4] 320–28 (2009).

82 I. Anghel, J. F. Beacom, M. Bergevin, G. Davies, F. Di Lodovico, A. Elagin, H. Frisch, R. Hill, et al., “Expression of Interest: The Atmospheric Neutrino Neutron Interaction Experiment (ANNIE)” (2014). Accessed on: January 2018. Available at < https://arxiv.org/abs/1402.6411>.

83 I. Anghel, J. F. Beacom, M. Bergevin, C. Blanco, F. Di Lodovico, A. Elagin, H. Frisch, J. Griskevich, et al., “Letter of Intent: The Accelerator Neutrino Neutron Interaction Experiment (ANNIE)” (2014). Accessed on: February 2018. Available at < https://arxiv.org/abs/1504.01480>.

84 T. Mori, “R&D Project for Gd-Doped Water Cherenkov Detector,” *J. Phys. Conf. Ser.*, **408**, 12077 (2013).

85 A. Renshaw, “Research and Development for a Gadolinium Doped Water Cherenkov Detector,” *Phys. Procedia*, **37** [0] 1249–56 (2012).

86 R. Laha and J. F. Beacom, “Gadolinium in Water Cherenkov Detectors Improves Detection of Supernova,” *Phys. Rev. D - Part. Fields, Gravit. Cosmol.*, **89** [6] 1–10 (2014).

87 H. Sekiya, “Low Energy Neutrinos in Super-Kamiokande,” *J. Phys. Conf. Ser.*, **718**, 1–5 (2016).

88 T. Advocat, J. L. Crovisier, E. Vernaz, G. Ehret, and H. Charpentier, “Hydrolysis of R7T7 Nuclear Waste Glass in Dilute Media: Mechanisms and Rate as a Function of pH;” in *Sci. Basis Nucl. Waste Manag. XIV*, Boston, MA, 1990.

89 B. P. McGrail, W. L. Ebert, A. J. Bakel, and D. K. Peeler, “Measurement of Kinetic

Rate Law Parameters on a Na-Ca-Al Borosilicate Glass for Low-Activity Waste," *J. Nucl. Mater.*, **249**, 175–89 (1997).

90 A. Tournié, P. Ricciardi, and P. Colomban, "Glass Corrosion Mechanisms: A Multiscale Analysis," *Solid State Ionics*, **179** [38] 2142–54 (2008).

91 T. Geisler, T. Nagel, M. R. Kilburn, A. Janssen, J. P. Icenhower, R. O. C. Fonseca, M. Grange, and A. A. Nemchin, "The Mechanism of Borosilicate Glass Corrosion Revisited," *Geochim. Cosmochim. Acta*, **158**, 112–29 (2015).

92 T. Geisler, A. Janssen, D. Scheiter, T. Stephan, J. Berndt, and A. Putnis, "Aqueous Corrosion of Borosilicate Glass Under Acidic Conditions: A New Corrosion Mechanism," *J. Non. Cryst. Solids*, **356** [28–30] 1458–65 (2010).

93 C. F. Drake and W. M. Allen, "The Use of Controlled-Release Glass for the Controlled Delivery of Bioactive Materials," *Biochem. Soc. Trans.*, **13** [2] 516–20 (1985).

94 D. V. Lenihan, A. J. Carter, T. Gilchrist, D. M. Healy, I. A. Miller, L. M. Myles, and M. A. Glasby, "Biodegradable Controlled Release Glass in the Repair of Peripheral Nerve Injuries," *J. Hand Surg. Am.*, **23** [5] 588–93 (1998).

95 R. A. Siegel and M. J. Rathbone, "Part I: The Value of Drug Delivery, Chapter 2: Overview of Controlled Release Mechanisms;" pp. 19–43 in *Fundamentals and Applications of Controlled Release Drug Delivery*. Edited by J. Siepmann, R.A. Siegel and M.J. Rathbone. Springer, New York, NY, 2012.

96 P. Nooeaid, W. Li, J. A. Roether, V. Mourino, O.-M. Goudouri, D. W. Schubert, and A. R. Boccaccini, "Development of Bioactive Glass Based Scaffolds for Controlled Antibiotic Release in Bone Tissue Engineering via Biodegradable Polymer Layered Coating," *Biointerphases*, **9** [4] 41001 (2014).

97 Y. Li, Y. Z. Liu, T. Long, X. Bin Yu, T. T. Tang, K. R. Dai, B. Tian, Y. P. Guo, and Z. A. Zhu, "Mesoporous Bioactive Glass as a Drug Delivery System: Fabrication, Bactericidal Properties and Biocompatibility," *J. Mater. Sci. Mater. Med.*, **24** [8] 1951–61 (2013).

98 L. Li, H. Li, M. Qian, and D. M. Strachan, "Gadolinium Solubility in Peralkaline Borosilicate Glasses," *J. Non. Cryst. Solids*, **283** [1–3] 237–45 (2001).

99 A. I. Priven, "General Method for Calculating the Properties of Oxide Glasses and Glass Forming Melts from Their Composition and Temperature," *Glass Technol.*, **45** [6] 244–54 (2004).

100 P. K. Abraitis, F. R. Livens, J. E. Monteith, J. S. Small, D. P. Trivedi, D. J. Vaughan, and R. A. Wogelius, "The Kinetics and Mechanisms of Simulated British Magnox Waste Glass Dissolution as a Function of pH, Silicic Acid Activity and Time in Low Temperature Aqueous Systems," *Appl. Geochem.*, **15** [9] 1399–1416 (2000).

101 B. Grambow and R. Müller, "First-Order Dissolution Rate Law and the Role of Surface Layers in Glass Performance Assessment," *J. Nucl. Mater.*, **298** [1–2] 112–24 (2001).

102 P. Aagaard and H. C. Helgeson, "Thermodynamic and Kinetic Constraints on Reaction Rates Among Minerals and Aqueous Solutions. I. Theoretical Considerations," *Am. J. Sci.*, **282** [3] 237–85 (1982).

103 B. C. Bunker, "Molecular Mechanisms for Corrosion of Silica and Silicate Glasses," *J. Non. Cryst. Solids*, **179** [1] 300–308 (1994).

104 B. P. McGrail, J. P. Icenhower, D. K. Shuh, P. Liu, J. G. Darab, D. R. Baer, S. Thevuthasen, V. Shutthanandan, M. H. Engelhard, C. H. Booth, and P. Nachimuthu, "The Structure of Na_2O-Al_2O_3-SiO_2 Glass: Impact on Sodium Ion Exchange in H_2O and D_2O," *J. Non. Cryst. Solids*, **296**, 10–26 (2001).

105 B. C. Bunker, T. J. Headley, and S. C. Douglas, "Gel Structures in Leached Alkali Silicate Glass," *MRS Proc.*, **32**, 41–46 (1984).

106 P. Frugier, S. Gin, Y. Minet, T. Chave, B. Bonin, N. Godon, J. E. Lartigue, P. Jollivet, A. Ayral, L. De Windt, and G. Santarini, "SON68 Nuclear Glass Dissolution Kinetics: Current State of Knowledge and Basis of the New GRAAL Model," *J. Nucl. Mater.*, **380**, 8–21 (2008).

107 C. Guittonneau, N. Godon, D. Ne, D. Rebiscoul, M. Cabi, S. Gin, C. Guittonneau, N. Godon, et al., "Nuclear Glass Durability: New Insight into Alteration Layer Properties," *J. Phys. Chem. C*, **115** [38] 18696–706 (2011).

108 S. Gin, J. V. Ryan, D. K. Schreiber, J. Neeway, and M. Cabié, "Contribution of Atom-Probe Tomography to a Better Understanding of Glass Alteration Mechanisms: Application to a Nuclear Glass Specimen Altered 25 Years in a Granitic Environment," *Chem. Geol.*, **349**–**350**, 99–109 (2013).

109 C. Jégou, S. Gin, and F. Larché, "Alteration Kinetics of a Simplified Nuclear Glass in an Aqueous Medium: Effects of Solution Chemistry and of Protective Gel Properties on Diminishing the Alteration Rate," *J. Nucl. Mater.*, **280** [2] 216–29 (2000).

110 S. Block and E. M. Levin, "Structural Interpretation of Immiscibility in Oxide Systems: II, Coordination Principles Applied to Immiscibility," *J. Am. Ceram. Soc.*, **40** [4] 113–18 (1957).

111 E. Levin and S. Block, "Structural Interpretation of Immiscibility in Oxide Systems: I, Analysis and Calculation of Immiscibility," *J. Am. Ceram. Soc.*, **40** [3] 95–106 (1957).

112 H. Li, Y. Su, L. Li, and D. M. Strachan, "Raman Spectroscopic Study of Gadolinium(III) in Sodium-Aluminoborosilicate Glasses," *J. Non. Cryst. Solids*,

292, 167–76 (2001).

113 R. K. Brow and D. R. Tallant, "Structural Design of Sealing Glasses," *J. Non. Cryst. Solids*, **222**, 396–406 (1997).

114 I. N. Chakraborty, H. L. Rutz, and D. E. Day, "Glass Formation, Properties and Structure of Y_2O_3-Al_2O_3-B_2O_3 Glasses," *J. Non. Cryst. Solids*, **84**, 86–92 (1986).

115 K. Terashima, S. Tamura, S.-H. Kim, and T. Yoko, "Structure and Nonlinear Optical Properties of Lanthanide Borate Glasses," *J. Am. Ceram. Soc.*, **80**, 2903–9 (1997).

116 R. K. Brow, D. R. Tallant, and G. L. Turner, "Raman and ^{11}B Nuclear Magnetic Resonance Spectroscopic Studies of Alkaline-Earth Lanthanoborate Glasses," *J. Am. Ceram. Soc.*, **79** [9] 2410–16 (1996).

117 R. K. Brow and D. R. Tallant, "Polyhedral Arrangements in Lanthanum Aluminoborate Glasses," *J. Am. Ceram. Soc.*, **80** [5] 1239–44 (1997).

118 L. Wondraczek, J. C. Mauro, J. Eckert, U. Kühn, J. Horbach, J. Deubener, and T. Rouxel, "Towards Ultrastrong Glasses," *Adv. Mater.*, **23** [39] 4578–86 (2011).

119 C. M. Jantzen and M. J. Plodinec, "Thermodynamic Model of Natural, Medieval and Nuclear Waste Glass Durability," *J. Non. Cryst. Solids*, **67**, 207–23 (1984).

120 C. M. Jantzen, K. G. Brown, and J. B. Pickett, "Durable Glass for Thousands of Years," *Int. J. Appl. Glass Sci.*, **1** [1] 38–62 (2010).

121 R. Dongol and K. Sundaram, "Release of Gd-ions from Peralkaline Borosilicate Glass in Pure Water for Neutrino Detection in Water-Cherenkov Detectors," *J. Instrum.*, **12**, 1–7 (2017).

122 R. Dongol and S. K. Sundaram, "Chemical Durability and Mechanical Properties of Aluminoborosilicate Glasses for Water Cherenkov Neutrino Detection," *Glass Technol. Eur. J. Glass Sci. Technol. Part A*, **58** [5] 145–55 (2017).

123 R. Dongol, K. Chambliss, and S. K. Sundaram, "Mechanical Properties of Photomultiplier Tube Glasses for Neutrino Detection," *Int. J. Appl. Glass Sci.*, **7** [1] 94–103 (2016).

124 V. Shutthanandan, D. R. Baer, S. Thevuthasan, E. M. Adams, S. Maheswaran, M. H. Engelhard, J. P. Icenhower, and B. P. McGrail, "High Energy Ion Beam Studies of Ion Exchange in a Na_2O-Al_2O_3-SiO_2 Glass," *J. Appl. Phys.*, **91** [4] 1910–20 (2002).

125 C. Mischler, W. Kob, and K. Binder, "Classical and Ab-Initio Molecular Dynamic Simulation of an Amorphous Silica Surface," *Comput. Phys. Commun.*, **147**, 222–25 (2002).

126 M. Du, A. Kolchin, H. Cheng, M. Du, A. Kolchin, and H. Cheng, "Hydrolysis of a Two-Membered Silica Ring on the Amorphous Silica Surface," *J. Chem. Phys.*, **120** [2] 1044–54 (2004).

127 J. M. Rimsza, J. Yeon, A. C. T. Van Duin, and J. Du, "Water Interactions with Nanoporous Silica: Comparison of ReaxFF and Ab Initio Based Molecular Dynamics Simulations," *J. Phys. Chem. C*, **120** [43] 24803–16 (2016).

128 S. H. Garofalini, "Molecular Dynamics Computer Simulations of Silica Surface Structure and Adsorption of Water Molecules," *J. Non. Cryst. Solids*, **120**, 1–12 (1990).

129 D. M. Zirl and S. H. Garofalini, "Structure of Sodium Aluminosilicate Glasses," *J. Am. Ceram. Soc.*, **73** [10] 2848–56 (1990).

130 E. A. Leed and C. G. Pantano, "Computer Modeling of Water Adsorption on Silica and Silicate Glass Fracture Surfaces," *J. Non. Cryst. Solids*, **325**, 48–60 (2003).

131 J. Du and A. N. Cormack, "Molecular Dynamics Simulation of the Structure and Hydroxylation of Silica Glass Surfaces," *J. Am. Ceram. Soc.*, **88** [9] 2532–39 (2005).

132 T. S. Mahadevan and S. H. Garofalini, "Dissociative Chemisorption of Water onto Silica Surfaces and Formation of Hydronium Ions," *J. Phys. Chem.*, **112**, 1507–15 (2008).

133 Y. Xiang, J. Du, M. M. Smedskjaer, and J. C. Mauro, "Structure and Properties of Sodium Aluminosilicate Glasses from Molecular Dynamics Simulations," *J. Chem. Phys.*, **139** [4] 44507 (2013).

134 J. Puibasser and R. J.-M. Pellenq, "A Comparison of Water Adsorption ofn Ordered and Disordered Silica Substrates," *Phys. Chem. Chem. Phys.*, **6** [8] 1933–37 (2004).

135 P. Demontis, G. Stara, G. B. Suffritti, D. Chimica, and V. Uni, "Behavior of Water in the Hydrophobic Zeolite Silicalite at Different Temperatures. A Molecular Dynamics Study," *J. Phys. Chem. B*, **107**, 4426–36 (2003).

136 G. C. Abell, "Empirical Chemical Pseudopotential Theory of Molecular and Metallic Bonding," *Phys. Rev. B*, **31** [10] 6184–96 (1985).

137 J. Tersoff, "New Empirical Approach for the Structure and Energy of Covalent Systems," *Phys. Rev. B*, **37** [12] 6991–7000 (1988).

138 D. Brenner, "Empirical Potential for Hydrocarbons for use in Simulating the Chemical Vapor Deposition of Diamond Films," *Phys. Rev. B*, **42** [15] 9458–71 (1990).

139 D. G. Pettifor, I. I. Oleinik, and F. Abel, "Analytic Bond-Order Potentials Beyond Tersoff-Brenner. I. Theory," *Phys. Rev. B*, **59** [13] 8487–99 (1999).

140 S. J. Stuart, A. B. Tutein, and J. A. Harrison, "A Reactive Potential for Hydrocarbons with Intermolecular Interactions," *J. Chem. Phys.*, **112** [14] 6472–86 (2000).

141 D. Raymand, A. C. T. van Duin, M. Baudin, and K. Hermansson, "A Reactive Force Field (ReaxFF) for Zinc Oxide," *Surf. Sci.*, **602** [5] 1020–31 (2008).

142 D. Raymand, A. C. T. van Duin, D. Spångberg, W. A. Goddard, and K. Hermansson, "Water Adsorption on Stepped ZnO Surfaces from MD Simulation," *Surf. Sci.*, **604**, 741–52 (2010).

143 M. F. Russo, R. Li, M. Mench, and A. C. T. Van Duin, "Molecular Dynamic Simulation of Aluminum-Water Reactions Using the ReaxFF Reactive Force Field," *Int. J. Hydrogen Energy*, **36** [10] 5828–35 (2011).

144 M. C. Pitman and A. C. T. Van Duin, "Dynamics of Confined Reactive Water in Smectite Clay-Zeolite Composites," *J. Am. Chem. Soc.*, **134** [6] 3042–53 (2012).

145 A. C. T. Van Duin, A. Strachan, S. Stewman, Q. Zhang, X. Xu, and W. A. Goddard III, "Reactive Force Field for Silicon and Silicon Oxide Systems," *J. Phys. Chem. A*, **107** [19] 3803–3811 (2003).

146 Y. Yu, B. Wang, M. Wang, G. Sant, and M. Bauchy, "Revisiting Silica with ReaxFF: Towards Improved Predictions of Glass Structure and Properties via Reactive Molecular Dynamics," *J. Non. Cryst. Solids*, **443**, 148–54 (2016).

147 Y. Yu, B. Wang, M. Wang, and M. Bauchy, "Reactive Molecular Dynamics Simulations of Sodium Silicate Glasses — Toward an Improved Understanding of the Structure," *Int. J. Appl. Glass Sci.*, **10**, 1–10 (2016).

148 J. M. Rimsza, L. Deng, and J. Du, "Molecular Dynamics Simulations of Nanoporous Organosilicate Glasses using Reactive Force Field (ReaxFF)," *J. Non. Cryst. Solids*, **431**, 103–11 (2016).

149 J. C. Fogarty, H. M. Aktulga, A. Y. Grama, A. C. T. Van Duin, and S. A. Pandit, "A Reactive Molecular Dynamics Simulation of the Silica-Water Interface," *J. Chem. Phys.*, **132** [17] 4704–14 (2010).

150 H. J. C. Berendsen, D. van der Spoel, and R. van Drunen, "GROMACS: A Message-Passing Parallel Molecular Dynamics Implementation," *Comput. Phys. Commun.*, **91**, 43–56 (1995).

151 A. J. Lanphere, "A Structural Study of a Multicomponent E-CR Glass via Molecular Dynamics Simulation"; M.S. Thesis. Alfred University, Alfred, NY, 2015.

152 B. Hess, C. Kutzner, D. Van Der Spoel, and E. Lindahl, "GROMACS 4: Algorithms for Highly Efficient, Load-Balanced, and Scalable Molecular Simulation," *J. Chem. Theory Comput.*, **4** [3] 435–47 (2008).

153 C. Kutzner, D. van der Spoel, M. Fechner, E. Lindahl, U. M. Schmitt, B. L. De Groot, and H. Grubmuller, "Speeding Up Parallel GROMACS on High-Latency Networks," *J. Comput. Chem.*, **28**, 2075–84 (2007).

154 S. Plimpton, "Fast Parallel Algorithms for Short–Range Molecular Dynamics," *J. Comput. Phys.*, **117**, 1–19 (1995).

155 E. Neria, S. Fischer, and M. Karplus, "Simulation of Activation Free Energies in Molecular Systems," *J. Chem. Phys.*, **105** [5] 1902–21 (1996).

156 W. L. Jorgensen, J. Chandrasekhar, J. D. Madura, R. W. Impey, and M. L. Klein, "Comparison of Simple Potential Functions for Simulating Liquid Water," *J. Chem. Phys.*, **79** [2] 926 (1983).

157 W. Humphrey, A. Dalke, and K. Schulten, "Visual Molecular Dynamics," *J. Mol. Graph.*, **14** [1] 33–38 (1996).

158 G. Bussi, D. Donadio, and M. Parrinello, "Canonical Sampling Through Velocity Rescaling," *J. Chem. Phys.*, **126**, 14101-1-014101–7 (2007).

159 J. Du, "Molecular Dynamics Simulation of the Structure of Silicate Glasses Containing Hydroxyl Groups and Rare Earth Ions"; Ph.D. Thesis. Alfred University, Alfred, NY, 2004.

160 S. H. Garofalini, "A Molecular Dynamics Simulation of the Vitreous Silica Surface," *J. Chem. Phys.*, **78** [4] 2069–72 (1983).

161 B. P. Feuston and S. H. Garofalini, "Topological and Bonding Defects in Vitreous Silica Surfaces," *J. Chem. Phys.*, **91** [1] 564 (1989).

162 D. I. Grimley, A. C. Wright, and R. N. Sinclair, "Neutron Scattering from Vitreous Silica IV. Time-of-Flight Diffraction," *J. Non. Cryst. Solids*, **119**, 49–64 (1990).

163 R. L. Mozzi and B. E. Warren, "The Structure of Vitreous Silica," *J. Appl. Crystallogr.*, **2**, 164–72 (1969).

164 D. A. McKeown, G. A. Waychunas, and G. E. Brown, "EXAFS Study of the Coordination Environment of Aluminum in a Series of Silica-Rich Glasses and Selected Minerals within the Na_2O-Al_2O_3-SiO_2 System," *J. Non. Cryst. Solids*, **74**, 349–71 (1985).

165 P. Rino, U. Federal, and I. Ebbsj, "Interaction Potential for SiO_2 : A Molecular-Dynamics Study of Structural Correlations," *Phys. Rev. B*, **41** [17] 12197–208 (2015).

166 D. A. Mckeown, G. A. Waychunas, and G. E. Brown, "EXAFS and XANES Study of Coordination Environment of Sodium in a Series of Silica-Rich Glasses and Selected Minerals within the Na_2O-Al_2O_3-SiO_2 System," *J. Non. Cryst. Solids*, **74**,

325–48 (1985).

167 G. N. Greaves, S. J. Gurman, C. R. A. Catlow, A. V Chadwick, S. Houde-Walter, C. M. B. Henderson, and B. R. Dobson, "A Structural Basis for Ionic Diffusion in Oxide Glasses," *Philos. Mag. A*, **64** [5] 1059–72 (1991).

168 T. Uchino, T. Sakka, Y. Ogata, and M. Iwasaki, "Local Structure of Sodium Aluminosilicate Glass: An ab Initio Molecular Orbital Study," *J. Phys. Chem.*, **97**, 9642–49 (1993).

169 K. Muralidharan, J. H. Simmons, P. A. Deymier, and K. Runge, "Molecular Dynamics Studies of Brittle Fracture in Vitreous Silica: Review and Recent Progress," *J. Non. Cryst. Solids*, **351** [18] 1532–42 (2005).

170 A. Pedone, G. Malavasi, M. Cristina Menziani, U. Segre, and A. N. Cormack, "Molecular Dynamics Studies of Stress-Strain Behavior of Silica Glass under a Tensile Load," *Chem. Mater.*, **20** [13] 4356–66 (2008).

171 L. R. V. Adkins, "Molecular Dynamics Simulations of the Structure and Failure of Silicate Glasses"; Ph.D. Thesis. Alfred University, Alfred, NY, 2011.

172 R. L. Mozzi and B. E. Warren, "The Structure of Vitreous Silica," *J. Appl. Crystallogr.*, **2** [4] 164–72 (1969).

173 T. F. Soules and A. K. Varshneya, "Molecular Dynamic Calculations of A Sodium Borosilicate Glass Structure," *J. Am. Ceram. Soc.*, **64** [3] 145–50 (1981).

174 M. Ren, L. Deng, and J. Du, "Bulk, Surface Structures and Properties of Sodium Borosilicate and Boroaluminosilicate Nuclear Waste Glasses from Molecular Dynamics Simulations," *J. Non. Cryst. Solids*, **476**, 87–94 (2017).

175 R. L. Mozzi and B. E. Warren, "The Structure of Vitreous Boron Oxide," *J. Appl. Crystallogr.*, **3** [4] 251–57 (1970).

176 V. Petkov, S. J. L. Billinge, S. D. Shastri, and B. Himmel, "Polyhedral Units and Network Connectivity in Calcium Aluminosilicate Glasses from High-Energy X-Ray Diffraction," *Phys. Rev. Lett.*, **85** [16] 3436–39 (2000).

177 G. N. Greaves, A. Fontaine, P. Lagarde, D. Raoux, and S. J. Gurman, "Local Structure of Silicate Glasses," *Nature*, **293**, 611 (1981).

178 M. Fábián, T. Proffen, U. Ruett, E. Veress, and E. Sváb, "Uranium Surroundings in Bborosilicate Glass from Neutron and X-ray Diffraction and RMC Modelling," *J. Phys. Condens. Matter*, **22** [40] 1–8 (2010).

179 E. Matsubara, S. Tanaka, A. Makino, and T. Chiang, "Crystallization Behavior of Fe in $Fe_{84}Nb_7B_9$ and $Fe_{85}Nb_6B_9$ Amorphous Alloys," *Mater. Trans.*, **45** [4] 1199–1203 (2004).

180 R. D. Shannon, “Revised Effective Ionic Radii and Systematic Studies of Interatomic Distances in Halides and Chalcogenides,” *Acta Crystallogr. Sect. A*, **32** [5] 751–67 (1976).

181 M. Benoit, S. Ispas, and M. E. Tuckerman, “Structural Properties of Molten Silicates from *Ab Initio* Molecular-Dynamics Simulations: Comparison Between $CaO{-}Al_2O_3{-}SiO_2$ and SiO_2,” *Phys. Rev. B*, **64** [22] 224205 (2001).

182 R.-S. Zhou and R. L. Synder, “Structures and Transformation Mechanisms of the η, γ and θ Transition Aluminas,” *Acta Crystallogr. Sect. B*, **47** [5] 617–30 (1991).

183 C. W. Burnham and M. J. Buerger, “Refinement of the Crystal Structure of Andalusite,” *Z. Kristallogr.- Crystallogr. Mater.*, **115** [1–6] 269–90 (1961).

184 N. Ishizawa, T. Miyata, I. Minato, F. Marumo, and S. Iwai, “A Structural Investigation of α-Al2O3 at 2170 K,” *Acta Crystallogr. Sect. B*, **36** [2] 228–30 (1980).

185 L. Deng and J. Du, “Development of Effective Empirical Potentials for Molecular Dynamics Simulations of the Structures and Properties of Boroaluminosilicate Glasses,” *J. Non. Cryst. Solids*, **453**, 177–94 (2016).

186 J. F. Stebbins, “NMR Evidence for Five-Coordinated Silicon in A Silicate Glass at Atmospheric Pressure,” *Nature*, **351**, 638–39 (1991).

187 A. M. George and J. F. Stebbins, “Dynamics of Na in Sodium Aluminosilicate Glasses and Liquids,” *Phys. Chem. Miner.*, **23** [8] 526–34 (1996).

188 M. M. Smedskjaer, R. E. Youngman, and J. C. Mauro, “Impact of ZnO on the Structure and Properties of Sodium Aluminosilicate Glasses: Comparison with Alkaline Earth Oxides,” *J. Non. Cryst. Solids*, **381**, 58–64 (2013).

CHAPTER 10. APPENDIX

1. X-ray Diffraction plot

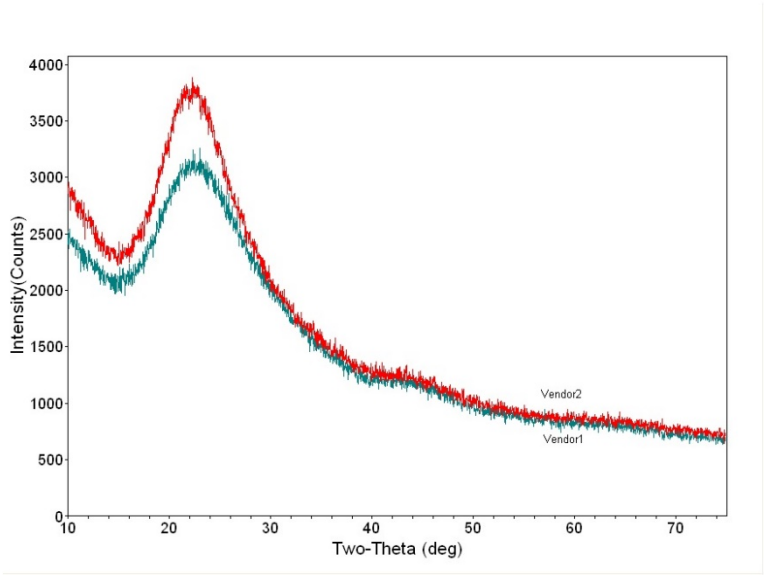

Figure 10-1. XRD plots for melted commercial PMT glasses